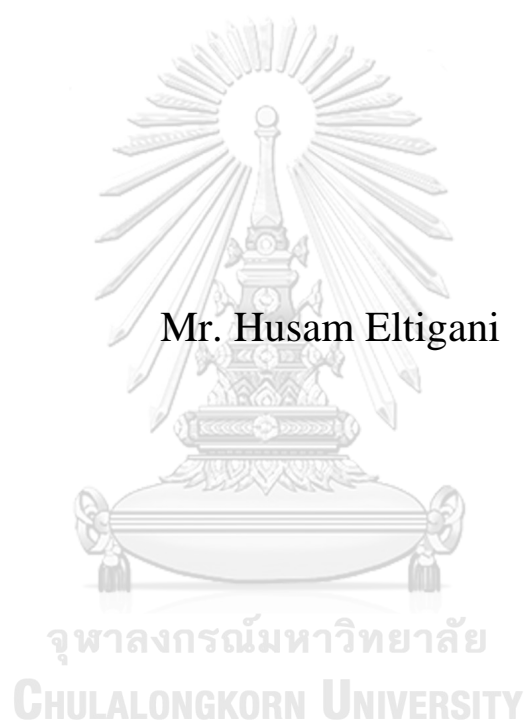


**TUNING THE WETTABILITY OF METAL SURFACE WITH
ELECTRODEPOSITED POROUS COPPER AND
GRAPHENE COATINGS**



Mr. Husam Eltigani

**A Dissertation Submitted in Partial Fulfillment of the Requirements
for the Degree of Doctor of Philosophy in Nanoscience and Technology
Inter-Department of Nanoscience and Technology
GRADUATE SCHOOL
Chulalongkorn University
Academic Year 2021
Copyright of Chulalongkorn University**

การปรับภาวะการเปียกของพื้นผิวโลหะด้วยทองแดงพรมที่ชุบด้วยไฟฟ้าและชั้นเคลือบผิวกราฟีน



วิทยานิพนธ์นี้เป็นส่วนหนึ่งของการศึกษาตามหลักสูตรปริญญาวิทยาศาสตรดุษฎีบัณฑิต
สาขาวิชาวิทยาศาสตร์นาโนและเทคโนโลยี สหสาขาวิชาวิทยาศาสตร์นาโนและเทคโนโลยี

บัณฑิตวิทยาลัย จุฬาลงกรณ์มหาวิทยาลัย

ปีการศึกษา 2564

ลิขสิทธิ์ของจุฬาลงกรณ์มหาวิทยาลัย

Thesis Title TUNING THE WETTABILITY OF METAL
SURFACE WITH ELECTRODEPOSITED POROUS
COPPER AND GRAPHENE COATINGS
By Mr. Husam Eltigani
Field of Study Nanoscience and Technology
Thesis Advisor Professor Dr. YUTTANANT
BOONYONGMANEERAT
Thesis Co Advisor Dr. NADNUDDA RODTHONGKUM

Accepted by the GRADUATE SCHOOL, Chulalongkorn University in
Partial Fulfillment of the Requirement for the Doctor of Philosophy

..... Dean of the GRADUATE
SCHOOL
(Associate Professor Dr. YOOTHANA
CHUPPUNNARAT)

DISSERTATION COMMITTEE

..... Chairman
(Professor Dr. VUDHICHAJ PARASUK)
..... Thesis Advisor
(Professor Dr. YUTTANANT
BOONYONGMANEERAT)
..... Thesis Co-Advisor
(Dr. NADNUDDA RODTHONGKUM)
..... Examiner
(Assistant Professor Dr. SUKKANESTE
TUNGASMITA)
..... Examiner
(Assistant Professor Dr. RATTHAPOL RANGKUPAN)
..... External Examiner
(Dr Martin Metzner)

สุชาม อธิทานิ : การปรับภาวะการเปียกของพื้นผิวโลหะด้วยทองแดงพรุนที่ชุบด้วยไฟฟ้าและชั้นเคลือบผิวกราฟีน. (TUNING THE WETTABILITY OF METAL SURFACE WITH ELECTRODEPOSITED POROUS COPPER AND GRAPHENE COATINGS) อ.ที่ปรึกษาหลัก : ยุทธนันท์ บุญยงมณีรัตน์, อ.ที่ปรึกษาร่วม : นาฏนัดดา รอดทองคำ

ทองแดงที่มีความพรุนที่ผลิตขึ้นด้วยกระบวนการชุบทางเคมีไฟฟ้าเป็นวัสดุเคลือบผิวแบบใหม่ที่มีการพัฒนาขึ้นและมีโอกาสนำไปใช้ประโยชน์ในหลากหลายงาน อย่างไรก็ตาม องค์กรผู้เกี่ยวข้องกับความสัมพันธ์ของคุณสมบัติการเปียกผิวของทองแดงพรุน และค่าพารามิเตอร์ในการชุบ รวมทั้ง สภาวะการเก็บรักษา ยังคงมีจำกัด นอกจากนี้ มีความน่าสนใจว่า วัสดุนาโน ดังเช่นกราฟีน หากมีการนำมาใช้เคลือบผิวทองแดงอีกชั้น จะมีผลต่อภาวะการเปียกของผิวชุบทองแดงอย่างไร งานวิทยานิพนธ์นี้ จึงเป็นการศึกษาพัฒนากรอบความสัมพันธ์ของกระบวนการชุบทองแดงและการเคลือบกราฟีน สภาวะการเก็บรักษาชิ้นงาน และคุณสมบัติการเปียกผิวของทองแดง งานวิจัยแบ่งออกเป็น 2 ส่วน ได้แก่ (i) ผลของการชุบและสภาวะการเก็บรักษาที่มีต่อภาวะการเปียกของผิวทองแดงพรุน และ (ii) การปรับภาวะการเปียกของผิวทองแดงด้วยกระบวนการหดยุทธศาสตร์กราฟีน จากการศึกษาวิเคราะห์โครงสร้างทางจุลภาคของชิ้นงานและมุมสัมผัสของน้ำบนพื้นผิวด้วยเทคนิคและอุปกรณ์วิเคราะห์ต่างๆ ทำให้ค้นพบว่า ความเข้มข้นของน้ำยาชุบทองแดงและกระแสไฟฟ้าเป็นปัจจัยสำคัญที่ควบคุมลักษณะความพรุนของผิวชุบทองแดง อันส่งผลต่อการมีมุมสัมผัสที่ค่าต่างๆ ในช่วงภาวะการเปียกแบบชอบน้ำ นอกจากนี้ ในขณะที่สภาวะการเก็บรักษาแบบในอากาศส่งเสริมภาวะการเปียกแบบชอบน้ำ การจัดเก็บแบบมีความชื้นหรือในสภาวะเกลือ ส่งเสริมให้พื้นผิวทองแดงมีภาวะการเปียกแบบไม่ชอบน้ำ ในส่วนของการเคลือบผิวทองแดงด้วยกราฟีน โดยวิธีการหดยุทธศาสตร์ พบว่าสามารถปรับมุมสัมผัสของน้ำบนพื้นผิวทองแดงได้ตั้งแต่ภาวะการเปียกแบบชอบน้ำยิ่งยวด ถึงแบบไม่ชอบน้ำยิ่งยวด ทั้งนี้ขึ้นอยู่กับความพรุนของทองแดง ความเข้มข้นของสารละลายกราฟีน และระดับการกระจายตัวของผงกราฟีน ดังนั้น งานวิจัยได้แสดงให้เห็นว่ากราฟีนเป็นวัสดุที่น่าสนใจในการเคลือบผิวทองแดงที่สามารถช่วยปรับแต่งภาวะการเปียกของพื้นผิวได้เป็นอย่างดี

จุฬาลงกรณ์มหาวิทยาลัย
CHULALONGKORN UNIVERSITY

สาขาวิชา วิทยาศาสตร์นาโนและเทคโนโลยี
ปีการศึกษา 2564

ลายมือชื่อนิสิต
ลายมือชื่อ อ.ที่ปรึกษาหลัก
ลายมือชื่อ อ.ที่ปรึกษาร่วม

6087813020 : MAJOR NANOSCIENCE AND TECHNOLOGY

KEYWORD Porous copper; Electrodeposition; Graphene; Wettability; Storage
D: condition

Husam Eltigani : TUNING THE WETTABILITY OF METAL SURFACE
WITH ELECTRODEPOSITED POROUS COPPER AND GRAPHENE
COATINGS. Advisor: Prof. Dr. YUTTANANT
BOONYONGMANEERAT Co-advisor: Dr. NADNUDDA
RODTHONGKUM

Electrodeposition of porous copper is an interesting type of coating that is emerging for various applications. However, the understanding of the relationships between copper surface wettability control and electrodeposition parameters and post-electrodeposition storage conditions is quite limited. Furthermore, it is worthwhile to explore how nanomaterials such as graphene would interact with porous copper to provide surface wettability modifications. This work therefore aims to develop a framework for the relationship of copper and graphene deposition processes, storage conditions, and the wetting behavior of copper surfaces. The research work performed in this study is divided into 2 parts: (i) effects of plating and storage conditions on the wettability of electrodeposited porous copper surfaces, (ii) tailoring the wettability of copper surfaces by dropping of graphene solutions. From a wide range of characterization methods and analysis to investigate the microstructure of porous copper and graphene, and corresponding wetting properties of their surfaces, the key findings of the study are that the concentration of copper electrolyte and current density largely influence the microstructure of the porous copper which subsequently lead to the variations of contact angles in the hydrophilic regime. Furthermore, whereas the air storing condition promote hydrophobicity, the water and saline storage conditions are found to induce hydrophilicity. Finally, deposition of graphene using a solution dropping technique allows tuning of the surface wettability in a wide range, spanning superhydrophilic to superhydrophobic, depending on copper surface porosity and graphene solutions' concentration and dispersing level. Graphene is thus demonstrated as a promising top-coat layer to tune the wettability of copper surfaces

Field of Study: Nanoscience and
Technology
Academic 2021
Year:

Student's Signature
.....
Advisor's Signature
.....
Co-advisor's Signature
.....

ACKNOWLEDGEMENTS

I am grateful to the Chulalongkorn University 100th Anniversary Scholarship for financial support. A special thanks go to Graduate School, Nanoscience and Nanotechnology Program, Metallurgy and Materials Science Research Institute MMRI, and the academic staff who focused the organizational effort and provided official service at a time when it was most needed

I would like to thank my advisor, Prof. Dr. Yuttanant Boonyongmaneerat, and my co-advisor, Dr. Nadnudda Rodthongkum, for great help and support with all my Ph.D. Student life. I am appreciated their teaching, training, and inspiration. I would also like to thank them for their support in researching and supervising theses until the completion of this dissertation.

More thankful to the senior students for the laboratory work assistance. I am also incredibly grateful for my friends Aui, Dr. Jai, Dr.Koong, Dr.Oak, Nittiya Firm, Belle and Fern.

I am thankful to all thesis committees, including Prof.Dr. Vudhichai Parasuk, Prof. Dr. Yuttanant Boonyongmaneerat, Asst. Prof. Dr. Ratthapol Rangkupan, Asst.Professor. Dr. Sukkaneste Tungasmita, Dr. Nadnudda Rodthongkum, and Dr. Martin Metzner for suggestions and guidance in thesis.

Last but not least, I would like to express my heartfelt thanks to my mother, Mariam, and my father's soul, Hussein, and I hope his soul lives in peace. More warm thanks to my brothers and sisters, Husham, Ikram, Siham, and Ibrahim, who always encouraged me during my Ph.D study.

To all of you, I dedicate everything I have done.

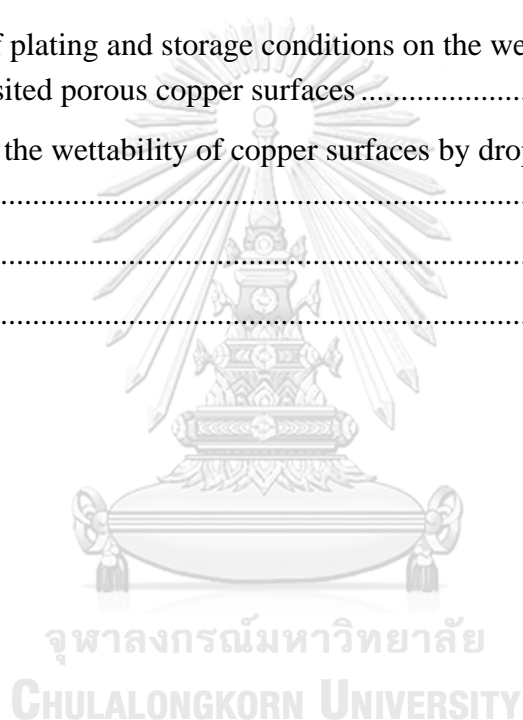
Husam Eltigani

TABLE OF CONTENTS

	Page
ABSTRACT (THAI)	iii
ABSTRACT (ENGLISH).....	iv
ACKNOWLEDGEMENTS	v
TABLE OF CONTENTS.....	vi
List of Tables	ix
List of Figures	x
CHAPTER I INTRODUCTION.....	1
1.1 Motivation	1
1.2 The objective of the research.....	5
1.3 Scope of research.....	5
CHAPTER II LITERATURE REVIEW	7
2.1 Wettability	7
2.2 Copper electroplating.....	8
2.2.1 Fundamentals of electroplating	8
2.2.2 Copper electroplating baths.....	10
2.2.3 The effect of hydrogen bubbles on electroplating of the porous copper surface	13
2.3 Graphene and its properties	17
2.4 Graphene coating techniques	21
2.5 Theory of wetting of the textured surface.....	23
2.5.1 Contact angle and surface tension	23
2.5.2 Types of pore and capillary pressure.....	30
2.5.3 Wenzel's theory.....	33
2.5.4 Cassie-Baxter theory	36
2.5.5 Transition between Wenzel and Cassie-Baxter states	37
2.5.6 Wetting and Adsorption	38

2.5.7 Correlation between copper and graphene	39
2.5.8 Wetting behavior and transparency of graphene	41
2.6 Water Desalination across Nanoporous Graphene and through graphene multilayers as membranes	45
CHAPTER III EXPERIMENTAL PROCEDURE.....	50
Part 1 Effects of plating and storage conditions on the wettability of electrodeposited porous copper surfaces	50
3.1.1 Sample preparation and fabrication.....	50
3.1.2 Storage condition test	52
3.1.3 Sample characterization	52
Part 2 Tailoring the wettability of copper surfaces by dropping of graphene solutions.....	54
3.2.2 Sample characterization	57
CHAPTER IV EXPERIMENTAL RESULTS AND DISCUSSION.....	58
Part 1 Effects of plating and storage conditions on the wettability of electrodeposited porous copper surfaces	58
4.1.1 Characteristics of the copper electrodeposits	58
4.1.2 Wetting behavior	61
Fig. 28 presents the wetting angles of the samples in groups A, B, and C in the as-deposited state and after exposure to air. After deposition, all groups of samples exhibit Wenzel state, hydrophilic behavior, with advancing contact angles below approximately 20°. This was followed by rapid penetration of the droplet in	61
4.1.3 The effects of storage conditions.....	65
4.1.4 Porosity control of copper surfaces	71
Part 2 Tailoring the wettability of copper surfaces by dropping of graphene solutions.....	74
4.2.1 A comparison of the Raman spectrum of graphene	74
4.2.1.1 Raman spectrum of graphene powder	74
4.2.1.2 Raman spectra of graphene layers on metals surfaces	76
A) Flat surface	76
B) Porous surfaces	80

4.2.2 TEM images for graphene solutions Sol1 and Sol2	81
4.2.3 Overall wettability results	84
4.2.4 Physical effect on wetting behavior	88
4.2.4.1 Flat copper surfaces	88
4.2.4.2 Porous copper surfaces	89
4.2.5 Chemical effect on wetting behavior.....	90
4.2.6 Further observation of the physical effect.....	94
CHAPTER VI CONCLUSION	96
Part 1 Effects of plating and storage conditions on the wettability of electrodeposited porous copper surfaces	96
Part 2 Tailoring the wettability of copper surfaces by dropping of graphene solutions.....	97
REFERENCES	98
VITA.....	113



List of Tables

	Page
Table 1 Concentration limit and operating condition of alkaline non-cyanide	12
Table 2 Formulation of acid copper solution [87].	13
Table 3 The effect of additives on porous copper from hydrogen bubble.....	16
Table 4 Different techniques and applications with water contact angles.....	17
Table 5 Surface tension of some liquid [140].	28
Table 6 Structure (interface distance D_{C-M}) and properties (interface binding energy E_b and mechanical strength σ_s) of Graphene-copper and Graphene-Nickel [182].....	41
Table 7 Electrodeposition parameters of the porous copper samples in 6 groups under investigation.....	51
Table 8 illustrates four names of different graphene solutions.....	56
Table 9 illustrates the names of each sample in detail.....	56
Table 10 Chemical composition of the C-2 samples after being stored in the different storage conditions for 4 weeks, as measured by EDS	64
Table 11 Chemical composition of the samples of interest C*-Sol1, C-Sol1 and C-Sol1' for 4 weeks, as measured by EDS	92

List of Figures

	Page
Figure 1 Schematic of the Stern layer, inner Helmholtz IH layer, outer Helmholtz OH layer, and diffuse layer. ζ -potential is the characterization of change of slipping plane.[83]	10
Figure 2 Schematic of the hydrogen bubbles 1. Anode 2. Power supply 3. Hydrogen bubbles .4 The deposited copper metal 5. Copper metal as a cathode.....	14
Figure 3 SEM images of copper electrodeposited for 20 s in electrolyte of 0.4 M $\text{CuSO}_4 + 1.5 \text{ H}_2\text{SO}_4 + 1 \text{ Mm}$ (a,b), 10mM (c,d), and 50 mM HCL (e,f) at an applied cell current density of 3 A/cm^2 .[90]	15
Figure 4 shows 2-dimension graphene, 1-dimensin carbon nanotube and 0-dimension Fullerene [107].....	19
Figure 5 Light transmittance between air, graphene, and a graphene bilayer [103]...20	20
Figure 6 Electrophoretic Deposition of graphene.....	23
Figure 7 A projection of a sessile drop, incremental change of radius, solid (S) and liquid (L) [131].	25
Figure 8 A schematic of the three interfacial tensions γ_{sg} , γ_{lg} , and γ_{sl}	25
Figure 9 The depiction of the rise of liquid inside a small-diameter vertical tube [136].....	27
Figure 10 Water droplets impinging on the superhydrophobic surface with different velocity and time of contact on the surface [144].....	29
Figure 11 Schematic images of pore types	31
Figure 12 Types of pore (a) closed, (b,c,e,f) open, (b,f) blind or dead-end/saccate, (f) through, and shape of pores are (b) ink-bottle shaped, (c) cylindrical open, (d) funnel shaped, (f) cylindrical blind, and (g) roughness [157].....	32
Figure 13 The meniscus in a capillary tube [158].....	32
Figure 14 A schematic diagram of Wenzel state	34
Figure 15 Roughness factor (r) with varying Young's intrinsic contact angle [165] .35	35
Figure 16 A schematic diagram of Young contact angle θ_Y and apparent contact angle θ_A	35

Figure 17 Increasing surface roughness with different measurements of contact angles described by Wenzel equation	36
Figure 18 A Schematic diagram of Cassie-Baxter state	37
Figure 19 Vapor adsorption isotherms for (a) complete wetting and (b) partial wetting. The dashed line represents the saturation axis (i.e., the saturated vapor pressure).[176]	39
Figure 20. The surface energy according to Neumann's equation	44
Figure 21 The permeability of water molecules through the defected area of graphene sheet and rejection of salt molecule by a graphene sheet	46
Figure 22 a) The diffusion of water molecules through the channels of the graphene oxide layers and the rejection of salt. b) Graphene oxide layers on a porous supported metal.....	47
Figure 23 A schematic of Oxygen Plasma synthesis method for creating pores on a graphene sheet.....	48
Figure 24 a) a hydroxylated pore (hydrophilic), b) a hydrogenated pore (hydrophobic).....	49
Figure 25 The process of graphene deposition on copper surfaces	55
Figure 26 Graphene solutions (Sol1, Sol', Sol2, Sol2' a) after 30 minutes sonication b) after three days.....	57
Figure 27 SEM micrographs showing the surface morphology of the porous	60
Figure 28 Advancing (θ_A), receding (θ_R), hysteresis, and sliding contact angles (θ_s) of the samples from 6 groups after 4 weeks of air exposure, in comparison with the contact angles of the samples measured following electrodeposition	62
Figure 29 Measured contact angle of the porous copper samples with respect to their surface roughness (R_a) after 4 weeks of air-exposure.....	65
Figure 30 Weekly measurements of contact angles of C-1 (a) and C-2 (b) samples exposed to different storage conditions: air, DI water, saline solution.....	68
Figure 31 SEM micrographs of the C-2 samples under 4-week storage tests: a) as-deposited and after exposure to b) air, c) DI water, and d) saline solution	69
Figure 32 Measured surface roughness of C-2 samples in the as-deposited state and after being exposed to different environmental conditions under investigation for 4 weeks.....	70
Figure 33 Contact angle measurements and porosity of all samples	73

Figure 34 Roughness and porosity measurements of all samples.....	73
Figure 35 A comparison between a) graphene powder, b) graphene nanoplatelets powder, and c) from a reference [214] d) showed similar Raman spectra from Raman for life (ramanlife.com).....	75
Figure 36 spectra of graphene of samples C-Sol1 and C-Sol1	76
Figure 37 shows a) the ideal Raman spectra between graphene and graphite. b) different shape of spectra around 2700 cm^{-1} [218]	77
Figure 38 Raman spectra recorded on the single-layer graphene sample of (b), both for the suspended (red solid line) and supported regions (blue dashed line). (c) Raman spectra in the lower-frequency region ($1,270\text{--}1,420\text{ cm}^{-1}$) for the two regions of the sample. (d) Detailed comparison of normalized spectra for the G mode [219].....	78
Figure 39 The Raman spectra of graphene as monolayer, bilayer,.....	79
Figure 40 Different Raman spectra of graphene on various metals [221].....	79
Figure 41 Raman spectra of two samples C*-Sol1 and C*-Sol1'	80
Figure 42 Raman spectra of graphitic layers grown on the porous structure. a) The outer surface and b) the cross-section after cutting [223].....	81
Figure 43 TEM images of graphene dispersed solutions a) Sol1, b) Sol2.....	82
Figure 44 TEM images of the graphene dispersed with different surfactants: (a) 300 ppm CTAB; 300 ppm CO890; (C) 200 ppm SDS and (d) 300 ppm H14N [225]	83
Figure 45 a) the initial graphite particle b) exfoliated multilayer graphene [226]....	83
Figure 46 Advancing AC_{θ} and receding RC_{θ} contact angles measurement for (C), (C-Sol1), (C-Sol1'), (C-Sol2), (C-Sol2'), (C*), (C*-Sol1), (C*-Sol1'), (C*-Sol2), and (C*-Sol2')	85
Figure 47 Photos of water droplets on samples (C), (C-Sol1), (C-Sol1'), (C-Sol2) and (C-Sol2')	86
Figure 48 Photos of water droplet on samples (C*), (C*-Sol1), (C*-Sol1'), (C*-Sol2) and (C*-Sol2')	87
Figure 49 More details of the Raman spectra of sample C*-Sol1	93
Figure 50 More details of the Raman spectra of sample C*-Sol2'	93
Figure 51 shown the porous copper without graphene C* (superhydrophobic) on left and the sample of interest C*-Sol1 (superhydrophilic) after 30 days of air exposure.	95
Figure 52 SEM micrographs showing the surface morphology of the 3D porous copper samples D* and D*-Sol1.....	95

CHAPTER I INTRODUCTION

1.1 Motivation

The wettability of a surface is one of the critical processing parameters to evaluate the performance of many modern pieces of equipment for further enhancement of their efficiency [1, 2]. It may also be useful for assessing the risk posed by chemical contamination on a surface [3]. In the industrial field, particularly in power or water desalination plants, it is essential to enhance thermal heat transfer with low-cost production taking into account technical considerations [4]. For instance, in thermal heat exchangers, which are made mostly from copper due to its high thermal conductivity, solving many straightforward problems such as erosion and controlling of the condensation rate are related to the wettability gradient of copper surfaces [5]. Another remarkable role of controlling the wettability of a solid surface, especially in an aqueous environment, is the help in mitigating electrochemical corrosion or galvanic corrosion of metals which can be triggered and accelerated further by the presence of adhering water to a conductive metal [6]. Furthermore, Controlling the wettability of a surface can be employed in many applications such as battery electrodes, sensors, and in electronic and electrical industries [7, 8]. For decades, a substantially broadened investigations on the physical and the chemical properties of a surface have been reported out and revealed that both surface morphology and the energy of the surface play a significant role in changing or controlling the affinity of liquid such as a water droplet with a surface. However, controlling the wetting behavior of water on a surface without alternating the intrinsic properties of a

substrate is still a challenge and would give rise to the additional investigation of surface structure.

One of the most common options of choice and important material for many industrial and domestic applications are copper metal, besides copper alloys like copper-lead and copper-Nickel [9-11]. Therefore, it is subjected to intensive investigation due to its excellent high thermal conductivity and electromigration resistance compared with another transition group of materials such as aluminum [12-15]. However, the susceptibility of pure copper to be oxidized is higher than silver but least comparing with zinc and magnesium [16-18]. Two types of copper oxide can be formed in an oxidation atmosphere. Reddish-colored cuprous oxide Cu_2O and black-colored cupric oxide CuO are common types of oxidation of copper [19]. This kind of residual oxides remains on a copper surface as an oxide layer if no surface treatment carried out. Thus, the reliability of using copper metal requires methods to improve its surface oxidation resistance [20-22]. The oxide layer can affect the electrical and thermal conductivity of the copper surface. Using chemical treatment is the conventional method of reduction of copper oxide to copper, especially for copper powder production [23, 24]. Electrochemically, recovering solid copper metal from a solution can be achieved by the electrowinning process [25, 26]. Moreover, in the casting process, additional treatments are needed to get rid of any impurities on the surface [27].

Improving the properties of a copper surface for high-quality products can be conducted by treating its substrate with an etching technique or with a thin layer of

coating [28]. However, in terms of wettability properties and geometry of a copper surface, fabrication of a coated porous copper surface is a candidate for capable controlling and has numerous applications [29-32]. There are several possible techniques to produce hierarchical surface (nano/micro surface) or alternative methods to manipulate porous surfaces, including methods such as electrochemical dealloying, etching, annealing or electrochemical anodization [33, 34]. However, some of these techniques such as etching depend on the removal of unprotected part of a metal surface which consumes the metal volume of the substrate during the process and may hinder the chance for any desired future direction for modification requirement or corrective maintenance on the surfaces.

One of the easiest ways to sculpt micro/nanoporous surfaces is to combine both the electrodeposition process and the hydrogen bubble dynamic template [35-38]. In the case of copper metal, the fabrication of porous surfaces with different pore sizes and shapes is controlled by changing some electroplating parameters such as current density [39-41]. Controlling the nanopore size and micro wall thickness of the coated copper film can be tailored either chemically by changing the concentration of the acid solution which contains both copper sulfate and sulfuric acid or by adjusting important electroplating parameters such as overpotential and temperature. The electrochemical reduction of hydrogen leads hydrogen bubbles to appear on the cathode surface with the reduction of copper ions [42]. It should be noted here that Cu^{2+} more easily reduced than H^+ , an oxygen gas is produced at the anode. In the deposition process and between the interstitial spaces of the hydrogen bubble, copper

film starts to deposit and grows on the copper substrate with fresh porous deposit copper [43].

A pivotal consideration of adopting graphene is to hinder any accelerate of copper oxide on copper surfaces and hold the intrinsic properties of a copper surface [44]. Apart from its excellent features such as thermal stability and chemically inert, graphene is expected to perform as a crucial element in the fabrication of dual scale nano/micro [45]. This gapless two-dimensional metal can pave the way for having high-quality porous copper surfaces and improving thermal conductivity. Therefore, by helping to suppress copper oxidation, the desired degree of wetting can be tuned.

An example of interest is in controlling the feed water in steam thermal power plant, the need to control the condensation rate [46-49]. Condensation occurs when there is a state of water vapor happens on a solid surface [50]. During condensation growth, it is essential to have a kind of stable partial wetting [51]. The condensation from vapor starts to grow from the depth grooves on the surface which need for high performance of condensation, a state between the stable sticky Wenzel mode and the unsticky Cassie-Baxter mode [52, 53]. This can be observed because of a mixture of both wetted grooves and trapped air-pockets underneath droplets. As a consequence, pinning droplets do not wholly penetrate the surface, minimizing the rapid transition from partial to full wetting [54-56]. Two kinds of condensation are called dropwise condensation, which is desired for enucleation of droplet resulting in high heat transfer, and filmwise condensation, which has significant thermal resistance to heat transfer [57, 58].

This research constitutes new area of research on wettability to understand the effects of electroplating parameters (current density and time) and the presence of graphene as multilayers on tuning the wettability.

The correlation between copper deposition and the observed wetting transparency of graphene may provide a framework comprising a wide range of tunable degrees of wettability on copper surface. For more assessment of the wettability, further study looks necessary to elucidate the influence of graphene on wetting properties

1.2 The objective of the research

- To compare the effect of electroplating conditions on developments of nano/microstructure of copper surfaces
- To obtain the understanding of the wetting stability of porous copper surface.
- To understand the correlation between copper deposition and observed wetting characteristics of graphene.
- To examine the feasibility of controlling the wettability of electroplated copper surfaces by employing of graphene.

1.3 Scope of research

This research work is divided into two main parts:

First part is to prepare porous copper surfaces on copper substrates using the hydrogen bubble template as a precursor coating. In addition, to test and compare the effect of environmental and storage conditions on the change in the morphology of deposited copper surfaces and the wetting behavior. The acid copper solution has

different concentration parameters of copper sulphate and sulfuric acid with fixing the temperature and without stirring of the copper acid solution upon electrodepositing. This part connected with measuring of contact angles to study the behavior of water on copper substrate and electroplated copper surface.

The second part is to perform graphene dropping using different concentrations, and dispersions of graphene solutions on copper substrates and electrodeposited copper surfaces.

All parts will be coupled with characterizing, analysis, monitoring and evaluation of the behavior of water on different structures of copper surfaces.

1.4 Benefits of research

This work is expected to offer an avenue to systematically and economically identify, modify, evaluate and improve copper surfaces as desired in terms of the wettability of a surface and to investigate the positive influence of graphene in tuning the wettability of copper surfaces, which its excellent properties gradually become demanded in more applications. It also allows exploring and comparing appropriate fabrication techniques of dual scale nano/microporous copper surface and therefore embodies its promotive effect on the wetting properties. The benefits of this research can be extended to the production antibacterial copper surfaces and the improvement of water desalination technology, where controlling wettability plays an important role.

CHAPTER II LITERATURE REVIEW

2.1 Wettability

Wettability is the tendency of a fluid to spread or remain on a surface. This ability of a fluid to adhere strongly or weakly to a surface is governed by its interaction with a solid [59]. The wettability of surfaces can be evaluated by measuring the contact angle (CA) of a liquid on a surface and its surface tension, which is described by Young's equation. Between the solid/liquid interface, the droplet can be flattened or rolled off according to the degree of contact angle value (from 0° to 180°) [60-63]. Therefore, the interaction of a surface with water molecules can be defined as a hydrophobic, hydrophilic, or superhydrophobic surface (non-wetting or water-repellent $> 150^\circ$), as observed in lotus leaves and super hydrophilic surface (ultimately spreading of liquid droplet across a surface) [64-66]. If the surface has high surface energy, the action of a fluid is to minimize the surface energy. On the other hand, the cohesive force of fluid molecules and their adhesion force to a solid is the criteria for understanding a fluid's behavior with a surface [59, 67]. By neglecting some effects, such as gravitational potential energy, surface vibration as well as physical and chemical properties of the surrounding environment, it can be concluded that the mobility of droplet moves along the surface depending on the surface's roughness and its chemical state [67, 68].

2.2 Copper electroplating

2.2.1 Fundamentals of electroplating

Electroplating is the key solution and the technology of choice for diverse functional materials, engineering, and decorative applications [69]. This is especially applicable for thermal equipment and complex modern electronic device [70]. This technique adds new properties, thickness or protection of substrate metals [71]. Electroplating is defined as a process of adding a thin layer to a substrate by transferring metal ions via an electrical field. Generally, it consists of a chemical solution (electrolyte), and two electrodes immersed the electrolyte, a positive electrode (anode) and a negative electrode (cathode) are connected with DC or AC electrical power supply to control operating current and voltage [72, 73]. The metal to be electroplated becomes the cathode of an electrolytic cell that receives the ions that dissolve in the electrolyte. The surface negative charge on the cathode attracts the positively charged ions (cations) like copper (Cu^{2+}) from the solution [73]. These positively charged ions accumulate on the surface and after a period of time there will be a kind of dynamic equilibrium between metal M and its ions:



The activity of metal ions $a(\text{M}^{Z+})$ is functioned by the potential E of the M^{Z+}/M electrode

$$E = E^0 + \frac{RT}{zF} \ln a(\text{M}^{Z+}) \dots\dots\dots(2)$$

Where E^0 is the relative standard electrode potential of metal, R is gas constant, T is the absolute temperature, z is the number of electrons involved in the reaction, F is Faraday's constant (96,500 C) [74]. Moreover, the relation between the amount of

electrochemical reaction at an electrode and the quantity of electrical charge Q passed is governed by Faraday's law. From this law the theoretical weight of the product w of electrolysis can be calculated:

$$W = ZQ = A_{wt}/zF \dots \dots \dots (3)$$

Where Z is the electrochemical equivalent ($Z (\text{Cu}^{2+}) = 3.293 \times 10^{-4} \text{ g C}^{-1}$), and A_{wt} is the atomic weight of metal deposited (for Cu =63.55) [69].

The electrolyte solutions can also contain additives or leveling agents to either improve the process itself or modify the electroplated surfaces [75]. On the other hand, it contains consumable or non-consumable anodes. Non-consumable anodes result in uniform plating and faster plating speeds than consumable anodes [76]. Electroplating parameters such as current density, pH, and temperature are essential to the quality of metal deposits [77]. Both metal ions and electrons alternatively carry the charge from the rectifier power supply. In laboratory work and even in industry, the provision of adequate electrical power supply system can be from a DC (direct current), pulsating direct current or AC (alternating current) [78-80]. At the metal-solution interface, electrons come out from the anode metals to the electrolyte solution, and on the other side, the accumulated ions on the second metal-solution interface in the vicinity of the cathode [59]. According to a combination of the models of Gouy Chapman, Stern, and Helmholtz, the slipping plane (the solid/solution interface region) can be divided into two regions, namely the inner region and the diffusion region [81, 82] (**Figure 1.**) Moreover, in order to achieve a uniform deposit layer thickness across a cathode surface, it is vital to enhance the ability of an electrolyte (throwing power), such as by adjusting applied voltage, and by filling up

the deposit into macro scratches or even micro-valleys of irregularly-shaped areas [59].

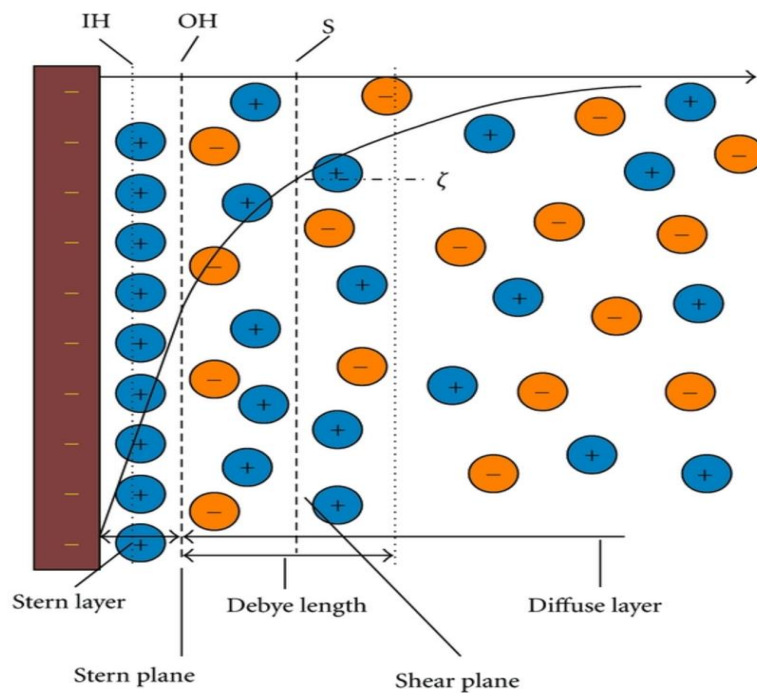


Figure 1 Schematic of the Stern layer, inner Helmholtz IH layer, outer Helmholtz OH layer, and diffuse layer. ζ -potential is the characterization of change of slipping plane.[83]

CHULALONGKORN UNIVERSITY

2.2.2 Copper electroplating baths

An electrodeposited copper layer can be obtained from a wide range of copper baths based on other plating adjustment parameters, such as current density or solution temperature [83]. The composition of electrodepositing copper baths includes acid baths, alkaline baths, alkaline agents, and copper cyanide baths [69]. However, one of the most commonly used baths is an aqueous acid solution, a mixture of sulfuric acid

(H_2SO_4) and cupric sulfate (CuSO_4) [84]. The concentration of the bath composition is limited to satisfy the requirements for specific applications. For example, limited alkaline non-cyanide copper plating baths composition and operating conditions are given in **Table 1**. Some formulation of acid copper solutions is illustrated in **Table 2**. Interestingly, it is reported that changing sulfate/sulfuric acid electrolyte concentration has an insignificant effect on the hardness of the copper plate.[83] Preventing the formation of cupric crystals on anodes can be minimized by increasing sulfuric acid. In some cases, low copper sulfate with high sulfuric acid improve throwing power especially for plating printed circuit boards [83]. Commonly sulfuric acid is used to lower pH solutions. However, for hydrogen evolution reaction, sulfuric acid gives high rich of hydrogen. Reversely, increasing the concentration of cupric sulfate leads to a decrease in the concentration of hydrogen ions [85].

In some plating baths, additives are employed for improving both brightening and physical properties. Furthermore, addition agents are used to altering copper powder characteristics. Another example, adding cetyl trimethyl ammonium bromide (CTAB) to copper sulfate can improve the mechanical and property of the deposit Cu-ZrO_2 [86]. The electroplating bath can be characterized by electrochemical techniques, potentiometric titration or UV-visible spectroscopy.

Table 1 Concentration limit and operating condition of alkaline non-cyanide cyanide copper plating baths.[83]copper plating baths.[83]

Constituent or Condition	Typical
Copper metal from copper sulphate concentration limit, g/l (oz/gal)	6-13.5 (0.8-1.8)
PH	9-10.5
Electrometric temperature °C °F	38-65 (100-150)
Cathode current density A/dm ² (A/ft ²)	0.5-3.0 (5-30)
Anode: cathode ratio	1.5:1

However, to establish optimum conditions and plating bath composition, it should be considered a parameter with the degree of agitation, the properties of the despitte, and current density for better electroplating products. Careful preparation and control of the composition of electroplating baths can prevent any deterioration, which may lead to replacing entire bath solutions.

Table 2 Formulation of acid copper solution [87].

Copper sulfate solution	Conventional solution	High-throw solution
CuSO ₄ .5H ₂ O, g/L	200-250	60-100
H ₂ SO ₄ , g/L	45-90	180-270
Chloride, mg/L	-	50-100
Copper Fluoborite Solutions	Low-concentration Solutions	High-concentration Solutions
Copper fluoborite Cu (BF ₄) ₂ , g/L	225	450
Fluoboric acid, HBF ₄ , g/L	15	30
Boric Acid, H ₃ BO ₃	15	30

2.2.3 The effect of hydrogen bubbles on electroplating of the porous copper surface

This economic efficient process is exploited to produce a micro/nanoporous surface and accompany it with electrodeposition. Together with the reduction of solvated metal ions during the electrodeposition process, hydrogen ions H⁺ are reduced to H₂ with freshly growing deposited metal. From this proceeding, micropores and nanopores around the bubbles can be created. The bubbles act as physical spacers that

create interstitial spaces, and as a consequence of this process, the obtained structure contains a kind of foam, dendrites, nanostructures pores, and walls [88, 89]. **Figure 2** and **Figure 3** give an example of the electroplating process of copper acid solution which consists of copper sulfate and sulfuric acid. The chemical equation of electrodeposition can be written in the following way:

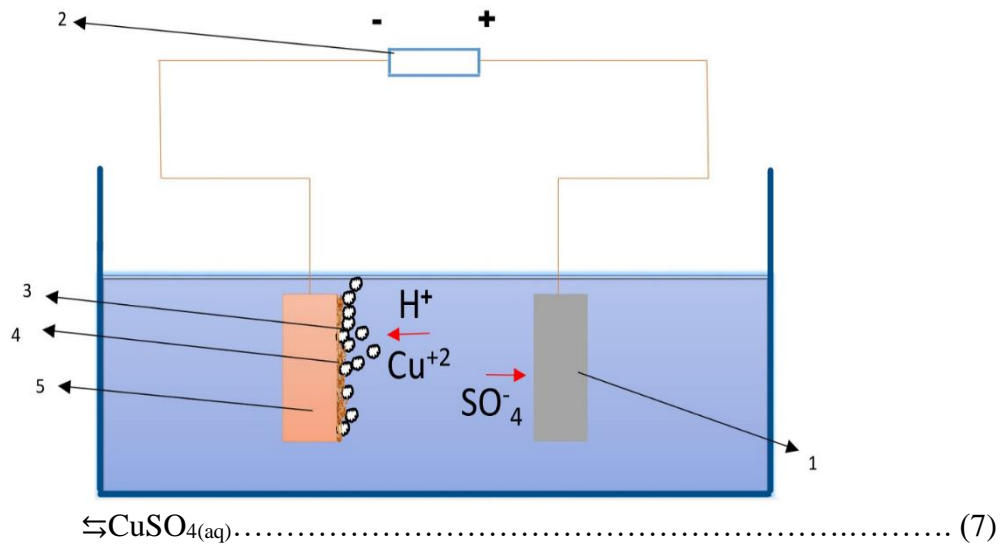
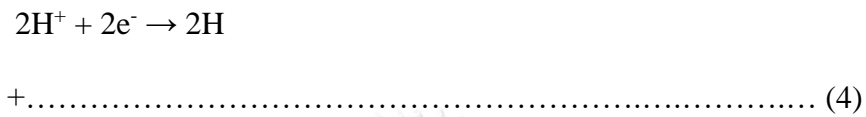


Figure 2 Schematic of the hydrogen bubbles 1. Anode 2. Power supply 3. Hydrogen bubbles .4 The deposited copper metal 5. Copper metal as a cathode.

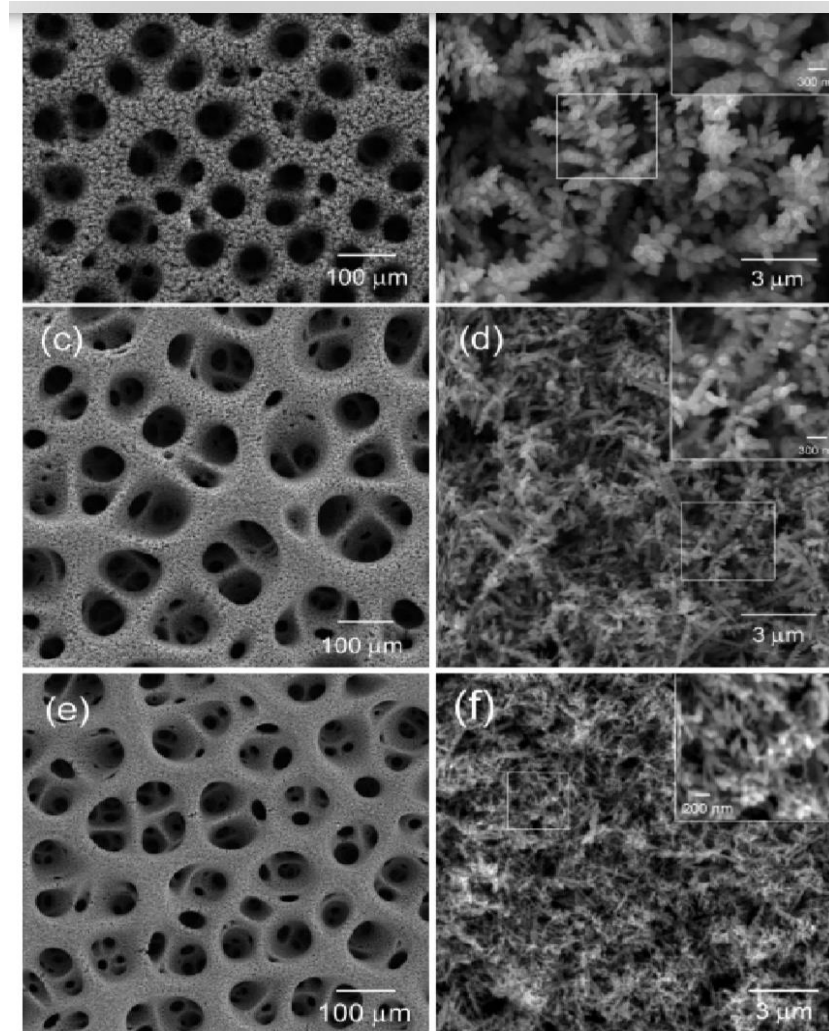


Figure 3 SEM images of copper electrodeposited for 20 s in electrolyte of 0.4 M $\text{CuSO}_4 + 1.5 \text{H}_2\text{SO}_4 + 1 \text{Mm}$ (a,b), 10mM (c,d), and 50 mM HCL (e,f) at an applied cell current density of 3 A/cm^2 . [90]

It may be followed by post-treatment or adding of additives to the electrolyte solution to enhance some properties of the deposited porous surface. **Table 3** illustrates the effect of some additives at different concentration ratios between CuSO_4 and H_2SO_4 .

Table 4 shows some fabrication methods of superhydrophobic copper surfaces which have numerous research laboratories around the world.

At the gas-liquid interface, the flux of bubbles to the bulk of the solution leads to bubbles grows. On a cathode surface, the bubbles gradually rise and coalesce before detaching from the surface. This ability of coalescence of bubbles with its size is related to its residence time on the surface.[91]

Table 3 The effect of additives on porous copper from hydrogen bubble

Additives	Effects	CuSO₄: H₂SO₄ (M)	Ref.
Na ₂ SO ₄	Increase bubble growth	0:2	[92]
CTAB*	Pores disappeared completely	<0.15: 0.04	[89]
(NH ₄)SO ₄ + BTA*	Mechanical strength and stiffness (Tightly interlocked needle-like nanodendrites)	0.2: 0.7	[35]
MPSA	Smooth and strong wall foam	0.4 : 0.7	[93]
Acetic acid	Bubble stabilizer	0.4 : 1.5	[94]
Cl ⁻	Reduce branches size and inner stress of foam wall	0.1 : 0.5	[95]

*CTAB: Cetyltrimethylammonium bromide * BTA Benzotriazole * MPSA Mercapto-1-propane sulfonic acid

Table 4 Different techniques and applications with water contact angles

Technique or method	Structure feature	Application	Contact angle	Ref
Template and etching	Hierarchical multi scale	Chemical and mechanical resistance	160°	[96]
Smoke deposition	Micro/Nano hierarchical	Separation of oil/water mixtures	164 ±0.8°	[97]
Oxidation & chemical modification	Bean sprout-like	Applications need thermal stability	150°	[98]
Hydrothermally synthesis	Carambola-like CuO film	Anticorrosion	157°	[99]
Solution-immersion	Micro-structure	Abrasion resistance	150°	[100]
Atmospheric pressure arc discharges	Micro/Nano hierarchical	Production of optically transparent SH coatings	150°	[101]

จุฬาลงกรณ์มหาวิทยาลัย
CHULALONGKORN UNIVERSITY

2.3 Graphene and its properties

Graphene is one of the latest miracle materials to be extracted from graphite. This SP² lattice and ultra-thin, two-dimensional crystal is atom-thick (1.42Å) and entirely composed of arranged carbon as a honeycomb-like pattern **Figure 4**. Although graphene is single layer of graphite, is considered a solution for many problems to its unlimited, remarkable properties and potential use in a wide range of practical

applications [102]. This is especially true for electronic device, photocatalysis, solar cells and optoelectronic device. It works as an excellent conductor with its tunable band gap and low density (2.267 g/cm^3). Therefore, it is a candidate for replacing silicon semiconductors to form a new generation of computer chips, including exceptional charge transport and charge collection. Graphene possesses a positive charge that absorbs ions. Its electron mobility is $2.5 \times 10^5 \text{ cm}^2 \text{ V}^{-1} \text{ S}^{-1}$ [103]. More importantly, dramatical enhancing of thermal conductivity has been reported. It has been utilized in manufacturing batteries that a high capacity with short charging time. In medical technology, graphene showed economically significant benefits as an optical probe for early diagnosis of cancer cell and tumor detection due to its luminescence, high thermal conductivity (above 3000 W mk^{-1}), and sensing of biomarkers [104]. Another benefit is its superior mechanical strength (130 GPa); therefore, materials that can be coated with graphene are expected to have better remarkable resistance to load with corrosion protection, and their strength can increase tremendously [105, 106]

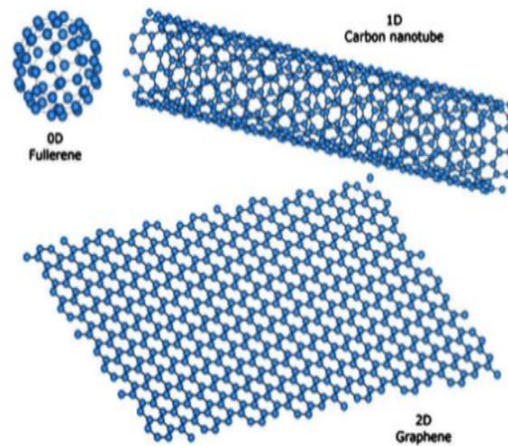


Figure 4 shows 2-dimension graphene, 1-dimensin carbon nanotube and 0-dimension Fullerene [107].

However, graphene is totally transparent due to its atom thickness and its being chemically inert. It has been found that the optical transparency property of graphene plays an important role in biological, and medical research by improving images. However, some reports challenge the “transparency of graphene coatings”. Thermally, at the graphene/ water interface, Kaptiza's length is higher 2.5 times than bare copper/ water interface but with a strong coupling between graphene and copper, this Kaptiza resistance becomes negligible [108]. Graphene has negative thermal expansion as the bond-bending cancels each other out in the plane graphene sheet. Theoretically, this optical transparency drops quickly with increasing the thickness as it has been reported that light transmittance decreased with an increasing number of graphene layers (see **Figure 5**) [103].

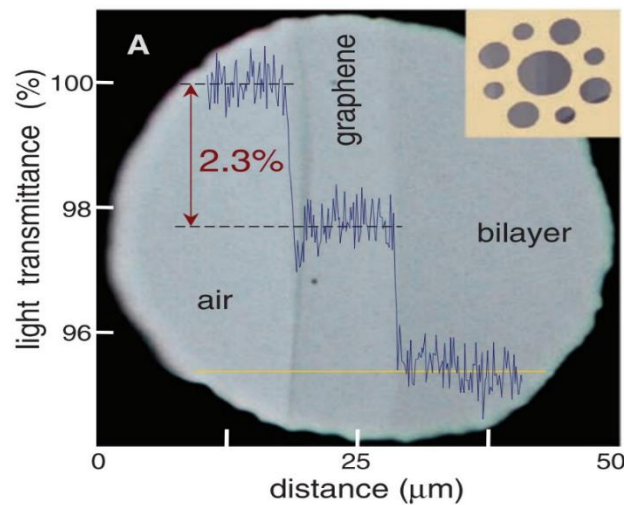


Figure 5 Light transmittance between air, graphene, and a graphene bilayer [103].

Despite the fact that graphene can generate economic benefits and has promising practical applications, some questions still need to be addressed. In this sense, it opens the door for more attempts to remedy and modify the graphene surface to overcome some challenges and be more efficient. It was reported that graphene could present fracture behavior. Using molecular dynamics simulation can detect this kind of failure behavior and discover where fracture begins, particularly near grain boundaries inside the high-temperature domain [109]. This fracture can be initiated in an armchair direction as decagon defects before expanding, resulting in pearl necklace-like structure [110]. Additionally, graphene has still been tested to solve many questions such as where and how fast cracks can propagate and what appropriate methods control of cracks. Eliminating such defects are essential to improve graphene toughness [111, 112].

2.4 Graphene coating techniques

Materials that can be coated with graphene are expected to have better properties such as corrosion protection, enhanced electrical conductivity and chemical resistance. Several feasible and efficient methods for graphene coating can include chemical vapor deposition (CVD), plasma-enhanced chemical vapor deposition (PECVD), roll-to-roll process, low-pressure chemical vapor deposition LPCVD, initiate chemical vapor deposition (iCVD), electrophoretic deposition (EDP), with aiming for uniformity, controllable thickness of graphene and good adhesion of the coated film [113]. All techniques depend mainly on the good preparation of the samples to be coated with graphene, the process condition, and the quality of graphene. The manufacture process of graphene can be completed simply by converting graphene oxide to graphene. The reduction of graphene oxide is possible by using reduction agents such as hydrazine [114]. A Raman spectroscopy is a method used to examine the quality of graphene [115]. However, like other materials, graphene tends to reduce its surface energy by forming agglomeration; therefore, there will be a kind of ununiform coatings [116]. As for the CVD technique, it has a high deposition rate, and it is a robust method, which does not require as high a vacuum as physical-vapor deposition (PVD), but it needs elevated temperatures and a control of pressure inside the chamber, which limits what kind of substrates can be coated, with the possibility of stress and the mechanical instability of the coated film due to different thermal expansion of the materials. The CVD consists of two steps. First, it performs kind of pyrolysis of a material to form carbons, such as exposing of copper foil to a CH_4/H_2 atmosphere at 1000°C , secondly, through the dissociation of carbon atoms to form

graphene structure [117]. It relies on the interaction between carbon atoms and a substrate [118].

By using plasma (a non-thermal energy source), in PECVD method, there is a chance for more efficient delivery and a distribution of carbon atoms with uninterrupted growth, which is widely used in integrated circuit manufacturing [119]. In this method, ionized plasma is generated above a substrate and diffused along a surface after bombarding the surface [120]. Another method is (iCVD) which is also called hot wire CVD. Compared to CVD, this economical technique is versatile, used in a wide range of applications, and can be conducted at a low temperature. The main difference between this and other methods is an initiator is used to heat up filament wires and start the process.

One of the promising techniques for graphene coatings and nanomaterials, which has many applications, is electrophoretic deposition EDP [121, 122]. This technique allows for obtaining thin and uniform graphene coatings on even complex objects (flat, cylindrical, porous, 3D) [123-125]. It can be conducted by charging a graphene nanoplatelet by using a conductive additive (polymer, ceramic, or metals) and using the influence of the electrical field to move these charged particles to an electrode of the opposite charge. **Figure 6.**

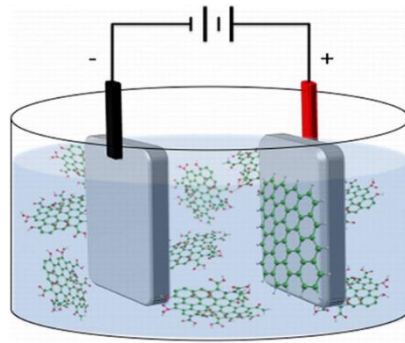


Figure 6 Electrophoretic Deposition of graphene.

2.5 Theory of wetting of the textured surface

2.5.1 Contact angle and surface tension

The angle at the liquid-solid interface is defined as a contact angle (θ), and from a contact angle value, a measuring of wettability is determined [126-128]. The contact angle of a drop decreases from an advancing contact angle θ_A to a receding contact angle θ_R ; the difference between these two angles is called the contact angle hysteresis. The dispersion out of a drop on a surface increase until ultimate spreading out or completing wetting with a zero contact angle [129, 130]. A liquid droplet can spread on a smooth surface until the cohesive force of the liquid equals the adhesion between the liquid and solid. Moreover, the spreading of the droplet continues until reaching a thermodynamic equilibrium between three phases: air, liquid, and solid surface [67]. Neglecting the effect of gravity, the system is assumed to be in an equilibrium state at constant temperature and pressure. The extent of wetting is calculated from free energy G' between three interfacial phases (Solid-Gas γ_{sg} , Solid-Liquid γ_{sl} , and Liquid-Gas γ_{lg}) which vary according to changes of the radii of sessile

liquid droplets **Figure 7** [131]. The following equations demonstrate how to derive the equilibrium value of the wetting angle from the free energy between each of the three phases **Figure 8**:

$$\frac{dG'}{dr} = 0 \dots\dots\dots(8)$$

$$\frac{dG'}{dr} = \gamma_{lg} \frac{dA_{LG}}{dr} + \gamma_{sg} \frac{dA_{SG}}{dr} + \gamma_{sl} \frac{dA_{SL}}{dr} = 0 \dots\dots\dots(9)$$

As area changes two relationships can be obtained:

$$\frac{dA_{SL}}{dr} = - \frac{dA_{SG}}{dr} \dots\dots\dots(10)$$

$$\frac{dA_{LG}}{dr} = \cos \theta \frac{dA_{SL}}{dr} \dots\dots\dots(11)$$

From equations (7), (8) and (9) we can obtain called is called Young's equation:

$$\cos \theta_Y = \frac{\gamma_{sg} - \gamma_{sl}}{\gamma_{lg}} \dots\dots\dots(12)$$

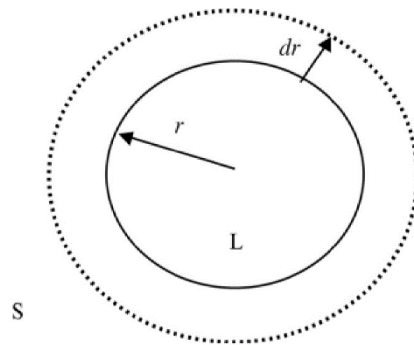


Figure 7 A projection of a sessile drop, incremental change of radius, solid (S) and liquid (L) [131].

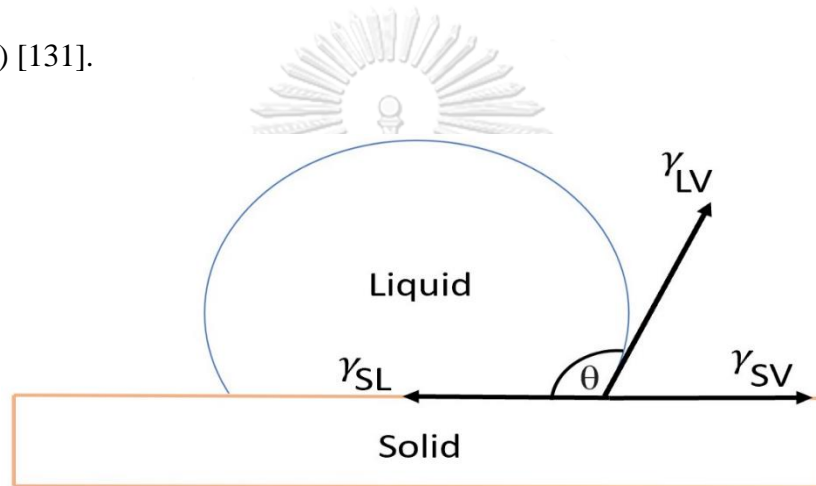


Figure 8 A schematic of the three interfacial tensions γ_{sg} , γ_{lg} , and γ_{sl}

The spreading out of a drop on a flat surface has a coefficient parameter that is also called spreading parameter **S** as a result of three interfacial tensions γ and is characterized as spreading tensions γ^{SLV} :

$$S = \gamma_{sg} - (\gamma_{sl} - \gamma_{lg}) \dots \dots \dots (13)$$

This coefficient S can be combined with Young’s equation to provide the Young-Dupre equation:

$$S = \gamma_{lg} (\cos (\theta)-1) \dots \dots \dots (14)$$

In which S equals zero; therefore, $\cos(\theta)=1$, which is only when the contact angle (θ) is zero (complete wetting).

Surface tension is considered one of the essential parameters in many applications and is defined as the energy supplied to increase the surface area by one unit [132]. In other words, fluid surfaces tend to shrink into the minimum surface area possible and act at the boundary between two presented phases (liquid-solid or liquid-gas or solid-gas) [133, 134]. The surface tension as a phenomenon can be observed in the nearly spherical shape of a small drop of liquid. It is measured in force per unit length [135].

$$\gamma = 1 \frac{\text{dyn}}{\text{cm}} = \frac{10^{-7} \text{m.N}}{10^{-4} \text{m}^2} = 0.001 \frac{\text{J}}{\text{m}} \dots\dots\dots(15)$$

In an early experiment, Laplace introduced a mathematical expression of wetting phenomena including surface tension and capillary rise in a tube [136] (see **Figure 9**). His equation gives the relation between different parameters: final height h of a liquid to which liquid rises, tube diameter D , the surface tension of a liquid γ , its density ρ , acceleration due to gravity g and contact angle θ_a which can be written as follows:

$$h = \frac{4\gamma \cos \theta_a}{\rho g D} \dots\dots\dots(16)$$

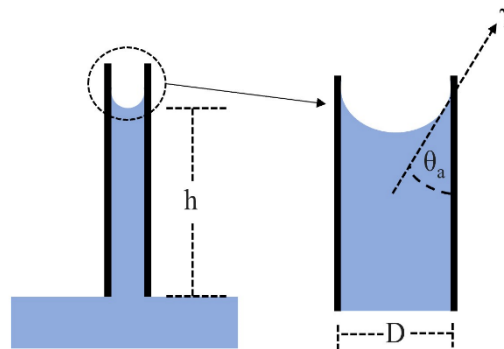


Figure 9 The depiction of the rise of liquid inside a small-diameter vertical tube [136].

The effect of interfacial tensions is also of paramount importance and relevance to the thermodynamic work of adhesion ΔW_{SLV} , which via the Young-Dupre equation is defined as [137]:

$$\gamma_{LV}(1+\cos \theta) = \Delta W_{SLV} \dots\dots\dots(17)$$

Moreover, during the wetting, the area between the solid and the liquid droplet A_{SL} increases until the surface energy becomes zero [52]. In the spreading process, the work change δw can be written as:

$$\delta w = \gamma_{SL}dA_{SL} + \gamma_{LG}dA_{LG} + \gamma_{LV}dA_{LV} - kdL + PdV + VdP, \dots\dots\dots(18)$$

Where L , k , and dV are the length of the three-phase contact line, the energy per unit length associated with contact line tension, and the change in volume, respectively [59, 138, 139].

Table 5 Surface tension of some liquid [140].

Liquid	Surface tension (mN/m)
Deionized water	72.3
Hexadecane	27.3
Glycerol	63.4
Dimethyl malonate	36.5
Ethanol	25.6

In the case of flow conditions, another liquid contact angle on a surface is called dynamic contact angle θ_D which may be smaller or larger than the Young contact angle and related to the movement of the triple line due to excess force:

$$F(\theta_D) = \gamma_{SV} - \gamma_{SL} - \gamma \cos \theta_D \dots \dots \dots (19)$$

Moreover, the dynamic contact in term of advanced contact θ_A and receding contact θ_R can be calculated according to droplet volume:

$$F_s = kw\gamma_{lv} (\theta_A - \theta_R) \dots \dots \dots (20)$$

(where F_s is the interfacial force, the k constant depends on droplet shape, and w is the width of the droplet) [141, 142]. It can be understood from equation (12) that the mobility of a droplet increases by reducing contact angle hysteresis ($\theta_A - \theta_R$), which is related to the force balance of a droplet for a non-horizontal plane [143]. Additionally, when considering the effect of droplet velocity and its impact on surfaces, a different kind of wettability behaviour can be deduced from **Figure 10** . The contact diameter

of a water droplet on the surface increases with increasing impact velocity V , which can impale the surface deeper.

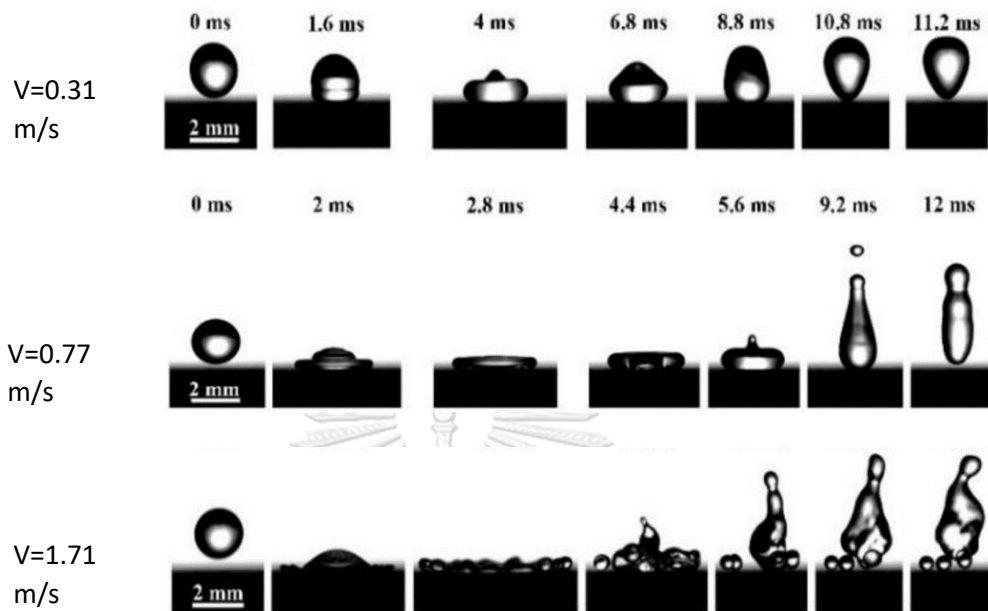


Figure 10 Water droplets impinging on the superhydrophobic surface with different velocity and time of contact on the surface [144].

At a nano or micro-scale in case of a nanodroplet, Laplace pressure becomes a dominant force. Therefore introducing V_{dp} is suggested by Jasper, which is related to droplet volume and has been found that contact angle measurement is less than that of a microscale [145]. This variation of pressure happens because of Laplace pressure is proportional to the droplet's curvature. Modified Young equation with Laplace pressure yields an equation including surface energy, Laplace pressure P , and the droplet's curvature [146]:

$$P = \gamma_{LV} \left(\frac{1}{R_1} + \frac{1}{R_2} \right) \dots \dots \dots (21)$$

R_1 and R_2 are radii of droplet curvature [3]. The analysis of a change in the nanodroplet volume from a sphere shape to a sphere cap on a surface can be observed by modern microscopic devices and computer modeling for the analysis of nanodroplets wetting behavior [147].

It can be concluded here that a higher liquid-vapor surface tension (high cohesive force of liquid molecules) compared with a low substrate-liquid interaction (low adhesive force) implies a higher resistance of a liquid to spreading out and so a poor wettability. More specifically, the wetting of a surface is favorable with less than 90 of the contact angles.

2.5.2 Types of pore and capillary pressure

Different types of pores can be observed, such as blind pores, closed pores, through pores, and cross-linked pores. **Figure 11** and **Figure 12** show different types and shapes of pores [148-151]. Pore geometry, pore throat, and pore distribution are also related to capillary pressure and can be evaluated using techniques such as SEM or TEM [152-154]. This capillary pressure is dependent on the pore structure and is an important factor in demonstrating the transition zone fluid behavior in different wettability states [155]. It can be defined as the difference in pressure across any curved interface between two immiscible fluids [156]. **Fig. 13.** In the capillary tube, a force balance over the meniscus of a liquid between the pressure in nonwetting fluid p_{nw} and pressure in wetting fluid p_w leads to the equation:

$$p_{nw}\pi R_c^2 = p_w\pi R_c^2 + \gamma \cos \theta (2 \pi R_c) \dots\dots\dots(22)$$

Capillary pressure p_c is different between p_{nw} and p_w , equation (13) yields

$$p_c = \frac{2\gamma \cos \theta}{r} \dots\dots\dots(23)$$

From equation (18) and (19) the capillary pressure is then

$$P_c = \rho g h \dots\dots\dots(24)$$

For the water-air interface, equation (16) becomes

$$P_c = (\rho_w - \rho_a) g h \dots\dots\dots(25)$$

Where ρ_w is the density of water and ρ_a is the density of air.

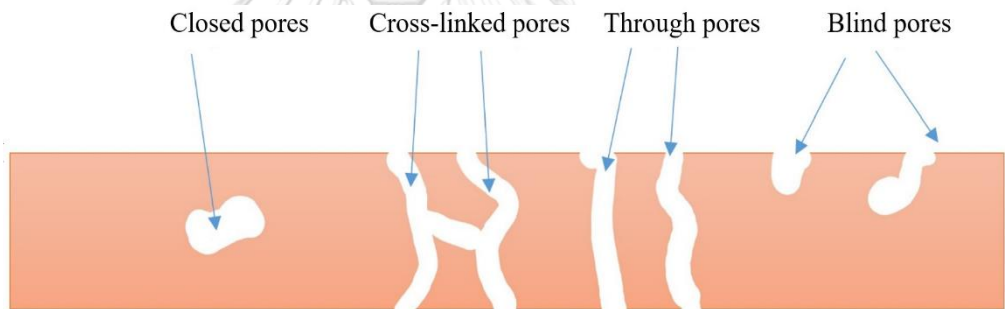


Figure 11 Schematic images of pore types

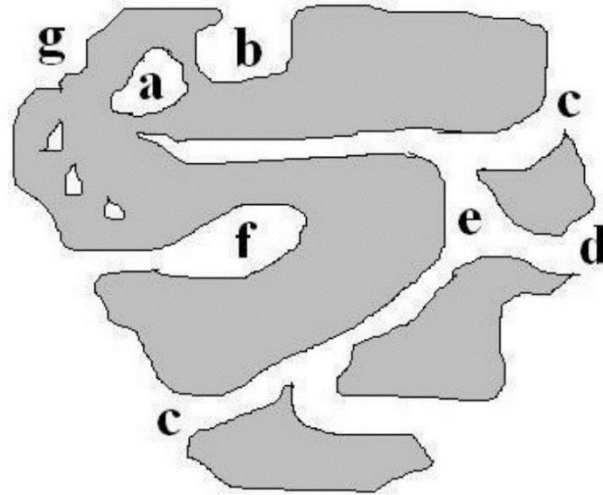


Figure 12 Types of pore (a) closed, (b,c,e,f) open, (b,f) blind or dead-end/saccate, (f) through, and shape of pores are (b) ink-bottle shaped, (c) cylindrical open, (d) funnel shaped, (f) cylindrical blind, and (g) roughness [157].

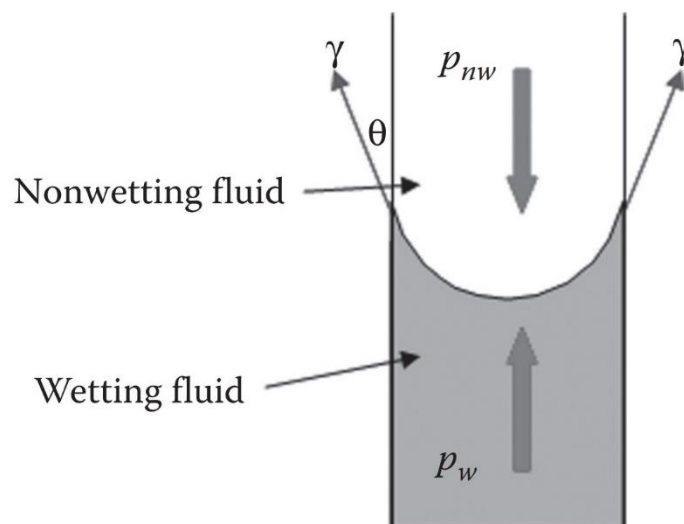


Figure 13 The meniscus in a capillary tube [158].

It has been reported that the entry capillary pressure is an important factor for liquid drainage and is wettability depended as it can enhance the entry of the non-wetting phase into pores [159].

Due to the form of liquid-air interface underneath the droplet, capillary pressure (anti-wetting pressure) is formed because of the bending of a droplet after it impacts a solid. In cases when the capillary pressure is less than dynamic pressure and water hammer pressure, the wetting phenomena are completely on the surface which is considered to be one of dynamic behavior of water both in contact processes and spreading processes [144].

2.5.3 Wenzel's theory

In 1936, Wenzel described the effect of surface roughness r on the wettability of a homogenous surface and proposed an equation based on the complete wetting of a rough surface. According to the Wenzel model as a classical situation of a droplet on a flat surface, the liquid penetrates between the grooves of a structure, and it is not valid for a heterogeneous surface **Figure 14** [63, 160]. Wenzel modified Young's equation, which demonstrates the relationship between three factors: equilibrium contact angle (Young angle θ_Y), roughness factor and apparent contact angle [161].

$$\cos \theta_A = r \cos \theta_Y \dots\dots\dots(26)$$

The roughness factor r ($r \geq 1$) is the ratio between the actual area and the projected area, and it equals one for a smooth surface. **Figure 15** shows the relation between the minimum value of the roughness factor (r) to promote the complete spreading of a liquid and contact angle on a smooth surface. When r is greater than one, it indicates

that the true surface area is larger than the apparent surface. Moreover, the less θ_Y is than 90° , the more enlarged the contact area is and the more hydrophilic the surface is. On the other hand, if θ_Y is higher than 90° , the more hydrophobic the surface is (see **Figure 16**) [162, 163]. Therefore, the roughness factor enhances either the hydrophobicity or hydrophilicity of a surface (see **Figure 17**). On the surface area, roughness value can be calculated with roughness profile parameters. R_a (arithmetic mean deviation) is the most common parameter with other parameters R_q (root mean square RMS) and R_z (ten-point high) [164].

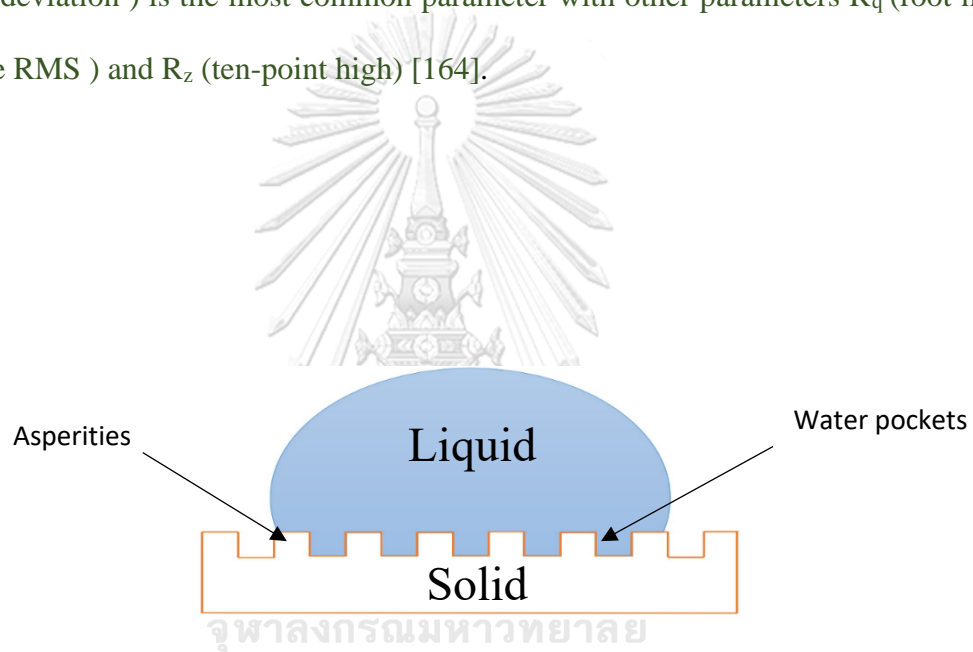


Figure 14 A schematic diagram of Wenzel state

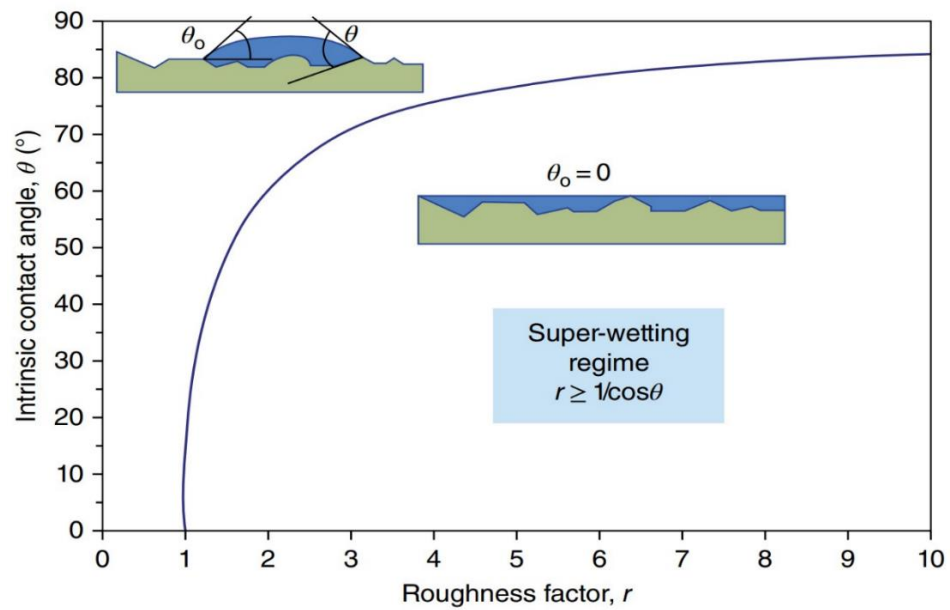


Figure 15 Roughness factor (r) with varying Young's intrinsic contact angle [165]

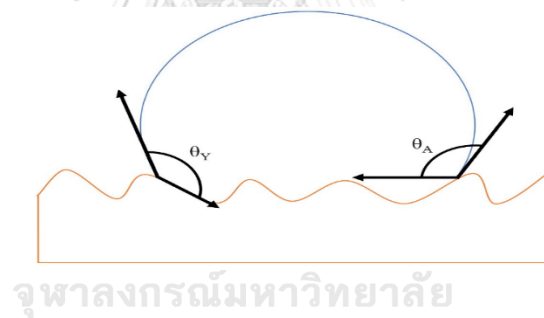


Figure 16 A schematic diagram of Young contact angle θ_Y and apparent contact angle θ_A

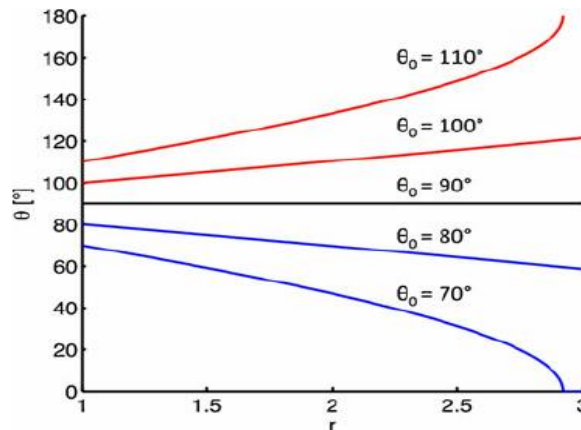


Figure 17 Increasing surface roughness with different measurements of contact angles described by Wenzel equation

2.5.4 Cassie-Baxter theory

Cassie-Baxter theoretical modeling takes place on heterogeneous surfaces (common in nature) and includes a solid-air interface. Cassie-Baxter proposed that liquid remains upon the asperities with less physical contact and does not penetrate because of the presence of trapped air-pockets [166] (see **Figure 18**). The equation of this highly non-wetting state of Cassie-Baxter can yield the following:

$$E_D = f_1 (\gamma_{LS} - \gamma_{SA}) + f_2 \gamma_{LA} \dots \dots \dots (27)$$

$$\cos \theta = 1 + f_1 (\gamma_{LS} - \gamma_{SA}) \dots \dots \dots (28)$$

Where E_D is the net energy of the solid-air interface and liquid-solid interfacial energy, f_1 is the total area of the solid-liquid interface, and f_2 is the total area of the liquid-air interface. Therefore, under a droplet, two interfaces are involved, f_1 and f_2 , which in total equal one ($f_1 + f_2 = 1$).

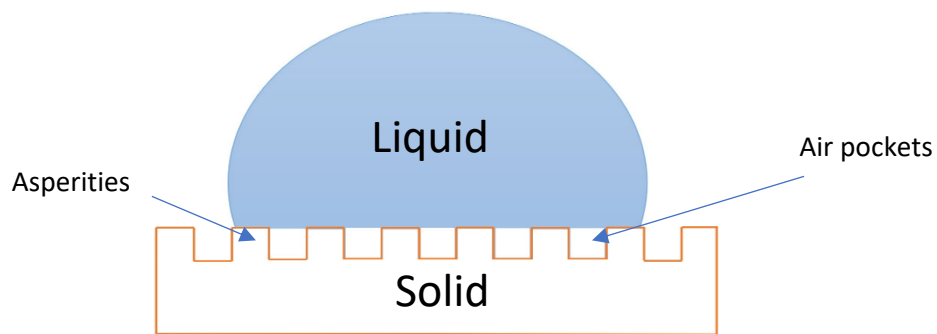


Figure 18 A Schematic diagram of Cassie-Baxter state

2.5.5 Transition between Wenzel and Cassie-Baxter states

When liquid penetrates the groove of a surface, the transition from Cassie-baxter state to Wenzel state is taking place. It occurs in the case of an external force, such as pressure or vibration applied to the liquid. It is reported that increasing Laplace pressure induced this transition [63]. Additionally, altering of surface roughness or increasing such as structure's holes depth, making the shift from Cassie-Baxter state to Wenzel state easier [167, 168].

Interestingly on a nanoscale, it has been reported that shallow and thick nanoholes of surface results in a Wenzel state; however, deep and thin nanoholes lead to a Cassie-Baxter state. Also, in nature or modified surfaces can exhibit a mixture of these two models, but Cassie-Baxter is more dominant in the case of high and radii artificial nanopillars [169, 170]. The transition of a surface from hydrophobic to

superhydrophobic through post-treatment means that a surface is transmitted from a Wenzel state to a Cassie-Baxter state [171].

A Third wetting behavior is called partial Cassie-Baxter wetting, which is in between the stable sticky Wenzel mode and the unsticky Cassie-Baxter mode [172, 173]. Because of a mixture of both wetted grooves and trapped air-pockets underneath droplets, this behavior introduces pinning droplets as the droplets do not wholly penetrate the surface, minimizing rapid transition from partial to full wetting. Droplets can be pinned if any deformation of a surface occurs, as air can be trapped between the droplet meniscus and surface texture [174]. It should be mentioned here that those two models with their transition behavior, are currently some of the primary instructions of the design of a superhydrophobic surface [170, 175].

2.5.6 Wetting and Adsorption

Wetting and adsorption are strongly related, and especially when considering adsorption of the vapor of a volatile liquid droplet on a solid surface. It is also possible to determine $(\gamma_{sv} - \gamma_{sl})$ from vapor isotherms, relating the surface concentration Γ (mole/ unit area) to the relative equilibrium pressure (p/p_0) in the gas phase [176] **Fig.19**. Therefore, the surface pressure of the solid-vapor interface $\pi^{sv}(\Gamma)$ can be written as in Figure 19:

$$\pi^{sv}(\Gamma) = \gamma^s - \gamma_{sv}(\Gamma) = \mathbf{RT} \dots \dots \dots (29)$$

Where γ^s is the surface tension in the vacuum of a pristine surface S, $\gamma_{sv}(\Gamma)$ is the surface tension of the same surface containing Γ molecule of vapor molecules, R is the gas constant, and T is the absolute temperature. It can be concluded that charging solid surfaces due to the adsorption of charged species is related to the solid-liquid tension.

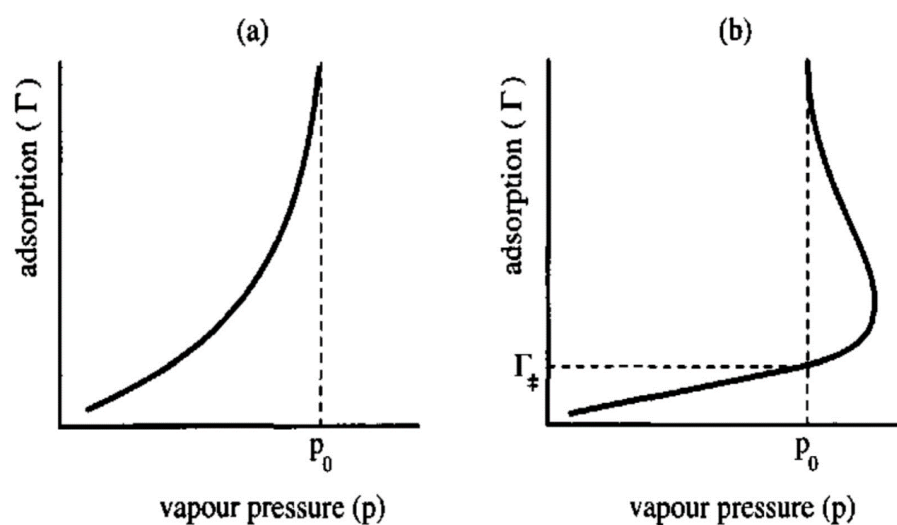


Figure 19 Vapor adsorption isotherms for (a) complete wetting and (b) partial wetting. The dashed line represents the saturation axis (i.e., the saturated vapor pressure).[176]

2.5.7 Correlation between copper and graphene

Both copper and graphene have high thermal conductivity and graphene can work as a passivation layer that inhibits the surface oxidation of the copper surface substrate.

Controlling the incorporation of graphene coatings with other materials particularly on transition metals such as copper attracted many researchers [177-179]. Functional

coupling with homogenous growth results in covalent and ionic bonding on the graphene /copper interface [180]. Electrons travel from the copper surface to a graphene-based on Fermi-level variations through the interface. Yinbo Zhao, found that the intact graphene monolayer coatings on the copper surface with nano notches is behind the strengthening of copper surface, and concluded that there would be a kind of misfit stress coming from the mismatch of lattice and shear modulus between copper (45 GPa) and graphene (280 GPa) at the interface [110, 181]. Adhesion between graphene and other materials can be calculated from the work of adhesion:

$$W_{st}=\gamma(1+\cos\theta)\dots\dots\dots(30)$$

Atomic geometry is correlated with strength and electronic structure. Compared to the other materials, the Graphene/ Nickel interface has much more cohesive energy than the graphene/ copper interface because of strong coupling between open d-orbitals,. Copper's lattice constant (3.597 Å) is the same as that of graphene. The binding energy E_b of the graphene sheet and metal substrate is calculated as

$$E_b = E_{C-M} - (E_C + E_M) \dots\dots\dots(31)$$

Where E_{C-M} is the energy of a hybrid system, E_C is the energy of the graphene sheet and E_M is the energy of metal substrate [182].

Thermal resistance at the interface graphene-coated copper is absorbed [108]graphene allows only 18 % of Van Der Waal energy of underneath copper to transmit. The need to transfer the graphene layer from copper foil to other substrates by using such liquid-assisted transfer or thermal tape [183]

In the case of the oxidation, the layer occurs on the copper surface such as Cu_2O , the nucleation density of graphene decreases as Cu_2O thickness increase because this oxide layer prevents the dissolution of carbon on the copper surface. [184]. Moreover, It has been reported that the stability of graphene on the copper surface increased with time depending on the quality of both graphene and copper surface [185].

Table 6 Structure (interface distance D_{C-M}) and properties (interface binding energy E_b and mechanical strength σ_s) of Graphene-copper and Graphene-Nickel [182].

Metal	D_{C-M} (Å)	E_b (meV Å ⁻²)	σ_s (GPa)
C-Cu	2.243	24.81	2.92
C-Ni	2.018	91.33	18.70

2.5.8 Wetting behavior and transparency of graphene

It is reported that graphene is wetting-transparent for many metals, such as copper and silicon because it is thinner and domination of van der Waal forces. When van der Waal forces are not dominated and only short-range chemical bonds exists, such as in glass as a substrate, graphene is not considered wetting transparency. Taking advantage of this property results in the excellent stability of a gradient degree wetting surface by blocking any kind of chemical or airborne contamination from the surrounding environment [186]. Unchanged water contact angles of substrates are the key to determining the quality of the unique transparency of graphene. This transparency can be understood in terms of how graphene affects the adsorption

energy of water on a substrate. Adsorption of water to the graphene surface is a slow process due to the resistance to saturate according to the level of humidity [187].

However, a report showed that graphene is partially transparent to wetting and not completely transparent, especially for superhydrophobic or superhydrophilic substrates. This incomplete transparency is due to that van der Waal forces are not dominated; which are responsible for the transmission of the substrate contact angle to fluid above graphene [188].

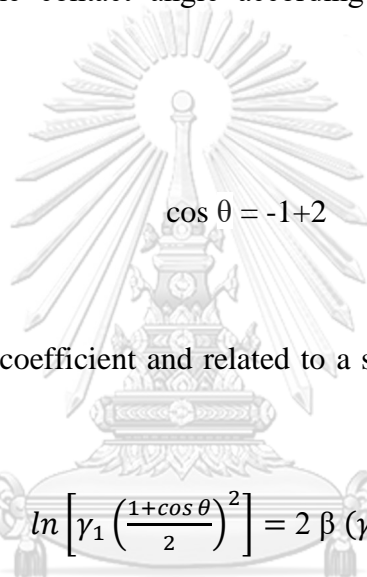
Apart from other effective factors such as water content and graphene coating condition, measurement of contact angle on graphene as an isolated layer is a simple way to investigate the wetting properties of graphene [189]. It was observed that water molecules do not strongly bind to a graphene sheet [190]. However, it is still controversial that whether graphene is hydrophobic or hydrophilic, but some experimental reports show that the initial process of producing graphene is reflected that the graphene sheet is hydrophobic or hydrophilic [191]. Some reports showed a changeable behavior of graphene hydrophobicity to hydrophilicity by using chemical additives or ultraviolet radiation [115, 192]. For instance a combination of acetone and water as a solvent shows a wide range of water contact angles on the graphene surface due to chemisorption of acetone on graphene in any defects of graphene surface [192]. In terms of a graphene oxide film, it is considered hydrophilic due to the strong hydrogen bond interaction. Moreover, in the presence of any defects, there is a kind of relatively increasing water contact angle measurement [193].

As with other metals, adhesion between graphene and liquid can be calculated from the work of adhesion:

$$W_{sl} = \gamma (1 + \cos \theta) \dots \dots \dots (32)$$

The contact angle of graphene is larger than that of graphite due to differences in surface energy. Wang determined that the surface energy of graphene is 62mJ/ m² and of for graphene oxide is 46.7 mJ/m² using the equation of state theory [194]. Using Neumann, which is more reasonable when compared with other approximation methods based on the equation of state theory, one can determine the surface free energy of graphene. The contact angle according to Neumann’s equation is as follows:

-



$$\cos \theta = -1 + 2$$

$$\sqrt{\frac{\gamma_s}{\gamma_l}} e^{-\beta (\gamma_s - \gamma_l)^2}$$

Where β is the constant-coefficient and related to a specific solid surface. Arranging the equation results in:

$$\ln \left[\gamma_1 \left(\frac{1 + \cos \theta}{2} \right)^2 \right] = 2 \beta (\gamma_s - \gamma_l)^2 + \ln (\gamma_s) \dots \dots (34)$$

By plotting the left side against γ_l , it can result in a parabola curve and fitting it with the second-order polynomial equation will help to determine the parameters β and γ [194]. **Figure 20.**

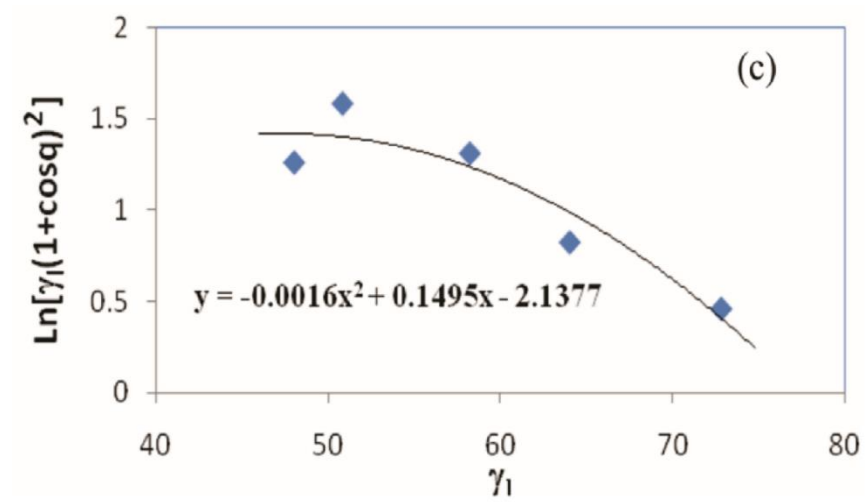


Figure 20. The surface energy according to Neumann's equation



2.6 Water Desalination across Nanoporous Graphene and through graphene multilayers as membranes

A desalination membrane is closely related to the materials from which it is made. Although some materials have been used as membranes for water desalination, such as Zeolite and Silica, research still needs to be done to control the cost of replacing membranes and improving the salt rejection rate. However, with the creation of nanopores on the single-layer graphene [195] by plasma etching [196] Fig. 23, there is an opportunity to filter out NaCl salt more effectively, thereby improving durability of the membranes with high salt rejection rate. The performance depends on pore size and tuning the wettability of the pores themselves (Fig. 24).

This effective water desalination of using nanoporous single-layer graphene can also be achieved through the channels of multilayer graphene oxide GO (contact angle around $34\pm 2^\circ$) or reduced graphene oxide (contact angle $76\pm 5^\circ$). Here, the performance mainly depends on the interlayer distance between graphene multilayers and the hydrophilicity of GO layers to enhance water flux with chemical resistance. Furthermore, recently there is a tendency of many researchers to investigate the fabrication of hybrid membranes of graphene oxide or reduced oxide membranes with other metals such as polydimethylsiloxane PDMS (as the hydrophobic metal) to control the wetting behavior and improve salt rejection to reach 100%. [197, 198] or with copper to give the membranes additional antibacterial properties [199]

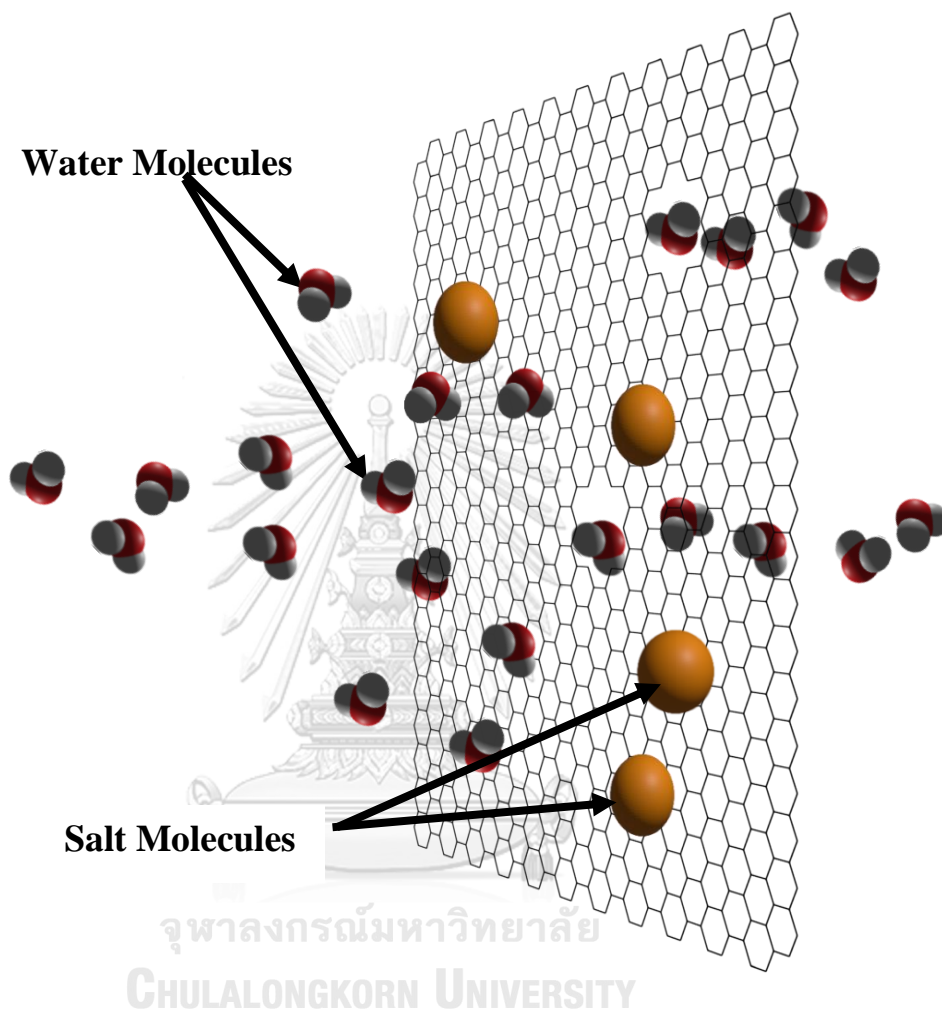


Figure 21 The permeability of water molecules through the defected area of graphene sheet and rejection of salt molecule by a graphene sheet

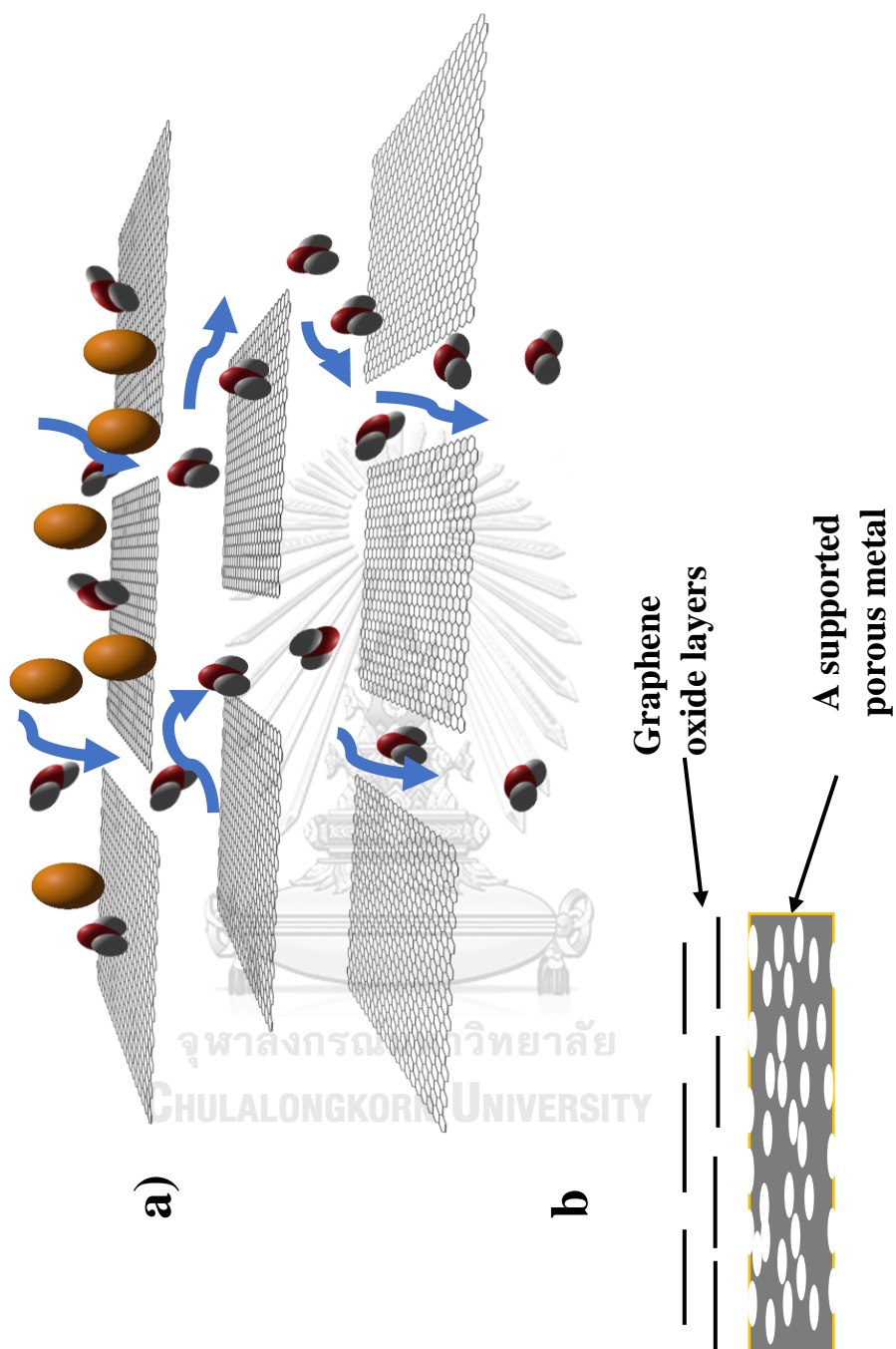


Figure 22 a) The diffusion of water molecules through the channels of the graphene oxide layers and the rejection of salt. b) Graphene oxide layers on a porous supported metal.

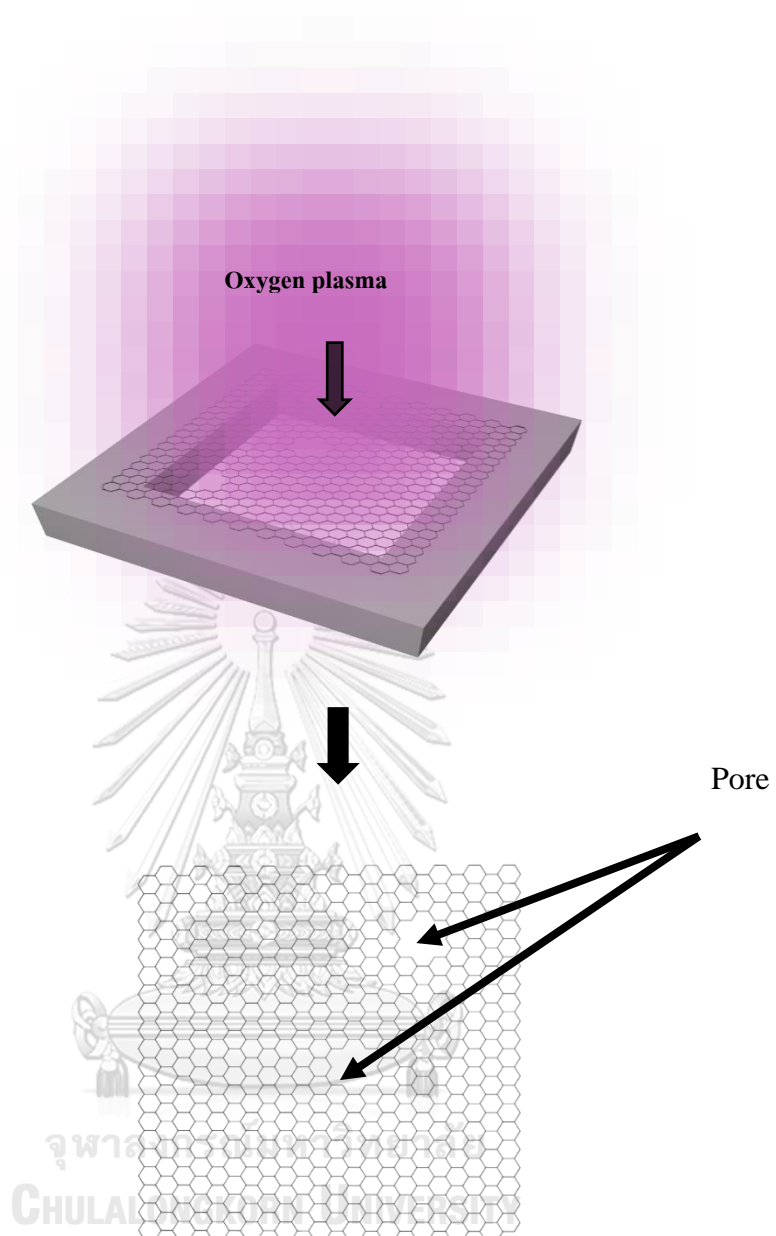


Figure 23 A schematic of Oxygen Plasma synthesis method for creating pores on a graphene sheet

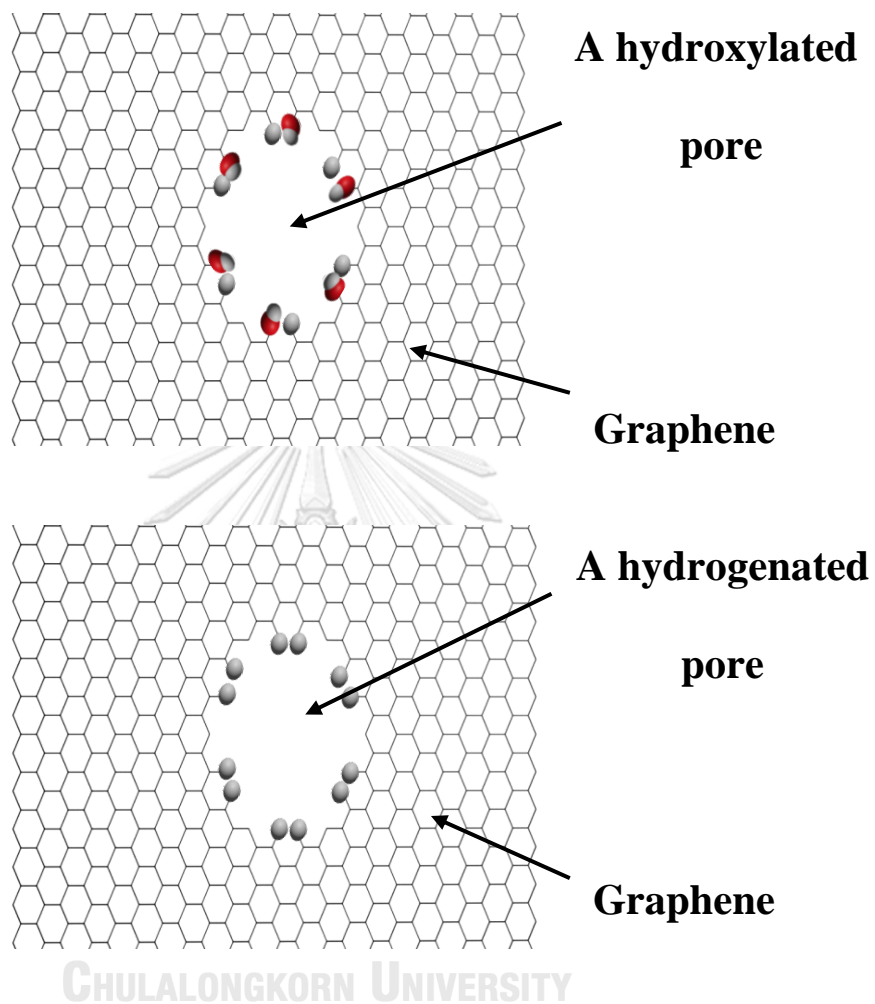


Figure 24 a) a hydroxylated pore (hydrophilic), b) a hydrogenated pore (hydrophobic)

CHAPTER III EXPERIMENTAL PROCEDURE

Part 1 Effects of plating and storage conditions on the wettability of electrodeposited porous copper surfaces

The objectives of this part:

- To compare the effect of electroplating conditions on developments of nano/microstructure of copper surface.
- To obtain the understanding of the wetting stability of porous copper surface.

This part demonstrates a method to modify the wetting characteristic of copper surfaces by developing porous structure via the promotion of hydrogen bubbles. Subsequently stored in different conditions, including air, water, and saline solution to assess the possible influence of storage conditions on the wetting behavior.

3.1.1 Sample preparation and fabrication

Porous copper samples were prepared by electrodepositing copper onto mirror-finished copper plate substrates (2x2 cm). Three acid copper plating baths (300 cc), named A, B, and C, with different concentrations of CuSO_4 and H_2SO_4 , as shown in Table 7 were explored. All 3 baths comprise CuSO_4 with contents lower than those normally used for monolithic copper plating and have relatively higher concentrations of H_2SO_4 than CuSO_4 to promote hydrogen evolution.

Table 7 Electrodeposition parameters of the porous copper samples in 6 groups under investigation

Samples	Electrolyte composition	Current density (A/cm ²)
	(Molar ratio) CuSO ₄ : H ₂ SO ₄	
A-1	0.1: 0.125	0.05
A-2	0.1: 0.125	0.125
B-1	0.1: 0.25	0.05
B-2	0.1: 0.25	0.125
C-1	0.4: 0.7	0.05
C-2	0.4: 0.7	0.125

The applied current densities under investigation are 0.05 A/cm² and 0.125 A/cm² for samples in set 1 and set 2, respectively. A platinum mesh was used as an anode (15x5 cm), and the distance between the 2 electrodes was kept at 2 cm. The prepared copper substrates were activated in 5 wt. % H₂SO₄ for 5 s and cleaned with distilled water before electrodeposition sessions, which were carried out at room temperature. Immediately after electrodeposition, the samples were rinsed well with deionized water and dried. For the case of the as-deposited samples, the samples were cleaned after deposition, dried for about 20 minutes and the wetting contact measurements were made directly.

3.1.2 Storage condition test

The electrodeposited copper samples from the 6 groups, as presented in Table 7, were subsequently stored in air (room temperature, 30-40% humidity). Additionally, the samples from groups C-1 and C-2 were also stored in deionized water and in saline water (concentration of salt = 3 wt.%) for a period of 4 weeks with weekly inspection. For these conditions, the samples were placed in beakers containing 300 cc of liquid. The beakers were well-sealed to prevent contamination.

3.1.3 Sample characterization

The microstructure and surface morphology of the electrodeposited samples were examined with SEM (Hitachi SU3500). CLSM (LEXT OLS4000) was employed to characterize the roughness profiles of the sample surface. The chemical composition of the electrodeposited copper was analyzed using EDX (Hitachi SU3500) and XRD (Bruker D8). The contact angles of the samples were measured with a goniometer (DropMaster V.3) and analyzed with FAMAS software based on the tangent method whereby a droplet 's profile is captured. Three sets of contact angles were determined, namely (i) advancing contact angle θ_A , (ii) receding contact angle θ_R measured after relaxing time of 300 s, and (iii) sliding contact angle θ_S measured with a tilted platform. The difference between θ_A and θ_R constitutes hysteresis. To steadily apply a water droplet onto a sample surface (4 μ L), a sample sitting on a movable stage was directed upwards to make contact with a water droplet that was released from a syringe's needle tip. The stage was then slowly moved downwards, rendering

a droplet adhered on a sample surface. The contact angle measurements were made at the center of each specimen to avoid the high-current electroplated area at the sample edges. The ImageJ software was also used to calculate porosity of the deposits.



Part 2 Tailoring the wettability of copper surfaces by dropping of graphene solutions

The objectives of this part:

- To understand the correlation between copper deposition and observed wetting characteristics of graphene.
- To examine the feasibility of controlling the wettability of electroplated copper surfaces by employing of graphene.

This part demonstrates a scalable, economical way to add graphene to flat copper substrates and electro-deposited porous copper surfaces through graphene droplets. The drops have different concentrations of dispersed solution and re-dispersed solution of graphene with and without using sodium dodecyl sulfate (SDS) surfactant.

3.2.1 Sample preparation and fabrication

The same as part (3.1.2), but in this part, the investigated applied current densities for porous copper surfaces were 0.125 A/cm² for samples (C*-Sol1, C*-Sol1', C*-Sol2, C*-Sol2'), C stands for a copper flat substrate and C* for a porous copper substrate as illustrated in Table 9, and 3 A/cm² for samples (D*, D*-Sol1). The sample D* is same as D*-Sol1 but D*-Sol1 with dropping graphene from solution Sol1. The idea of investigating additional samples (D*, D*-Sol1) to fulfill also whether graphene has a limit effect on the wettability or the physical effect can be dominated and assist the effect of different morphology with and without graphene. Also in this part four

different concentrations of graphene solutions were prepared using the 0.5 mg/mL ratio of graphene sheets (from XFnanO company (95 % purity)) with DI water with and without sodium dodecyl sulfate (SDS) surfactant. Moreover, graphene nanoplatelet powder from Graphene Tech Company from USA with 99.5 % purity was used to compare its Raman spectra with Raman spectra of graphene sheets. **Fig.25** shows the process of depositing multilayer graphene on copper surfaces. **Fig.26** shows the four solutions a) immediately after 30 minutes sonification which used for deposition and b) after three days.

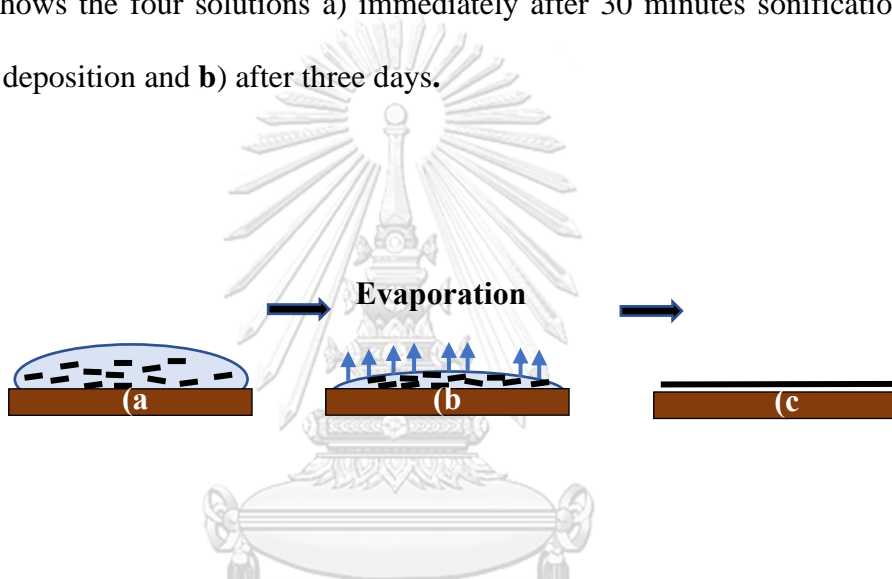


Figure 25 The process of graphene deposition on copper surfaces

For more details, **Table 8** illustrates the derived names of solutions, while **Table 9** shows the derived names of the samples.

Table 8 illustrates four names of different graphene solutions

Solutions	Description
Sol1	Solution (0.5mg/mL) of graphene with SDS surfactant
Sol1'	Re-dispersed solution from Sol1 by diluting with DI-water (1:30)
Sol2	Solution (0.5mg/mL) of graphene without SDS surfactant
Sol2'	Re-dispersed solution of Sol2 by diluting with DI-water (1:15)

Table 9 illustrates the names of each sample in detail

Samples	Sample details
C	A bare copper substrate
C- Sol1	A dispersed graphene solution of Sol1 on C
C- Sol1'	A dispersed graphene solution of Sol1' on C
C- Sol2	A dispersed graphene solution of Sol2 on C
C- Sol2'	A dispersed graphene solution of Sol2' on C
C*	A porous copper surface
C*- Sol1	A dispersed graphene solution of Sol1 on C*
C*- Sol1'	A dispersed graphene solution of Sol1' on C*
C*- Sol2	A dispersed graphene solution of Sol2 on C*
C*- Sol2'	A dispersed graphene solution of Sol2' on C*

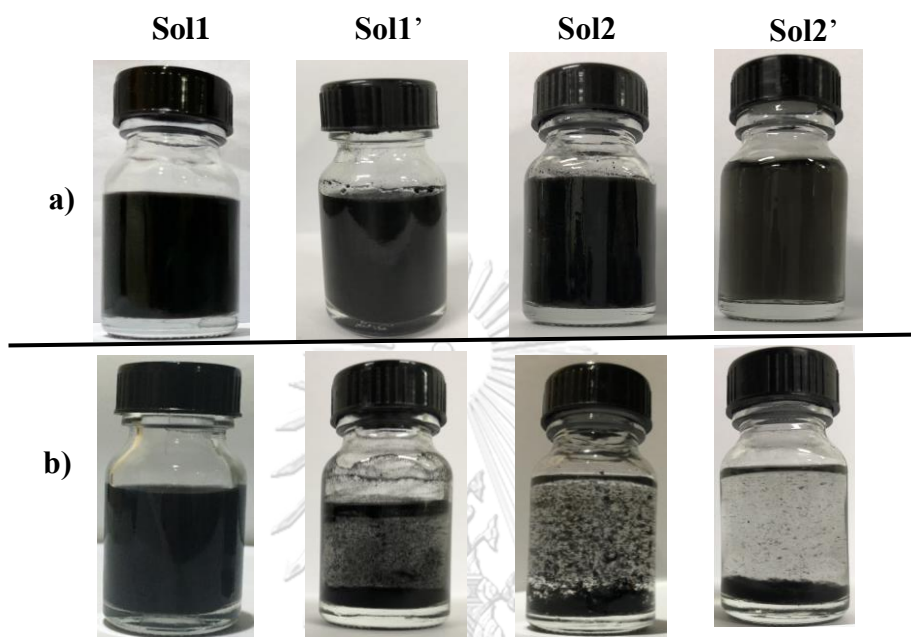


Figure 26 Graphene solutions (Sol1, Sol', Sol2, Sol2' a) after 30 minutes sonication b) after three days

3.2.2 Sample characterization

Same as (3.1.3) for contact of angle measurement for one month and for SEM images. In this part, additional characterization with Raman spectroscopy was used to characterize the presence of graphene and to analyze the different wetting behavior of samples. Transmission electron spectroscopy (TEM) was used for a more detailed morphology and topographic evaluation of graphene. The TEM grid samples were prepared by dropping approximately 3 microliters of Sol1 solution and another sample of Sol2 solution into TEM copper grids, followed by natural air drying.

CHAPTER IV EXPERIMENTAL RESULTS AND DISCUSSION

Part 1 Effects of plating and storage conditions on the wettability of electrodeposited porous copper surfaces

4.1.1 Characteristics of the copper electrodeposits

The copper electrodeposits of all groups were prepared successfully and were characterized by uniformly porous layers. As shown in **Fig. 27** (A-1, B-1 and C-1), samples from groups A and B exhibit similar porous structures, with B having a slightly more refined deposit structure and more uniform pore size distribution. This reflects the relatively lower surface roughness of group B samples, as assessed by laser confocal microscopy. The samples in group C, on the other hand, are characterized by a different surface morphology composed of relatively round and large, accumulated granules of copper deposits with interconnected pores in between. Additionally, it can be observed that the samples in all groups exhibit hierarchical arrays of micropores (i.e., large pores between a cluster of nodules or granules) and nanopores (i.e., smaller pores of the spaces between individual modules or granules).

All of these results thus show that at relatively low contents of copper sulfate and sulfuric acid (Baths A and B), the ratio of the two chemicals in the plating bath slightly influences the morphology of the porous copper deposits. A larger contribution of the chemicals to the microstructure appears at higher chemical concentrations (Bath C). By increasing the current density from $0.05\text{A}/\text{cm}^2$ and $0.125\text{A}/\text{cm}^2$, the samples from all groups become more porous and less refined (Fig.

27 (A-2, B-2 and C-2). This is due to the increments of the deposition rate of copper atoms and generation and coalescence rates of hydrogen bubbles in the vicinity of the cathode at the high applied current. However, it should be mentioned pore shapes are not rounded, but rather it appears as highly rough surface with peaks and valleys: in the case, the porosity might not solely produced by hydrogen. However it should be mentioned pore shapes are not rounded, but rather it appears as highly rough surface with peaks and valleys: in this case, the porosity might not solely produced by hydrogen bubble generation, but also due to the electro-crystallization effect in the high current regime whereby preferential deposition occurred at the high current density area (electro-burning effect). Subsequently, the measured surface roughness of the samples of all groups increased when processed at a high current density, with the sample from group C experiencing the largest change in this regard.

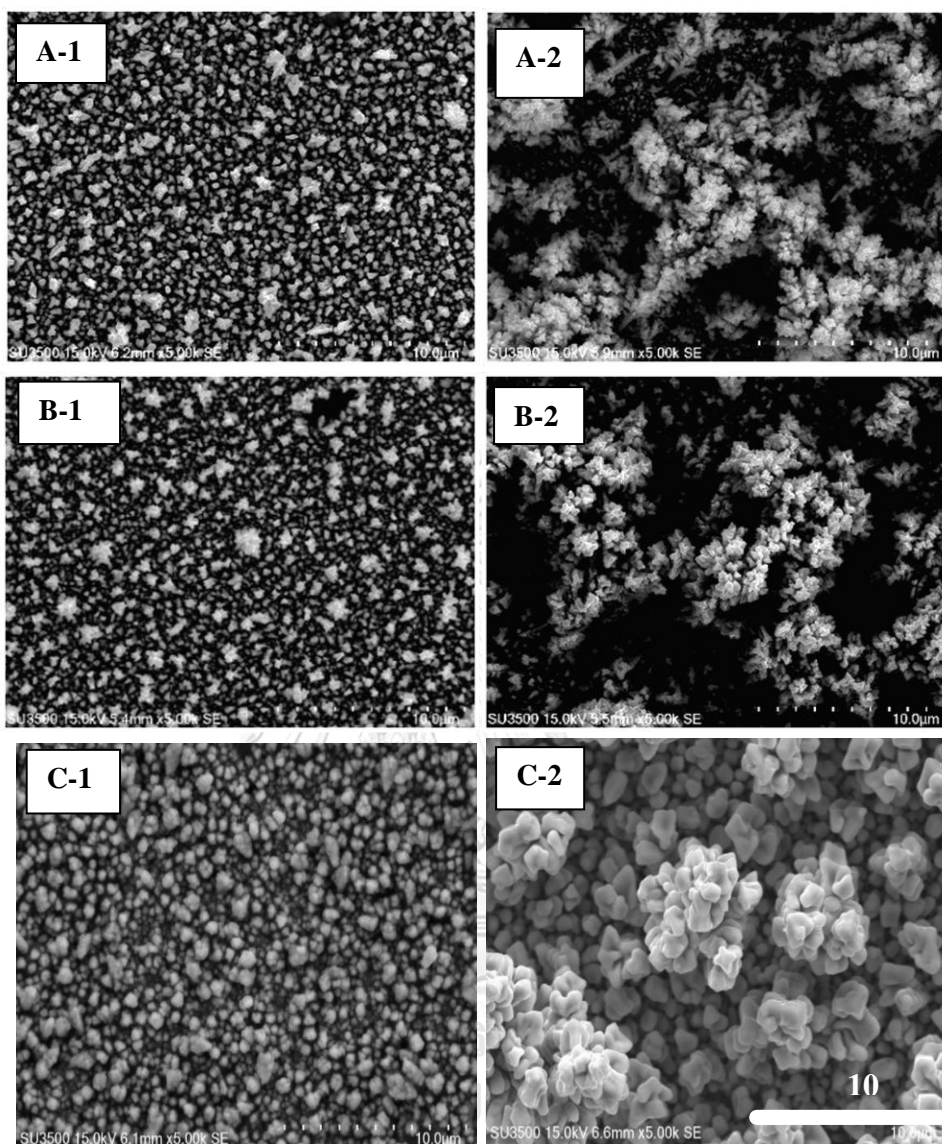


Figure 27 SEM micrographs showing the surface morphology of the porous copper samples from the 6 groups: A-1, A-2, B-1, B-2, C-1 and C-2

4.1.2 Wetting behavior

Fig. 28 presents the wetting angles of the samples in groups A, B, and C in the as-deposited state and after exposure to air. After deposition, all groups of samples exhibit Wenzel state, hydrophilic behavior, with advancing contact angles below approximately 20° . This was followed by rapid penetration of the droplet in droplets in the grooves within 5 sec. The as-deposited A-1, B-1, and C-2 are specifically superhydrophilic (fully-wet) with contact angles below 10° , whereas sample C-1 shows relatively high contact angles compared to the other groups. Compared to the typical static contact angle of a monolithic copper surface of 12° reported in the literature [200], the porous structures of electrodeposited copper can either promote or impede wettability, depending on the detailed structure of the deposits and in turn on the electrodeposition parameters. Interestingly, after storage in air for 4 weeks, all samples became hydrophobic, with contact angles above 130° and low hysteresis contact angle, as shown in Fig. 28, in parallel with a prior observation made to copper foams produced by different methods [201]. Samples A-2 and C-2 in particular show relatively high contact angles, close to 150° . Combined with the observed low hysteresis and low sliding contact angles, the state of superhydrophobicity, Cassie-Baxter wetting behavior, is confirmed for these sample groups.

Within the 4 weeks storing period, the wetting behavior of all samples generally progressed to various different states over time [202], changing from the Wenzel regime with full filling of water droplet in the surface's pores to the state where advancing angles were increased above 5° on average after a few days. Following the second week of air exposure, increments of both advancing and receding contact

angles, and hence pinning behavior, were observed. This may be considered as a hydrophilic transition state of the droplet, owing to a partial formation of liquid-vapor interphase. Subsequently, a hydrophobic transition state with higher advancing and receding angles of approximately 120° and 110° , respectively, appeared by the third week of the tests. Such state with less sticky behavior was soon overcome by the dewetting behavior of the Cassie-Baxter state by end of the tests.

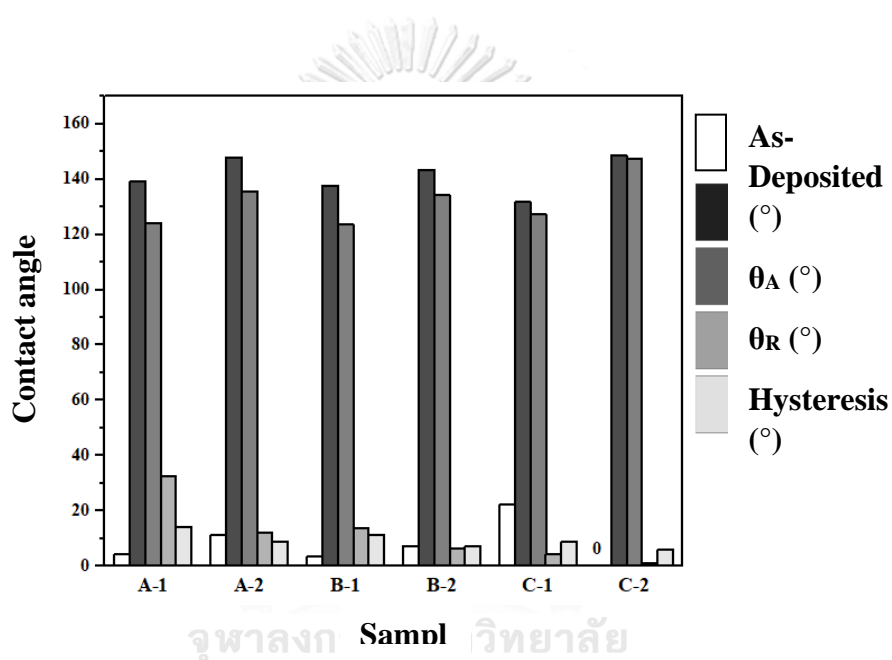


Figure 28 Advancing (θ_A), receding (θ_R), hysteresis, and sliding contact angles (θ_s) of the samples from 6 groups after 4 weeks of air exposure, in comparison with the contact angles of the samples measured following electrodeposition

The incremental shifts of wetting angles over the storage time in air could be attributed to various factors, including the formation of oxides on the copper surfaces owing to the chemical reaction of copper and oxygen [203, 204]. Cu_2O , in particular, is known to exhibit hydrophobic behavior. There were incremental levels of oxygen with carbon contents on the sample surfaces, as presented in **Table 10** for C-2 stored in different conditions. Some limited studies have also reported the possible effect of

volatile hydrocarbon contamination on the wettability reduction of copper surfaces exposed to air [205, 206]. Such an influence is, however, not clearly observed in this part. While there is a possibility of having contamination on samples surface right after cleaning and drying process, however, the degree of contamination probably not as significant to alter contact angle measurement, as shown in Fig.28. It should also be mentioned here that SEM vacuum system using such as diffusion pumps can create a backflow oil vapor which then break up under the electron beam. This can lead to the deposition of carbon on the surface of the specimen [207]. The as-deposited C-2 sample had a relatively large amount of carbon (Table 10). This carbon adsorption is possibly due to two effects: (i) because of the high surface energy and hence hydrophilicity that facilitate its interaction with the environment; (ii) because of the large, porous surfaces that are more prone to attracting hydrocarbon contaminants. Additionally, it has been noted that the roughness of a surface can promote air trapping underneath water droplets and a physical barrier for water to spread [208, 209]. These factors in turn lead to the development of surface hydrophobicity. The possible modification of surface roughness, and correspondingly a profile of pore structure, over the air-exposure period (e.g., as evidenced from the measured surface roughness of sample C-2 from 3.88 to 2.95 mm) signifies that this factor may play a role.

The wetting angles of the samples from the different groups vary from approximately 130° to 150° could suggest that the formation and possible content of the oxides and/or the characteristics of air entrapment in these samples are distinct from one another. Indeed, when the results of wetting angles are plotted with the measured surface roughness of the deposits, a strong correlation of these two parameters is

observed (Fig. 29). This could imply that the increase in surface roughness of the porous copper deposits facilitates the formation of oxides and/or air entrapment that favor water repellency.

Table 10 Chemical composition of the C-2 samples after being stored in the different storage conditions for 4 weeks, as measured by EDS

Environmental Condition	Composition (at. %)			
	Cu	O	Cl	C
As-Deposited	41.18	0.92	-	57.9
Air-Exposure	55.16	3.9	-	40.94
DI-Water Immersion	39.45	35.46	-	25.09
Salt solution Immersion	40.15	27.49	3.14	29.75

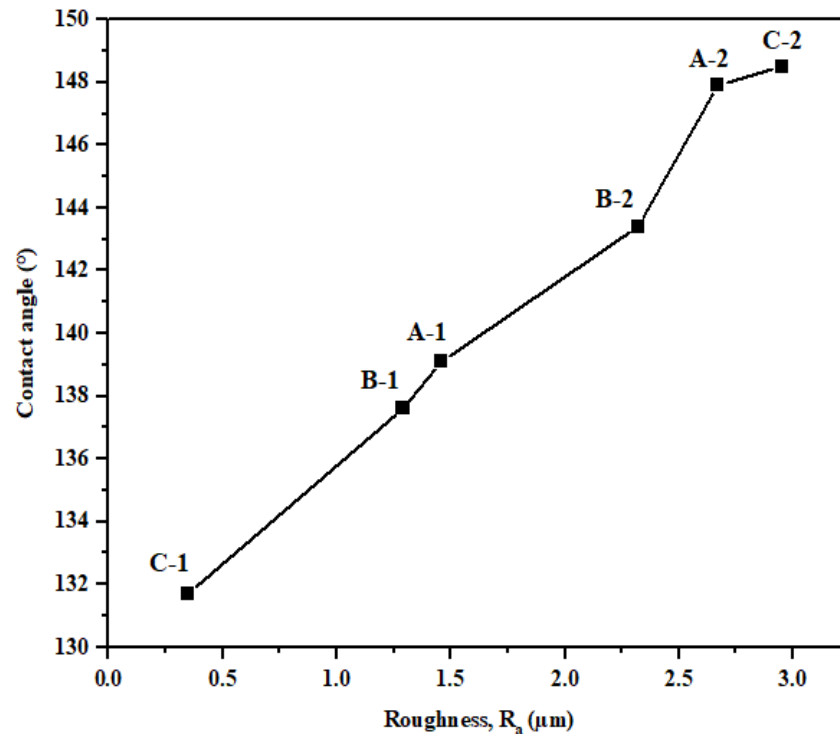


Figure 29 Measured contact angle of the porous copper samples with respect to their surface roughness (R_a) after 4 weeks of air-exposure.

4.1.3 The effects of storage conditions

The contact angles of the samples from groups C-1 and C-2 exposed to air, water, and saline solution were measured weekly, up to 4 weeks, as presented in Fig. 30. Overall, the C-1 and C-2 samples behave in a similar way: compared to those exposed to air, the wetting angles were decreased when the samples were stored in water and in saline solutions. Whereas the contact angle of the in-water sample increased gradually over time, that of the in-saline remained unchanged at zero degree. The

observed results can partially be reasoned by the microscopic changes of the copper surface, which may be characterized through surface roughness, as discussed in the previous section. Particularly, as illustrated by the micrographs in Fig. 31 and the surface roughness profiles in Fig. 32, the surface morphology and surface roughness of the C-2 samples stored under the different storage conditions are fairly distinct. The surface roughness of the samples exposed to water and to saline solution are much smaller than the as-deposited and in-air conditions. This could be due to the penetration of the liquid media into the porous structure, resulting in a reduction in hierarchical arrays of pores, enlargement of the solid contact area fraction, and smoothing of the surface profile. Furthermore, the chemical reactions between copper and water/salt would lead to the formation of copper oxide and copper chloride, which not only affect the surface morphology but also intrinsically influence the surface chemistry contribution that promotes a relatively high energy state of the surface and thus decreases the wetting contact angle compared to the copper surface exposed to the in-air condition. Additionally, the liquid medium may also contribute to the inhibition of hydrophobic surface oxide formation. Similar observation and correlation of the changes of surface roughness and wetting behavior of copper have been reported in some prior studies where copper particles were immersed to saline solutions, with subsequent development of insoluble copper chloride and dissolution of Cu_2O on the metal surface [210-213]

Finally, it is worth noting that a separate experiment was performed whereby the samples from C-2 group that had been stored individually in water and in saline solution were subsequently stored in air for another 4 weeks. The wetting angles of the samples were found to increase significantly to the superhydrophobic level ($\theta_A >$

150°, $\theta_s < 5^\circ$), a true Cassie-Baxter regime. This observation implies that the surface chemistry, which determines the wetting characteristic, can readily change from one storage condition to another, despite the transformation of the surface characteristics from the pre-exposure conditions in this case



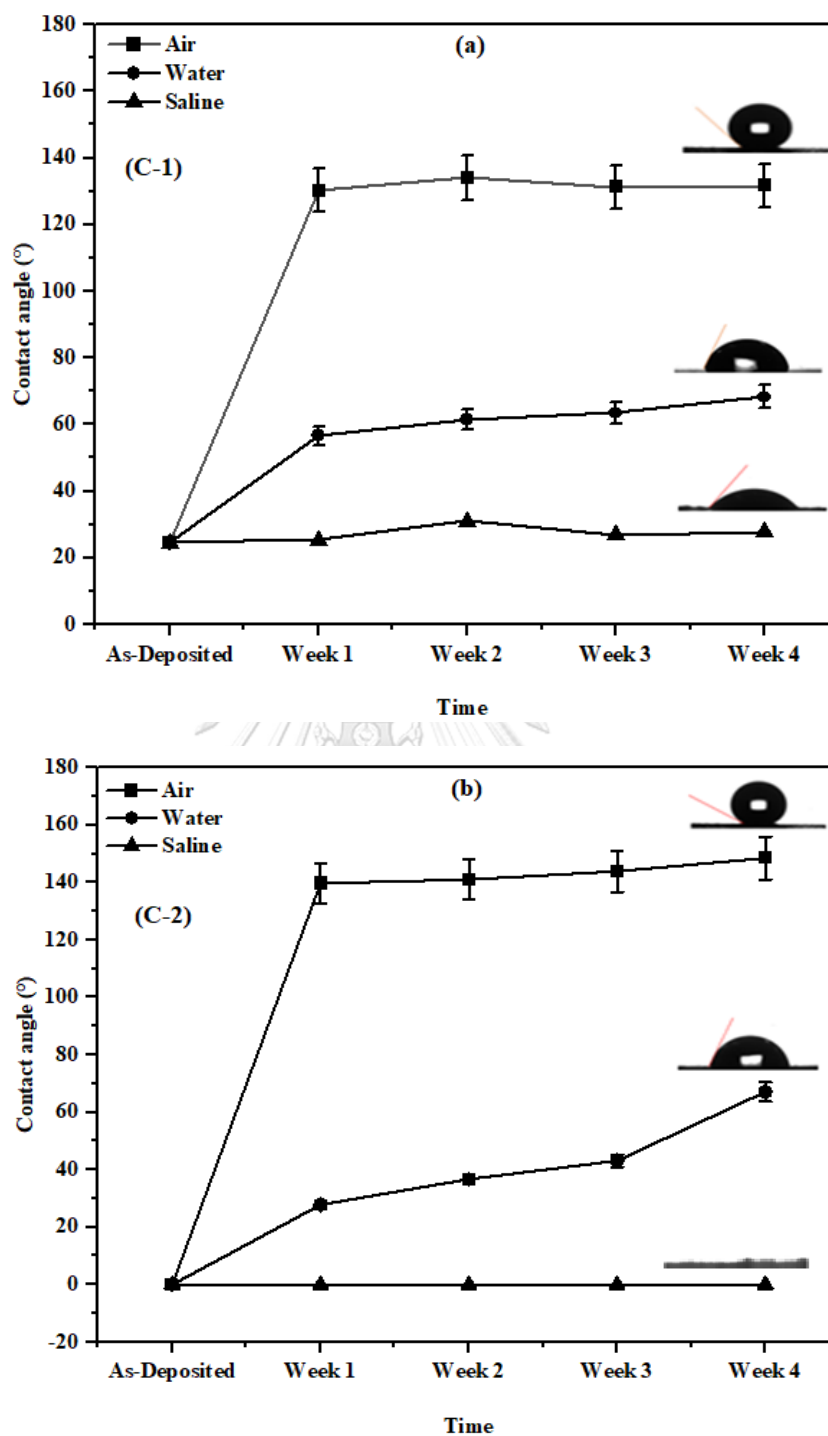


Figure 30 Weekly measurements of contact angles of C-1 (a) and C-2 (b) samples exposed to different storage conditions: air, DI water, saline solution

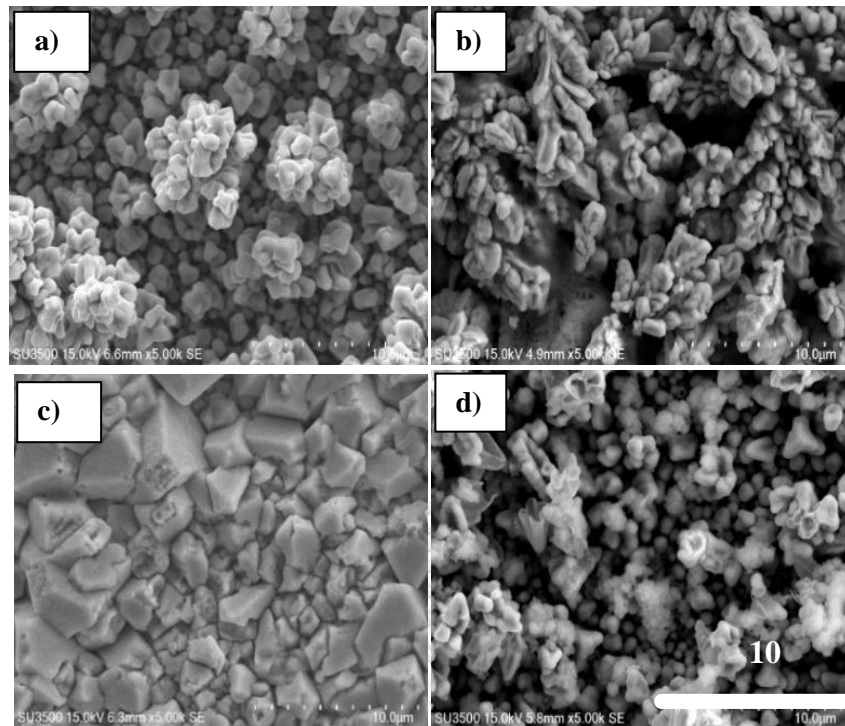


Figure 31 SEM micrographs of the C-2 samples under 4-week storage tests: a) as-deposited and after exposure to b) air, c) DI water, and d) saline solution

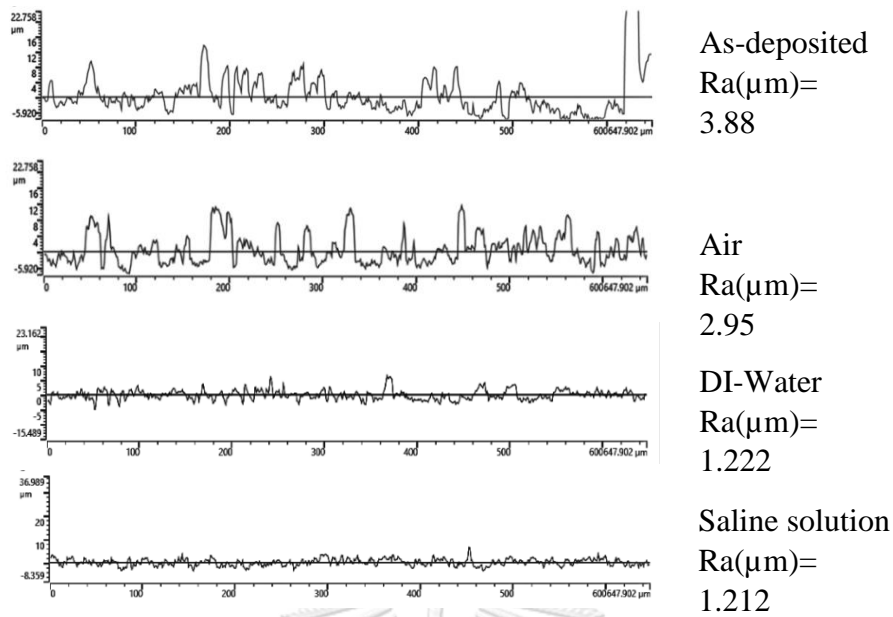
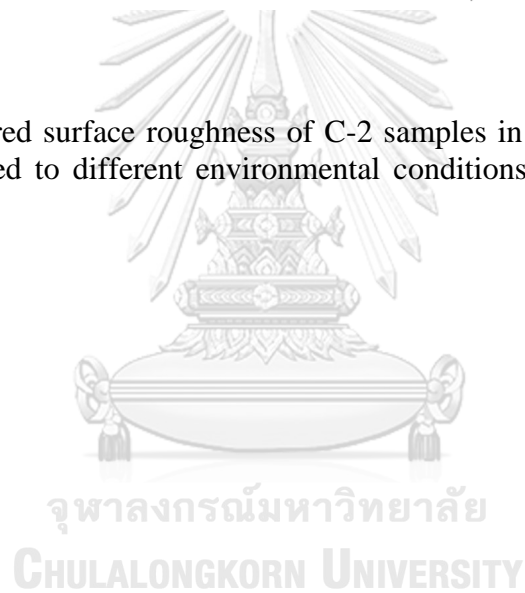


Figure 32 Measured surface roughness of C-2 samples in the as-deposited state and after being exposed to different environmental conditions under investigation for 4 weeks



4.1.4 Porosity control of copper surfaces

Several factors can influence the formation of porosity and pore characteristics of the electrodeposited copper surfaces. These include surface cleaning protocol, substrate roughness and characteristics, electrolyte composition and circulation, uses of additives, size of anodes with respect to cathodes, and distance between the electrodes.

In this part of the investigative work, three key porosity control parameters were of focus, including:

- 1) Current density,
- 2) Concentration of Cu ions from CuSO_4
- 3) Concentration of sulfuric acid H_2SO_4

These three important parameters must be examined in parallel in order to obtain a systematic control to achieve the target porosity. In the case of samples A-1 and A-2, the morphologies of these two samples showed less variation in porosity from 38.93 % to 40.55 %. **Fig 33.** This variation happened by just increasing of the current density from 0.05 to 0.125 A/cm^2 . On another hand for samples B-1 and B-2 with same copper sulfate concentration same like samples A-1 and A-2, there is a substantial difference in porosity around 10 % between B-1 and B-2 by only increasing the concentration of the sulfuric acid from 0.125 (group A) to 0.25 M (group B). This exhibits the influence of sulfuric acid concentration on obtaining different porosity.

The influential effect of copper ions and sulfuric acid concentration with varied current densities was clearly evident in the case of samples C-1 and C-2. In the case of C-1, ions transport is insufficient due to the low current density 0.05 A/cm^2 and high concentration 0.4 M . This was resulting in a highly porosity around 50.5% . On the other hand for C-2 with higher current density 0.125 A/cm^2 , the porosity is less 42.68% . It can be concluded here, in order to obtain superhydrophobic surface with contact angle near to 150 degree, the porosity should be in the range between (40 - 43%) as for samples A-2 and C-2.

However, for more accurate control, the porosity must be considered with roughness characterization. It is apparent from **Fig 34**, samples A-2, C-2, showed a relatively increase in porosity and higher degree of roughness compared with other samples. However, for C-1 in particular, showed highest porosity and the lowest roughness degree. It can be concluded here specifically for samples C-1 and C-2 that current density plays the main role in controlling the percentage of the porosity and the degree of roughness. Therefore, the current density will likely need to be adjusted, as indirect way, to eventually obtain specific contact angle, as previously shown in Fig. 29.

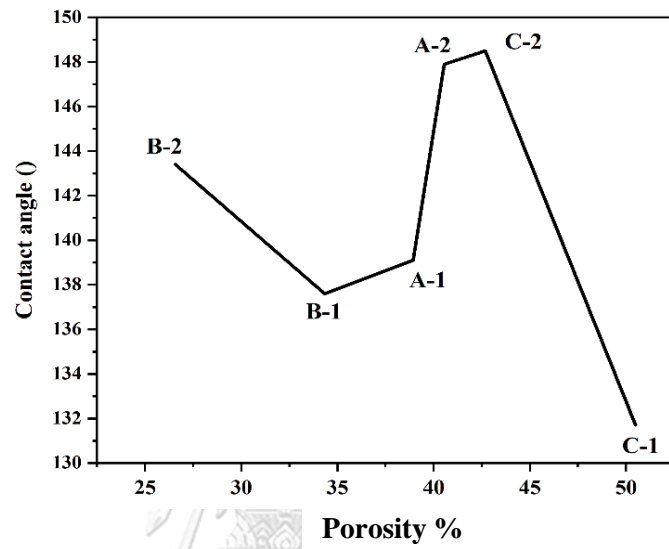


Figure 33 Contact angle measurements and porosity of all samples

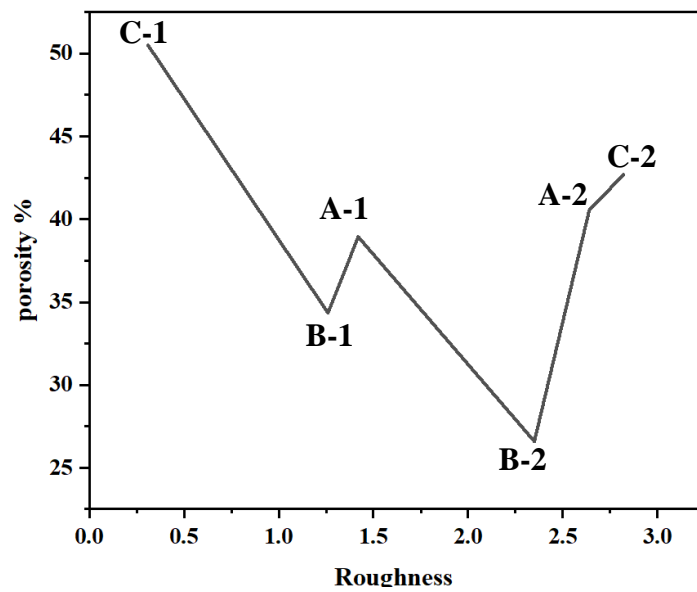


Figure 34 Roughness and porosity measurements of all samples

Part 2 Tailoring the wettability of copper surfaces by dropping of graphene solutions

4.2.1 A comparison of the Raman spectrum of graphene

4.2.1.1 Raman spectrum of graphene powder

In this work, the powder samples of graphene and graphene nanoplatelets were characterized by Raman spectroscopy and compared to references. The shape of the Raman spectra of the graphene and graphene nanoplatelets showed a similar low-intensity 2D band and a high-G band. **Fig.35** shows Raman spectra of a) graphene powder, b) graphene nanoplatelets, c) graphene powder from a reference [214]. The high intensity of the D-band of graphene nanoplatelets is indicative of an increasing number of graphene layers, which is also true for graphene nanosheets containing few graphene layers [215]. In comparison, the graphene powder used in this work showed a low intensity of D-band, noted in the reference. [214] with high intensity of G-band and low band of D and 2D.

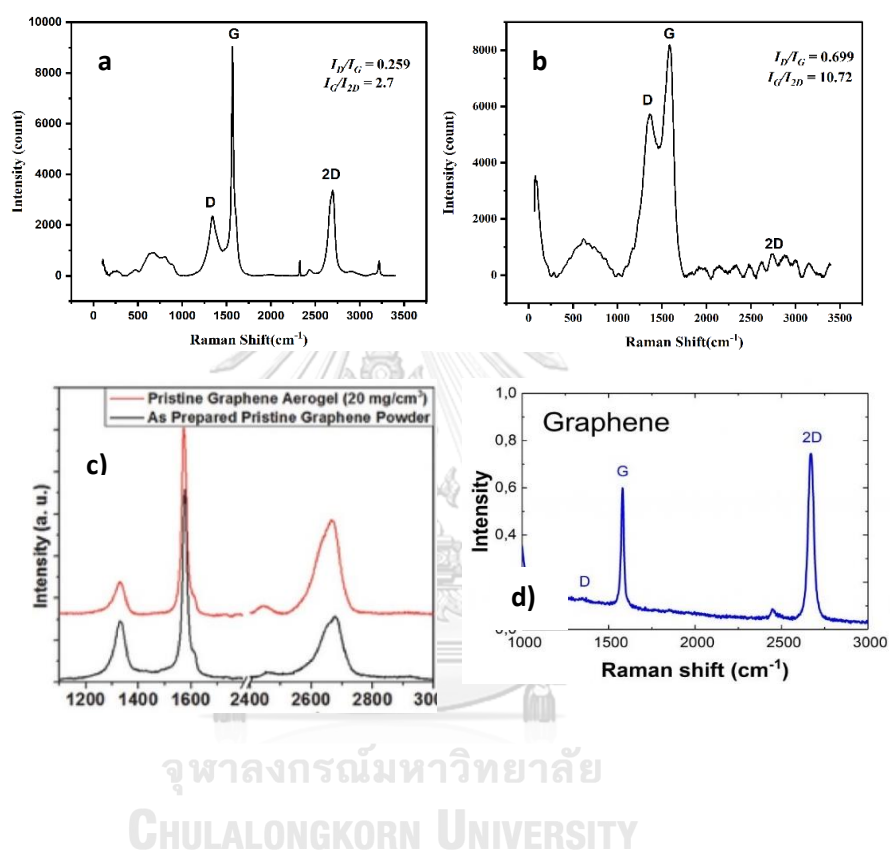


Figure 35 A comparison between a) graphene powder, b) graphene nanoplatelets powder, and c) from a reference [214] d) showed similar Raman spectra from Raman for life (ramanlife.com)

4.2.1.2 Raman spectra of graphene layers on metals surfaces

A) Flat surface

In general, 2D/G ratio is used for indication the number of graph layers. Therefore, in case of dispersed graphene of the samples C-Sol1 and C-Sol1' in **Fig 36**, the 2D/G ratio around (0.31) and (0.37), respectively. This ratios can be considered as multilayer graphene according to the references [216, 217]. The presence of graphene layers is also consistent with the following TEM observations in the next **section 4.2.3**

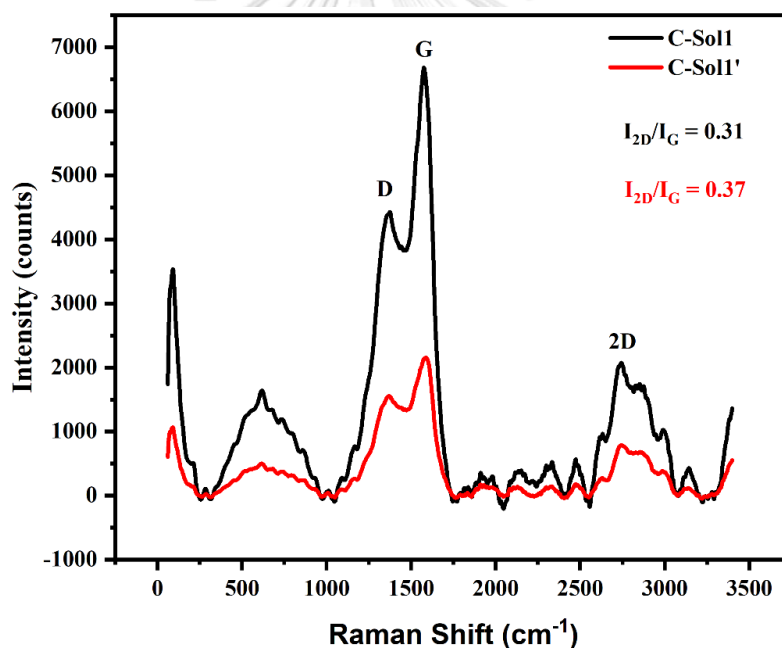


Figure 36 spectra of graphene of samples C-Sol1 and C-Sol1

Compared to other references, it is known that an existing fingerprint for identical Raman spectra of graphene could be used to unambiguously distinguish between defect-free single-layer graphene and defect-free graphite. The Raman spectrum

shows a high intensity peak at 2D around 2700 cm^{-1} and a low on G at 1582 cm^{-1} for graphene and vice versa for graphite in **Fig 37 a)**. It should be noted here that with more than 5 layers, the Raman spectrum is almost indistinguishable from that of the graphite mass. In addition, there are also some characteristics to distinguish a single-layer, two-layer, three-layer, single-layer FLG or even multiple layers of graphene depending on some factors. For example, the shapes of the 2D peak at 2700 cm^{-1} as shown in **Fig 37. b)** [218].

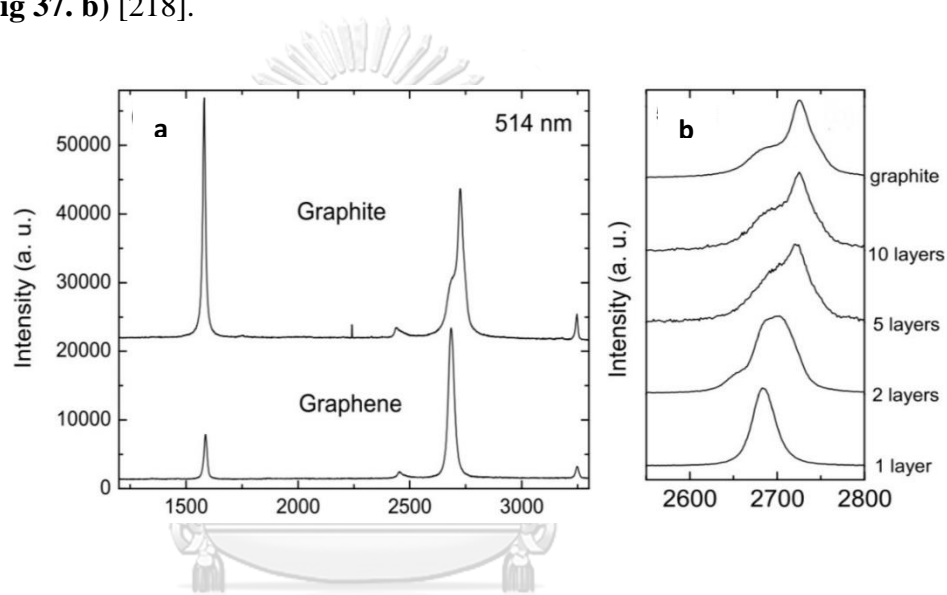


Figure 37 shows a) the ideal Raman spectra between graphene and graphite. b) different shape of spectra around 2700 cm^{-1} [218]

The freely suspended graphene shows a high peak at 2D and a low peak at G as ideal spectra for graphene, while the opposite spectra show peaks from graphene on supported metal (low peak at 2D and G) and smooth and a displacement change of 7 cm^{-1} between suspended and supported graphene sheets in **Fig. 38** [219]. It is noted that the decrease in 2D intensity occurs by increasing the number of graphene layers.

Fig 39 [220]

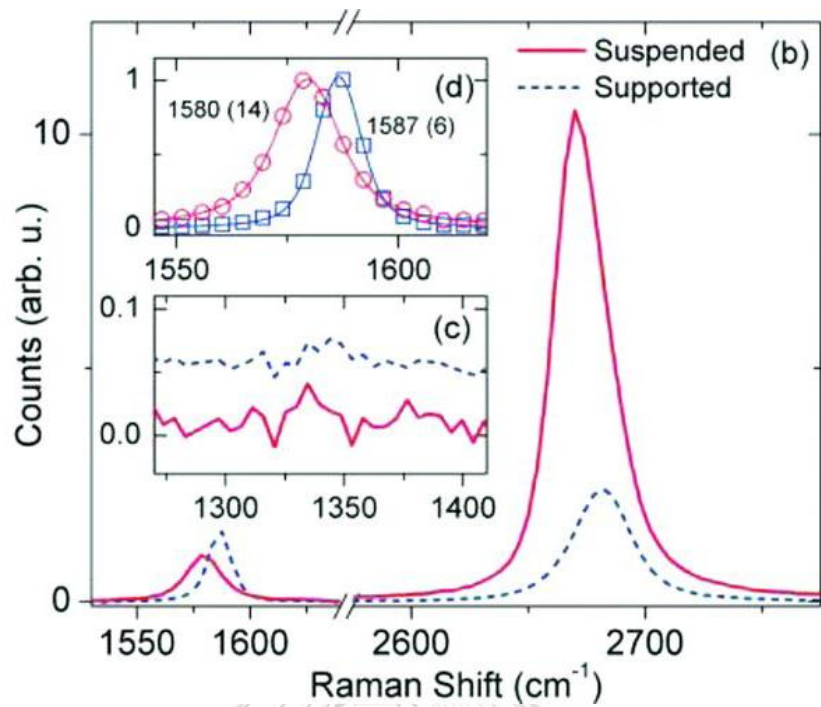


Figure 38 Raman spectra recorded on the single-layer graphene sample of (b), both for the suspended (red solid line) and supported regions (blue dashed line). (c) Raman spectra in the lower-frequency region (1,270–1,420 cm^{-1}) for the two regions of the sample. (d) Detailed comparison of normalized spectra for the G mode [219].

Besides, the Raman spectra can also be varied depending on the supported materials.

Fig.40 shows graphene growing on various metals such as copper and cobalt substrates [221].

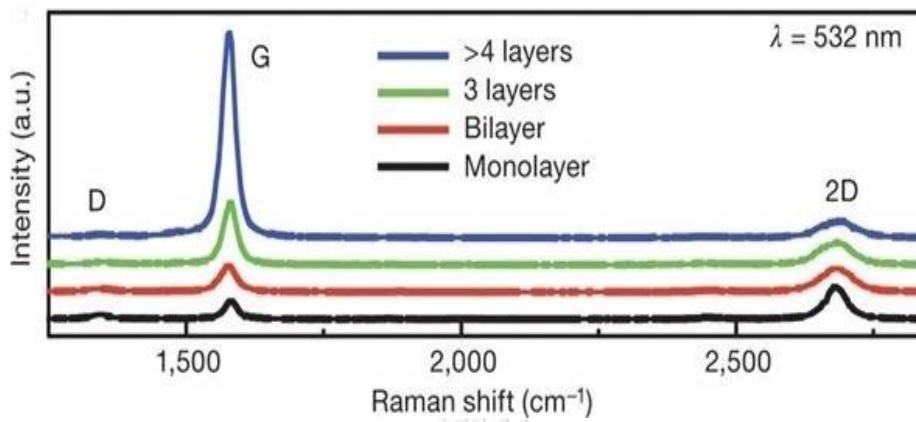


Figure 39 The Raman spectra of graphene as monolayer, bilayer, 3 layers and more than 4 layers [222]

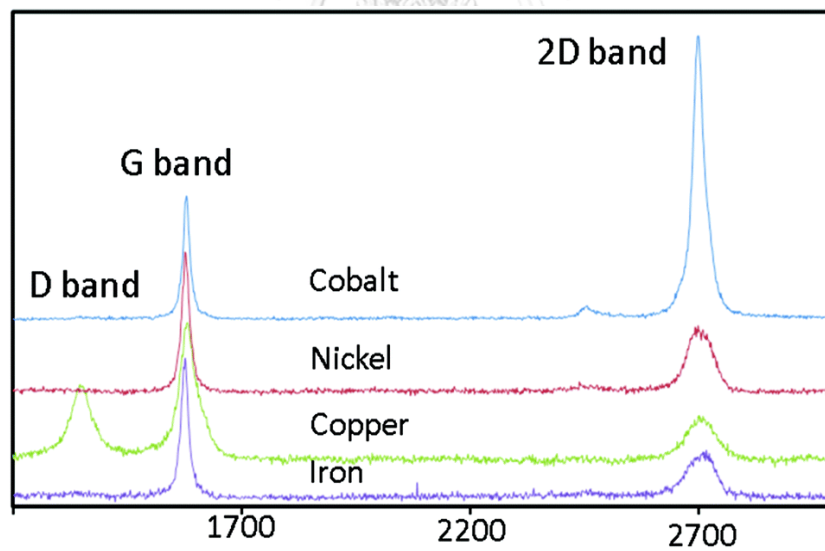


Figure 40 Different Raman spectra of graphene on various metals [221]

B) Porous surfaces

In case of electrodeposited porous samples C*-Sol1, C*-Sol1' in **Fig 41**, the presence of graphene is more clear noticed for samples C*-Sol1 with peaks at 2D, G, and D. With noticeable distinguish air contamination peaks are observed in sample C*-Sol1'. Furthermore, in an example of graphene on porous copper from a reference [223] the outer surface of the sample can show features similar to high quality graphene grown on copper as shown in **Fig.42**. Whereas the cross section of the porous structure shows a significantly higher intensity for the D band and a lower 2D/G ratio [223]. This may also give an indication of the Raman spectra of graphene on porous copper surface obtained from Sample **C* Sol1** as shown in **Fig. 41**.

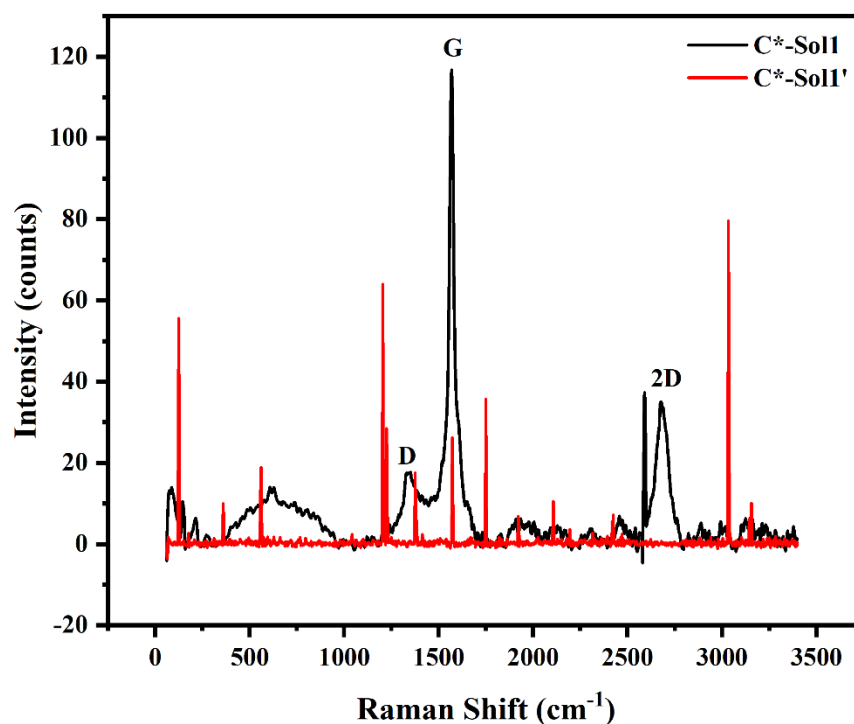


Figure 41 Raman spectra of two samples C*-Sol1 and C*-Sol1'

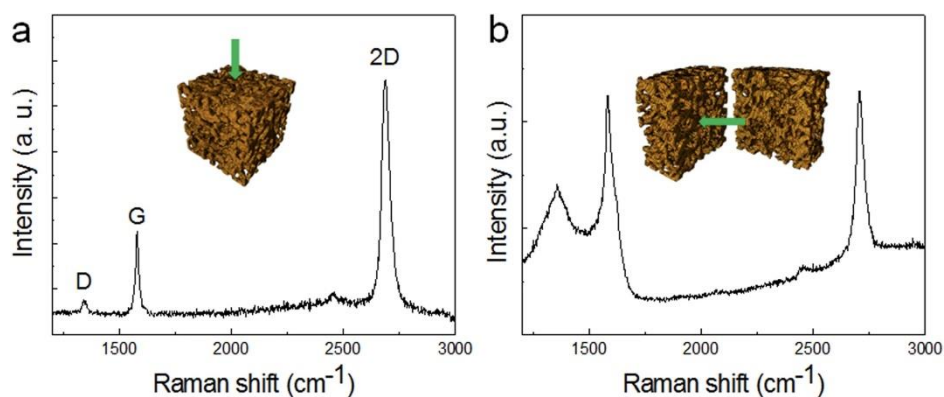


Figure 42 Raman spectra of graphitic layers grown on the porous structure. a) The outer surface and b) the cross-section after cutting [223]

4.2.2 TEM images for graphene solutions Sol1 and Sol2

TEM observation was performed to examine the morphology of dispersed graphene from Sol-1, and the result was compared to that of graphene without using the surfactant Sol-2. **Fig.43** shows the TEM images of the two dispersed graphene solutions. The light gray areas show isolated graphene sheets, since graphene sheets are highly transparent to electron beams [224]. In contrast, the dark areas of both images can be taken as an indication that the electron beam barely penetrates through the twisted, crumpled layers of the graphene sheets, especially at the edges. From the TEM images it can be seen that the use of surfactant in solution Sol-1 (**Fig. 43.a**) provides a relatively higher concentration of graphene sheets compared to Sol-2 in (**Fig. 43 b**). Further, this work is consistent with other investigative works such as the work of **Pu et al** [225]. They studied the effect of using different surfactants on dispersed graphene solutions using TEM. Comparing their results in **Fig. 44** gives a similar result of graphene sheets, which are expected around 4-6 layers of graphene

sheets as shown in Fig. 44. In particular, The TEM image c) is in case of using SDS, which highly consistent with this work. To better distinguish the contrast between graphite and graphene from TEM images from another investigation work, the graphite showed dark areas, **Fig. 45 a)**, compared to grey, exfoliated graphene in **Fig. 45 b)** [226]

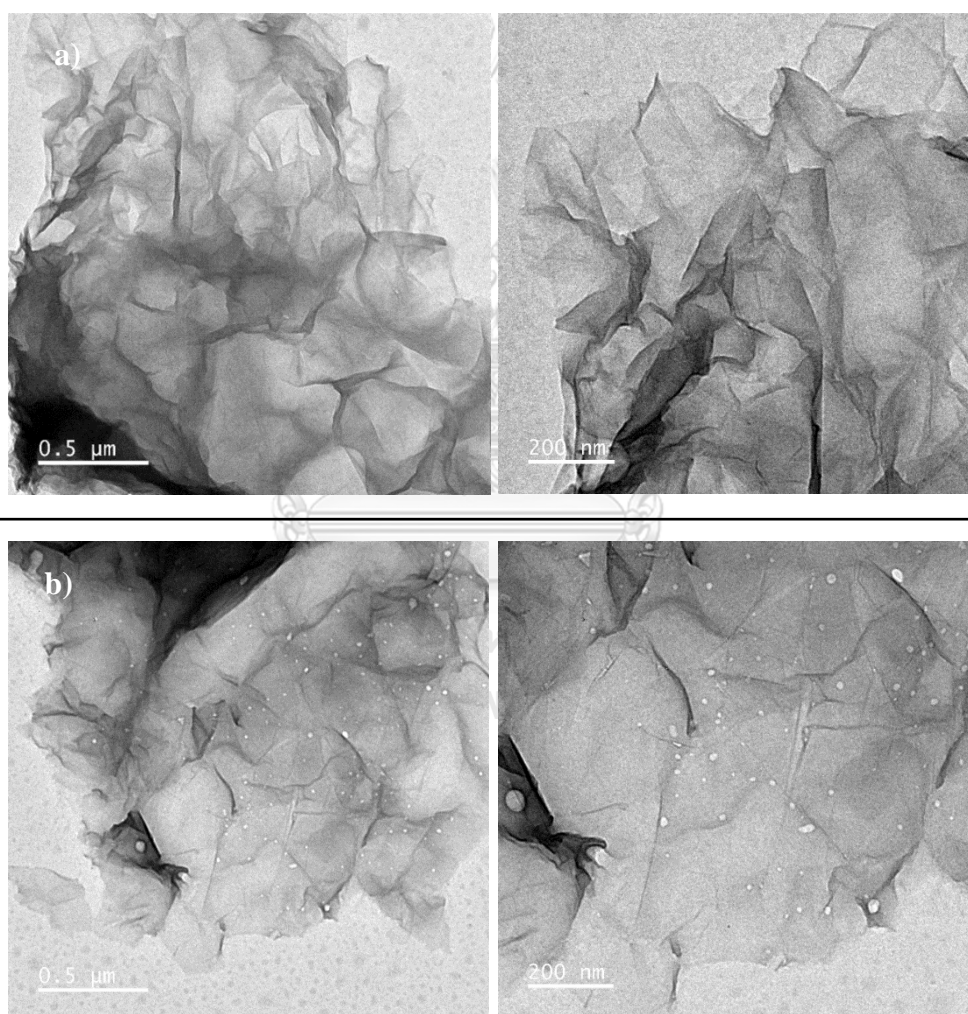


Figure 43 TEM images of graphene dispersed solutions a) Sol1, b) Sol2

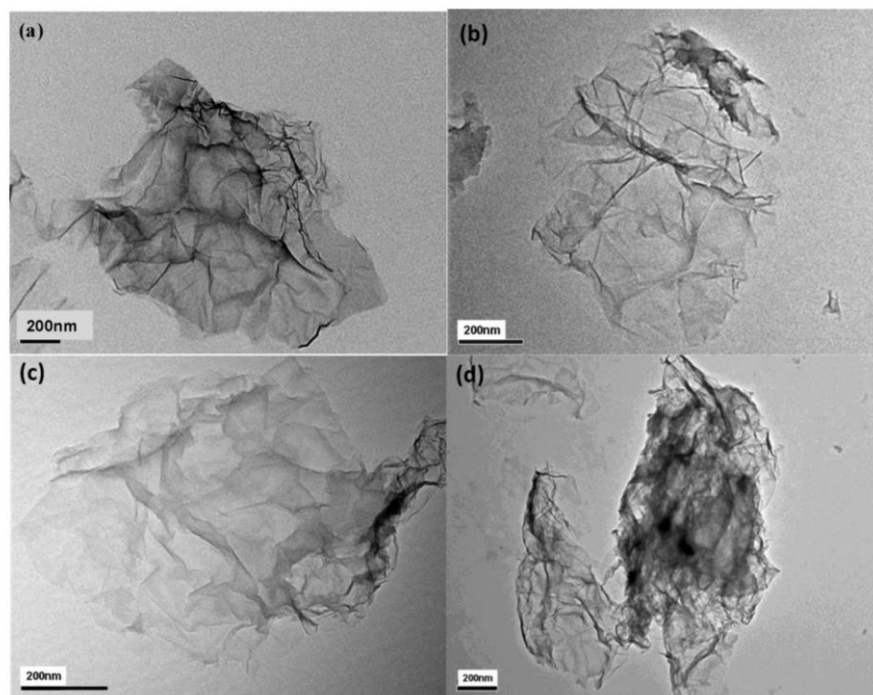


Figure 44 TEM images of the graphene dispersed with different surfactants: (a) 300 ppm CTAB; 300 ppm CO890; (C) 200 ppm SDS and (d) 300 ppm H14N [225]

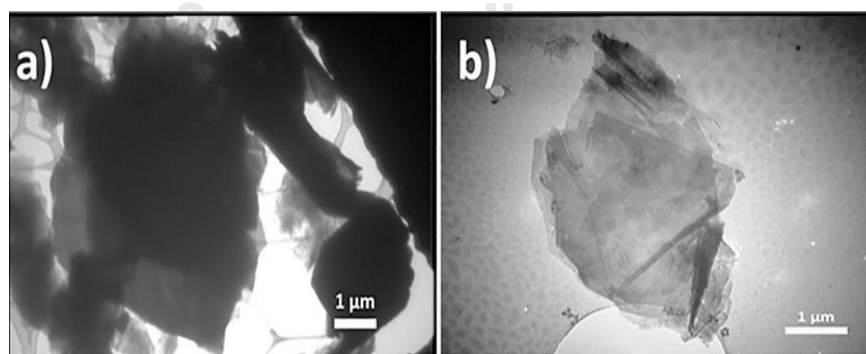


Figure 45 a) the initial graphite particle b) exfoliated multilayer graphene [226]

4.2.3 Overall wettability results

A variety of contact angle measurements were recorded for both geometric copper surfaces as flat and electrodeposited porous layers. **Fig.46** From zero contact angle (superhydrophilic) for sample (C*-Sol1) to about 152.45 (superhydrophobic) for sample (C*-Sol1'). For flat surface samples, the lowest advancing contact angle was for Sample C- Sol1 (54.86°) and the highest for Sample C-Sol1' (123.56°) compared to Sample C (72.42°) (Sample C without using a droplet of graphene solution on the surface). The flat surfaced samples also showed lower susceptibility to air pollution compared to the porous samples which will be discussed in the next sections. A slightly deviation in the average of both of advancing and receding contact angles for C-Sol2 (83.84°, 74.23°) and for C-Sol2' (87.34°, 73.93°) respectively was recorded. Furthermore, non-uniform distribution of graphene from solution Sol2 was observed during evaporation process result in accumulation dispersed graphene in some areas on samples C-Sol2 and C-Sol2' in **Fig.47**.

However, for the electrodeposited porous samples (C*-Sol1, C*-Sol1', C*Sol2, C*-Sol2'), a zero contact angle was found for sample C*-Sol1 because of the use of surfactants. **Fig 48**. Whereas, for sample C* Sol1', in particular, the air pollution effect likely resulted in a maximum contact angle of about 152.45 degrees. Additionally, in case of C*-Sol2', various advancing contact angle measurement (between 101.65° to 117.82°) from different areas were tested. In this sample (C*-Sol2'), accumulation of graphene, in some pores (dark spotted areas), can lead to wrinkled graphene sheets.

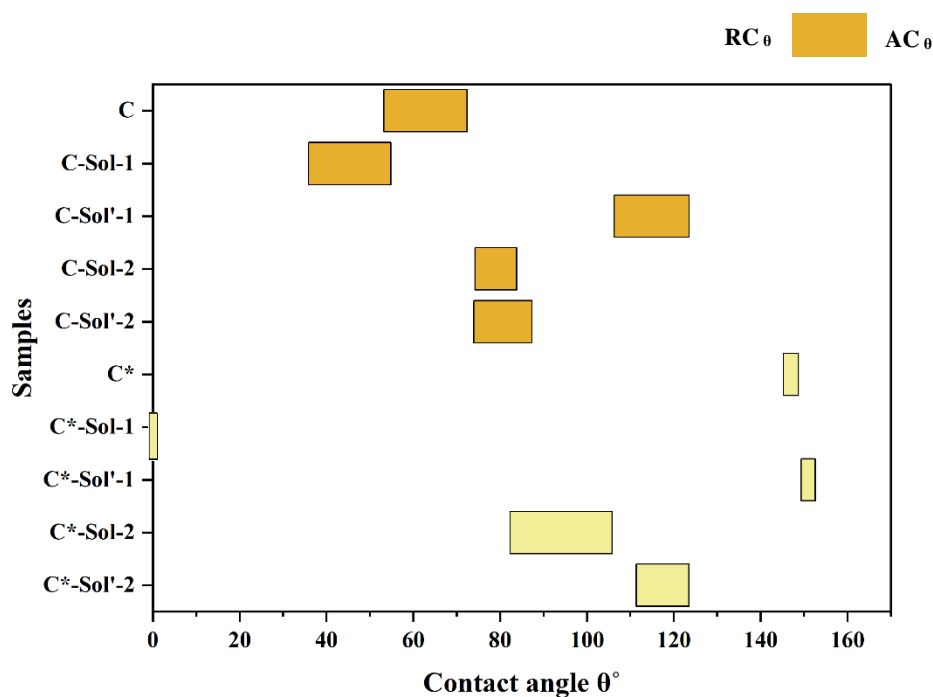


Figure 46 Advancing AC_{θ} and receding RC_{θ} contact angles measurement for (C), (C-Sol1), (C-Sol1'), (C-Sol2), (C-Sol2'), (C*), (C*-Sol1), (C*-Sol1'), (C*-Sol2), and (C*-Sol2')

Moreover, graphene with good dispersion, once covered on the copper surface, promotes surface hydrophilicity (C-Sol1 & C*-Sol1). This effect is more pronounced in the case of porous copper (C*) than in the case of monolithic copper (C). The opposite effect occurs when using a low (diluted) level of graphene (C-Sol1' & C*-Sol1'). These surfaces all show hydrophobic/superhydrophobic with no graphene dispersion (Sol2 and Sol2'). All offer moderate wetting angles (80–100 degrees). This is true for both C and C*. In general, the physical and chemical effects are the main influencing factors in providing this wide range of contact angles. Also considered is the effect of the SDS surfactant in demonstrating excellent dispersing of

graphene and its reduced effect through dilution. In the next sections 4.2.5 and 4.2.6 explain the possible physical and chemical explanation of these observations

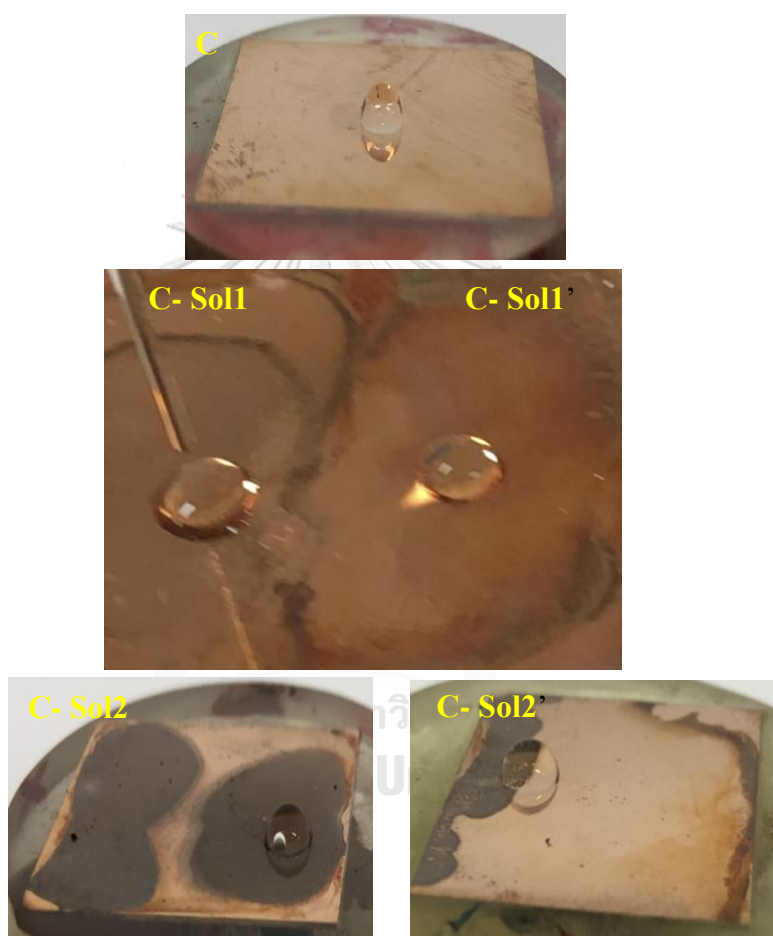


Figure 47 Photos of water droplets on samples (C), (C-Sol1), (C-Sol1'), (C-Sol2) and (C-Sol2').

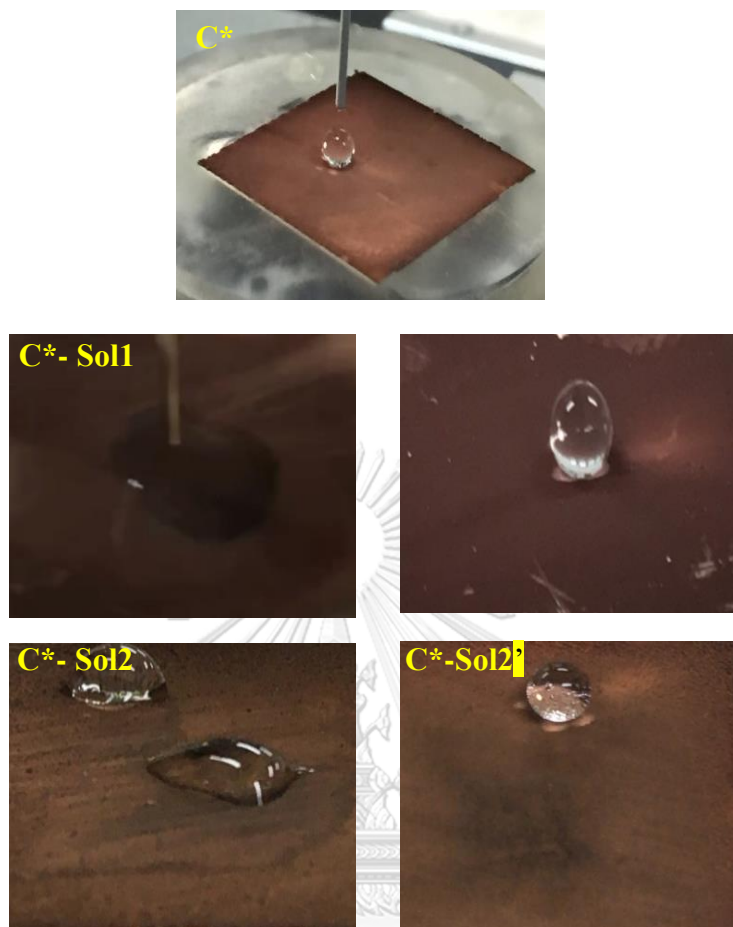


Figure 48 Photos of water droplet on samples (C*), (C*-Sol1), (C*-Sol1'), (C*-Sol2) and (C*-Sol2')

4.2.4 Physical effect on wetting behavior

4.2.4.1 Flat copper surfaces

For flat copper surfaces, graphene drop deposition partially altered the intrinsic wetting behaviour of bare copper substrate samples. The lowest advancing contact angle was for Sample C- Sol1 (54.86°) and the highest for Sample C-Sol1' (123.56°) compared to Sample C (72.42°) without using a graphene droplet on the surface. The presence of layered graphene on the flat surfaces for samples C-Sol1 and C-Sol1' (with SDS surfactant) was confirmed by Raman spectroscopy **Fig. 36** and TEM images in **Fig.43**. The difference in contact angles between C-Sol1 and C-Sol1' is significant and is probably estimated from the remarkable variation in intensity of the G, D and 2D bands between the two samples. This variation in intensities can lead to three important observations: (1) the intensity of the D and 2D defects correlates with the contact angle, and (2) an easily controllable graphene solution concentration can be used to tune the contact angles, and (3) re-dispersion the solution of Sol1 in Sol1' suggests that the contact angle measurement could predict from the Raman spectra of graphene layers on a flat copper surface and vice versa.

As noted before, a slight variation in the average of both the advancing and receding contact angles was found for C-Sol2 (83.84° , 74.23°) and for C-Sol2' (87.34° , 73.93°) respectively.

The hydrophilic behavior of samples C-Sol2 and C-Sol2' may be due to the lower availability of air pockets to create air entrapment on flat surfaces. In addition, the influence of airborne contamination on the change in the wetting behavior of some samples is discussed in next sections. From this, it can be concluded that for flat copper substrates, the deposited graphene solution partially affects the wetting behavior and the samples showed a hydrophilic behavior of less than 90° except for sample C-Sol1'. It was also clearly observed that the use of surfactant SDS in samples C-Sol1 and C-Sol1' offered a chance for stronger adsorption of graphene solutions.

4.2.4.2 Porous copper surfaces

In case of electrodeposited porous copper, graphene solution Sol1 may contribute to the disappearance of the hierarchical arrays of C*-Sol1 sample (right) in Fig 51 and produce only a micro porous copper surface. Therefore, less availability of air-trapping. The sample C*-Sol1 in Fig 51 (right) showed some dark areas where the graphene sheets settled with the homogenous distribution. This assumption has an important aspect for altering the wetting behaviour by varying the amount trapped air. In contrast, sample C*-Sol1' exhibit superhydrophobic behaviour (152.45°) after measuring for one month and nearly the same as C* sample (148.43°) In case of C*-Sol2 and C*-Sol2', the advancing and receding contact angle measurements for sample C*-Sol-2 were (105.8° , 82.35°) and for C*-Sol2 (139.52° , 111.35°) Fig 46. Although, the degree of advancing contact angle for C*-Sol2 implies hydrophobic behaviour more than 90° but water droplet showed sticky behaviour on the surface even by turning the sample upside down. This Indication of what is called "pinning

effect of contact line”. This phenomenon was mostly noticed on dark area where graphene sheets probably accumulated. Although, some researcher claimed that the wrinkled morphology can improve the hydrophobicity of graphene, but wrinkled graphene layers can result in pinning effect of contact line as water prefer to stay at the crest of wrinkles [227]

4.2.5 Chemical effect on wetting behavior

One of most important feature affecting the wetting behavior was the use of the anionic surfactant SDS with graphene. Even with air exposure, sample C*-Sol1 sustained its wetting behaviour as superhydrophilic. Taking into account the fact that surfactants are compounds that lower the interfacial tension - between two liquids, a liquid and a solid or a gas and a liquid. Additionally, SDS can prevent graphene layers from re-aggregating and elongate the graphene layers. This produced multiple layers of graphene to cover most of the sample surface area according to the consistency of the contact angle measurement on different areas of sample C*-Sol1. Moreover, the hydrophilic tail of SDS may point to the water molecules, which itself could be an additional clue to the superhydrophilicity of sample C*-Sol1. However, acting of SDS separately from graphene has a limited effect on the change in the wettability of copper. This became more evident when 0.2M SDS was dropped onto Sample C*. Superhydrophilic behavior was observed during the first week and the contact angle increased rapidly from zero As-deposited to about 147.45 at the end of one month. This observation indicated a limited effect of SDS apart from graphene on wettability porous copper sample C* and acts as a wetting agent for a short time. Although, it

was investigated elsewhere that SDS can effectively decrease the pore sizes of porous copper films as part of electrolyte solution [228] but it is more likely that deposited SDS on porous copper plays no part in preventing airborne contamination without graphene compared to the superhydrophilic behavior of C*-Sol1 (graphene with SDS). On other hand, sample C* with SDS only is more likely to be subjected to air contamination, resulting in an increase in contact angle from zero to about 147.45 degree as SDS solution does not protect the porous from airborne . This was investigated elsewhere that there is a possibility of SDS aggregation (without graphene) on a metal surface and concentrated in specific areas [229]

However, the superhydrophobic behavior of sample C*-Sol1' same as C*, is considered as indication that graphene sheets did not also cover all the entire electrodeposited copper surfaces. The SDS surfactant may also lose its surface activity according to the less dispersion of graphene from the solution Sol1'. It observed also that sample C*-Sol1' showed initially hydrophilic behavior after being fabricated but contact angles increased rapidly and continued overtime for four weeks until around 152.43 degree. The responsible of this wetting transitions was probably related to the high level of adsorption of organic matters such as C₂H₂ C₂H₄ C₃H₆ C₄H₆. The attendance of this hydrocarbon contamination confirmed by Raman spectra that showed high intense peaks. For example the peak around 3035 cm⁻¹ is supposedly to be phenyl on sample C*-Sol1' Fig.41. Moreover, Table 11 showed variable content of carbon on the surface of some sample of interest. In comparison with sample C*-Sol1, this air borne contamination was inhibited by using of Sol1 solution. The Raman spectra Fig. 41 of C*-Sol1 showed low intense peaks around 3000 cm⁻¹ and therefore gives an evidence of the superhydrophilic behavior of sample C*-Sol1.

It should be noted here, this probability of air contamination relied on a comparison from some reference [230-232] More details of the peaks in Fig.49 and Fig.50

Table 11 Chemical composition of the samples of interest C*-Sol1, C-Sol1 and C-Sol1' for 4 weeks, as measured by EDS

Samples	Composition (at. %)		
	Cu	O	C
C*-Sol1 fresh	41.10	5.70	53.20
C*-Sol1- 30 days	56.76	8.72	34.52
C-Sol1-30 days	54.56	4.15	41.30
C-Sol1'-30days	58.39	4.91	36.70

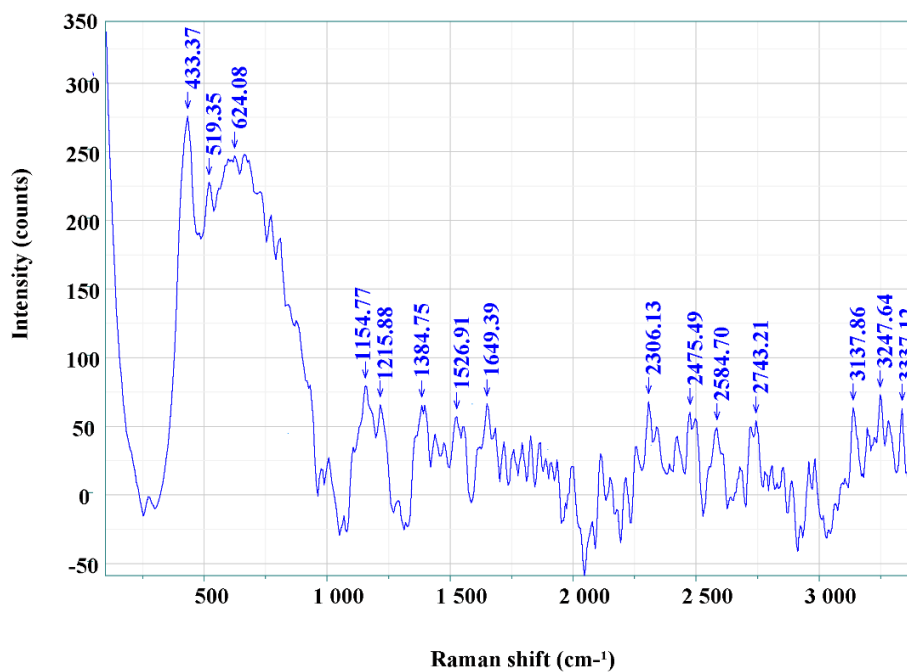


Figure 49 More details of the Raman spectra of sample C*-Sol1

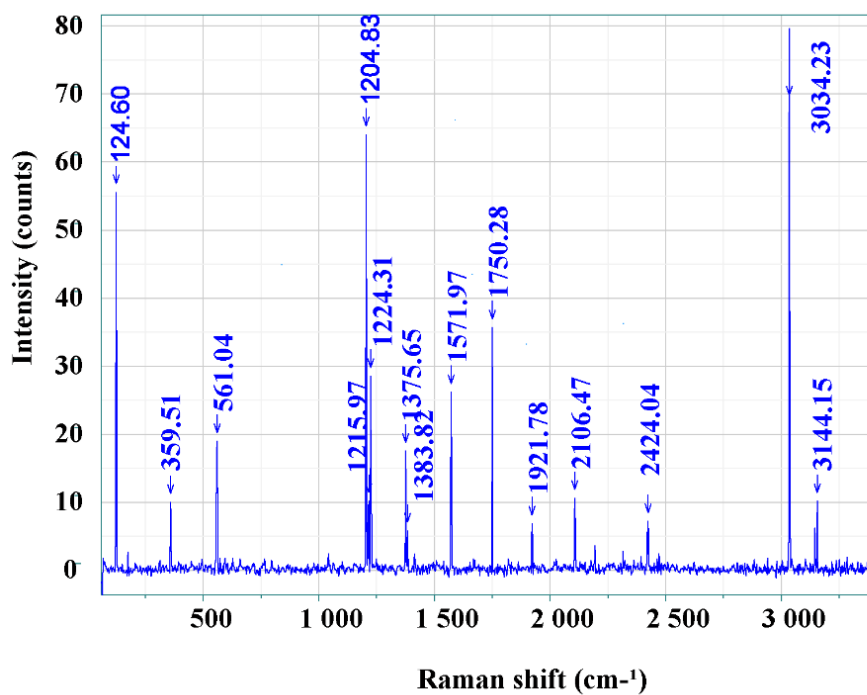


Figure 50 More details of the Raman spectra of sample C*-Sol2'

4.2.6 Further observation of the physical effect

The impact of different geometric porous structures of samples with different current densities C^* (0.125 A/cm^{-1}), and D^* and D^* -Sol1 (3 A/cm^{-1}) on the wettability was realized. Start by comparing different structures from the SEM images of the samples in **Fig 51** and **Fig 52**. The images showed a hierarchically dense exterior area on the deposited copper in sample C^* in **Fig 51** and large pores with depths of the channels in samples D^* and D^* -Sol1 in **Fig 52**. In Sample C^* , a new liquid-air interface (hydrophobic) may have been created between the droplet and the air beneath the water droplet. This interface may add an explanation of the superhydrophobic behavior of Sample C^* (a porous sample). In addition, sample of interest C^* -Sol1 (using SDS) showed superhydrophilic behavior. Interestingly, both samples D^* and D^* -Sol1 showed sustained superhydrophilic behavior without dropping graphene D^* and with graphene D^* -Sol1 **Fig.52**. This superhydrophilicity of both samples D^* and D^* -Sol1 is probably due to the large pore network. It was observed that a slight penetration of water droplets penetrates through the pores and further into the channels of the pores. This may attribute to a gravity-driven effect that can force water ingress into the pores, with a great chance of air escaping once the water intrusion was initiated. The droplet typically reached a plateau level after several seconds. When graphene was deposited in the sample D^* -Sol1, the contact angle was stable at 0° with a relatively faster water propagation speed of about 4 seconds compared to 7 seconds for sample D^* . This may be to the accumulation of graphene at the bottom of the pores, resulting on frictionless passage of water into the channels.

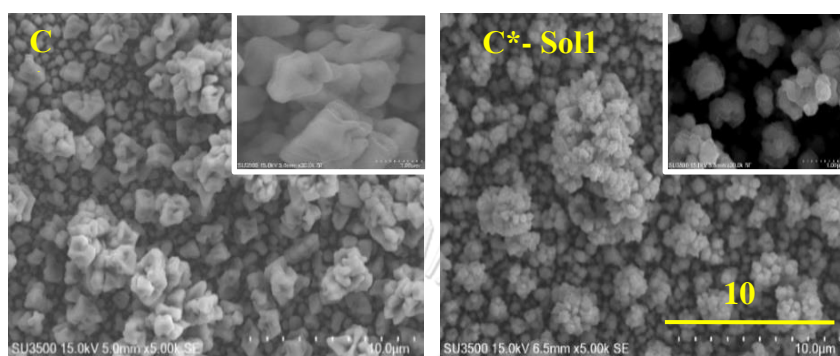


Figure 51 shown the porous copper without graphene C* (superhydrophobic) on left and the sample of interest C*-Sol1 (superhydrophilic) after 30 days of air exposure

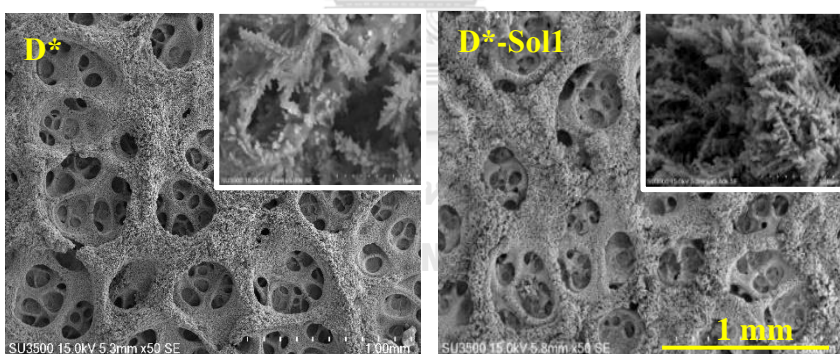


Figure 52 SEM micrographs showing the surface morphology of the 3D porous copper samples D* and D*-Sol1.

CHAPTER VI CONCLUSION

Part 1 Effects of plating and storage conditions on the wettability of electrodeposited porous copper surfaces

Porous copper samples with hierarchical arrays of interconnected micropores and nanopores were successfully developed with a variation process parameter. By increasing concentration of the copper electrolyte, copper granules' size became larger and more uniform in size. The increase of the applied current density led to micropore enlargement and some changes in copper granules' size. These physical characteristics reflect in the variations of contact angles in the hydrophilic regime that positively or negatively deviate from that of the monolithic copper surface. Following the air storing session, it was found that the examined porous copper samples became hydrophobic and their surface roughness directly related to the wetting angle, which may be owed to the relation of exposed surface area to oxidation and to the air trapping effect. In the DI water and saline solution storage conditions, on the other hand, the examined porous copper samples exhibited hydrophilic characteristics, most likely owing variations in surface morphology and roughness, and changes of surface chemistry. Overall, this study thus illustrates how electrodeposition parameters and storage conditions can largely and mutually influence the development of a large variation of wetting characteristics, from hydrophilic and hydrophobic, for copper surfaces. The ability to control the wetting behavior of the copper surfaces would be important and useful for many engineering applications and corrosion protection functions

Part 2 Tailoring the wettability of copper surfaces by dropping of graphene solutions

The use of graphene on substrates or electro-deposited copper surfaces showed high feasibility of wettability control and mainly depends on both geometric features and the dispersion of graphene solutions on the obtained samples. There exists a significant correlation between electrodeposited surfaces and graphene by utilization of graphene to obtain different contact angles measurements. Although wetting transparency has not been clearly observed in the case of few-layer graphene using a drop of graphene solutions, however, there is an opportunity to tune the wetting behavior on the obtained copper surfaces. A wide range of contact angle measurement was recorded by choosing different concentration of the graphene solutions. The highest contact angle for porous copper, C* and C*-Sol1', coated with low concentration of graphene solutions before subjected air exposure. A droplet of graphene solution with SDS surfactant on the epitaxial surface of porous copper showed sustainable superhydrophilic behavior during one month. This emphasizes that using an SDS surfactant is more applicable to provide good graphene dispersibility and control graphene wetting behavior. This work provides a simple way to understand the effect of parameters such as the concentration on altering the wetting behavior of graphene layer on copper. Characterization with Raman spectra provided a reasonable analysis of the possibility of air environment affecting the wetting transition on porous copper surfaces.

REFERENCES



จุฬาลงกรณ์มหาวิทยาลัย
CHULALONGKORN UNIVERSITY

1. Wang, H., et al., *Fabrication of superhydrophobic metallic surface on the electrical discharge machining basement*. Applied Surface Science, 2019. **478**: p. 110-118.
2. Jo, H., et al., *Nucleate boiling performance on nano/microstructures with different wetting surfaces*. Nanoscale research letters, 2012. **7**(1): p. 1-9.
3. Nishikawa, N., et al., *Theoretical explanation of the photoswitchable superhydrophobicity of diarylethene microcrystalline surfaces*. Langmuir, 2014. **30**(35): p. 10643-50.
4. Neikov, O.D., S.S. Naboychenko, and I.B. Murashova, *Production of Copper and Copper Alloy Powders*, in *Handbook of Non-Ferrous Metal Powders*. 2019. p. 571-614.
5. Huang, D.-J. and T.-S. Leu, *Fabrication of high wettability gradient on copper substrate*. Applied Surface Science, 2013. **280**: p. 25-32.
6. Lathe, S.S., et al., *Sliding behavior of water drops on sol-gel derived hydrophobic silica films*. Applied Surface Science, 2010. **256**(10): p. 3259-3264.
7. Song, Z., et al., *Controllable bidirectional wettability transition of impregnated graphite by laser treatment and transition mechanism analysis*. Surface and Coatings Technology, 2017. **317**: p. 95-102.
8. Choi, W., et al., *Electrospinning onto Insulating Substrates by Controlling Surface Wettability and Humidity*. Nanoscale research letters, 2017. **12**(1): p. 610.
9. Mvola, B., P. Kah, and J. Martikainen, *Welding of dissimilar non-ferrous metals by GMAW processes*. International Journal of Mechanical and Materials Engineering, 2014. **9**(1): p. 21.
10. Do Lago, D., et al., *The use of experimental design for the study of the corrosion of bronze pretreated with AMT in artificial rainwater*. Progress in Organic Coatings, 2013. **76**(10): p. 1289-1295.
11. Luke, A., *Preparation, measurement and analysis of the microstructure of evaporator surfaces*. International journal of thermal sciences, 2006. **45**(3): p. 237-256.
12. Lee, D.-W., et al., *Characteristics and mechanism of Cu films fabricated at room temperature by aerosol deposition*. Nanoscale research letters, 2016. **11**(1): p. 162.
13. Young, C., J. Duh, and C. Huang, *Improved characteristics of electroless Cu deposition on Pt-Ag metallized Al₂O₃ substrates in microelectronics packaging*. Surface and Coatings Technology, 2001. **145**(1-3): p. 215-225.
14. Sartini, L., et al., *Nuclear instruments and methods in physics research section A: Accelerators, spectrometers, detectors and associated equipment*. Nuclear Instruments and Methods in Physics Research A, 2010.
15. Jegadheeswaran, S., S. Pohekar, and T. Kousksou, *Investigations on thermal storage systems containing micron-sized conducting particles dispersed in a phase change material*. Materials for Renewable and Sustainable Energy, 2012. **1**(1): p. 5.
16. Rubina, M.S., et al., *Synthesis and characterization of chitosan-copper nanocomposites and their fungicidal activity against two sclerotia-forming*

- plant pathogenic fungi*. Journal of Nanostructure in Chemistry, 2017. **7**(3): p. 249-258.
17. Haroun, N.A., et al., *Heat and mass transfer of nanofluid through an impulsively vertical stretching surface using the spectral relaxation method*. Boundary Value Problems, 2015. **2015**(1): p. 161.
 18. Storme, P., O. Schalm, and R. Wiesinger, *The sulfidation process of sterling silver in different corrosive environments: impact of the process on the surface films formed and consequences for the conservation-restoration community*. Heritage Science, 2015. **3**(1): p. 25.
 19. Morales, J., et al., *Antagonistic effects of copper on the electrochemical performance of LiFePO₄*. Electrochimica acta, 2007. **53**(2): p. 920-926.
 20. Guo, Y.-h., et al., *A catalytic oxidation approach to coat copper powder with polyaniline*. Surface and Coatings Technology, 2007. **202**(3): p. 555-558.
 21. Bateni, M., et al., *Oxidation behaviour of titanium coated copper substrate*. Surface and Coatings Technology, 2001. **139**(2-3): p. 192-199.
 22. Tsai, C.-Y., et al., *A study of the preparation and properties of antioxidative copper inks with high electrical conductivity*. Nanoscale research letters, 2015. **10**(1): p. 357.
 23. Nadutov, V., et al., *Influence of Oxidation on Electrical Properties of Compacted Cu Nanopowders*. Nanoscale research letters, 2016. **11**(1): p. 478.
 24. Aghilizadeh, N., A. Sari, and D. Dorrnian, *Role of Ar/O₂ mixture on structural, compositional and optical properties of thin copper oxide films deposited by DC magnetron sputtering*. Journal of Theoretical and Applied Physics, 2017. **11**(4): p. 285-290.
 25. Sigley, J.L., P.C. Johnson, and S.P. Beaudoin, *Use of nonionic surfactant to reduce sulfuric acid mist in the copper electrowinning process*. Hydrometallurgy, 2003. **70**(1-3): p. 1-8.
 26. Haghghi, H.K., et al., *Production of copper cathode from oxidized copper ores by acidic leaching and two-step precipitation followed by electrowinning*. Hydrometallurgy, 2013. **133**: p. 111-117.
 27. Rasgado, M.A., et al., *Bi-metallic dies for rapid die casting*. Journal of materials processing technology, 2006. **175**(1-3): p. 109-116.
 28. Yuan, W., et al., *High-performance CuO/Cu composite current collectors with array-pattern porous structures for lithium-ion batteries*. Electrochimica Acta, 2017. **226**: p. 89-97.
 29. Gu, H., et al., *Investigation on contact angle measurement methods and wettability transition of porous surfaces*. Surface and Coatings Technology, 2016. **292**: p. 72-77.
 30. Wu, M.-S., et al., *Effects of copper trifluoromethanesulphonate as an additive to propylene carbonate-based electrolyte for lithium-ion batteries*. Electrochimica acta, 2004. **49**(25): p. 4379-4386.
 31. Bandarenka, H., et al., *Nanostructures formed by displacement of porous silicon with copper: from nanoparticles to porous membranes*. Nanoscale research letters, 2012. **7**(1): p. 477.
 32. Du, M., H. wei Zhang, and Y. xiang Li, *Inner surface alloying on pores of lotus-type porous copper through electroless plating with supersonic vibration and annealing treatment*. Surface and Coatings Technology, 2015. **261**: p. 1-6.

33. Song, T., et al., *Creation of bimodal porous copper materials by an annealing-electrochemical dealloying approach*. *Electrochimica Acta*, 2015. **164**: p. 288-296.
34. Salem, S.B., et al., *Study and characterization of porous copper oxide produced by electrochemical anodization for radiometric heat absorber*. *Nanoscale research letters*, 2014. **9**(1): p. 577.
35. Nam, D., et al., *Effects of (NH₄)₂SO₄ and BTA on the nanostructure of copper foam prepared by electrodeposition*. *Electrochimica Acta*, 2011. **56**(25): p. 9397-9405.
36. Nguyen, T., et al., *Hydrogen bubbling-induced micro/nano porous MnO₂ films prepared by electrodeposition for pseudocapacitor electrodes*. *Electrochimica Acta*, 2016. **202**: p. 166-174.
37. Zhang, K., et al., *Two-step preparation of porous nickel-sulfur electrode for hydrogen evolution in alkaline water electrolysis*. *Electrochimica Acta*, 2017. **228**: p. 422-427.
38. Qiu, H., et al., *Facile electrochemical preparation of three-dimensional porous Cu films by potential perturbation*. *Electrochimica acta*, 2010. **55**(20): p. 6081-6087.
39. Coskun, S.B. and N.C. Wardlaw, *Influences of pore geometry, porosity and permeability on initial water saturation—An empirical method for estimating initial water saturation by image analysis*. *Journal of Petroleum Science and Engineering*, 1995. **12**(4): p. 295-308.
40. Bagheri, H., et al., *Facile fabrication of uniform hierarchical structured (UHS) nanocomposite surface with high water repellency and self-cleaning properties*. *Applied Surface Science*, 2018. **436**: p. 1134-1146.
41. Nikolić, N., et al., *Morphologies of copper deposits obtained by the electrodeposition at high overpotentials*. *Surface and Coatings Technology*, 2006. **201**(3-4): p. 560-566.
42. Viswanath, S. and M. Jachak, *ELECTRODEPOSITION OF COPPER POWDER FROM COPPER SULPHATE SOLUTION IN PRESENCE OF GLYCEROL AND SULPHURIC ACID*. *METALLURGICAL & MATERIALS ENGINEERING*, 2013. **19**(2): p. 119-135.
43. Singh, H., et al., *Electrodeposition of porous copper as a substrate for electrocatalytic material*. *Journal of Electroanalytical Chemistry*, 2017. **785**: p. 1-7.
44. Rafiee, J., et al., *Wetting transparency of graphene*. *Nat Mater*, 2012. **11**(3): p. 217-22.
45. Shin, Y.J., et al., *Surface-energy engineering of graphene*. *Langmuir*, 2010. **26**(6): p. 3798-3802.
46. Tewari, P., R. Khanduja, and M. Gupta, *Performance enhancement for crystallization unit of a sugar plant using genetic algorithm technique*. *Journal of Industrial Engineering International*, 2012. **8**(1): p. 1.
47. Andone, D., et al., *Evolved fuzzy control system for a drum boiler*. *IFAC Proceedings Volumes*, 2007. **40**(8): p. 141-146.
48. Trivedi, D.P., R.I. Bagga, and J.V. Chokshi, *Structural engineering challenges in structures for cooling water system in thermal power plant*. *Procedia Engineering*, 2013. **51**: p. 141-150.

49. Seneviratne, M., *A practical approach to water conservation for commercial and industrial facilities*. 2007: Elsevier.
50. Khandekar, S. and K. Muralidhar, *Dropwise condensation on inclined textured surfaces*. Vol. 302791. 2014: Springer.
51. Dorrer, C. and J. R uhe, *Condensation and wetting transitions on microstructured ultrahydrophobic surfaces*. *Langmuir*, 2007. **23**(7): p. 3820-3824.
52. Jung, Y. and B. Bhushan, *Wetting behaviour during evaporation and condensation of water microdroplets on superhydrophobic patterned surfaces*. *Journal of microscopy*, 2008. **229**(1): p. 127-140.
53. Cai, T.-m., et al., *Investigation of Cassie-Wenzel wetting transitions on microstructured surfaces*. *Colloid and Polymer Science*, 2016. **294**(5): p. 833-840.
54. Yan, X., et al., *Droplet condensation on superhydrophobic surfaces with enhanced dewetting under a tangential AC electric field*. *Applied Physics Letters*, 2016. **109**(16): p. 161601.
55. Good, R.J., *Contact angles and the surface free energy of solids*, in *Surface and colloid science*. 1979, Springer. p. 1-29.
56. Liu, Y., X. Yan, and Z. Wang, *Droplet dynamics on slippery surfaces: Small droplet, big impact*. *Biosurface and Biotribology*, 2019. **5**(2): p. 35-45.
57. Preston, D.J., et al., *Scalable graphene coatings for enhanced condensation heat transfer*. *Nano letters*, 2015. **15**(5): p. 2902-2909.
58. Rose, J., *Dropwise condensation theory and experiment: a review*. *Proceedings of the Institution of Mechanical Engineers, Part A: Journal of Power and Energy*, 2002. **216**(2): p. 115-128.
59. Erbi, H.Y., *Surface Chemistry*, in *Surface Chemistry Of Solid and Liquid Interfaces*. 2006, Blackwell Victoria Australia p. 360.
60. Yamamoto, M., et al., *Theoretical Explanation of the Lotus Effect: Superhydrophobic Property Changes by Removal of Nanostructures from the Surface of a Lotus Leaf*. *Langmuir*, 2015. **31**(26): p. 7355-63.
61. Bormashenko, E., et al., *Characterization of rough surfaces with vibrated drops*. *Phys Chem Chem Phys*, 2008. **10**(27): p. 4056-61.
62. Nosonovsky, M. and B. Bhushan, *Multiscale effects and capillary interactions in functional biomimetic surfaces for energy conversion and green engineering*. *Philos Trans A Math Phys Eng Sci*, 2009. **367**(1893): p. 1511-39.
63. Hosseini, S., H. Savaloni, and M. Gholipour-Shahraki, *Design and fabrication of highly hydrophobic Mn nano-sculptured thin films and evaluation of surface properties on hydrophobicity*. *Journal of Theoretical and Applied Physics*, 2017. **11**(1): p. 1-11.
64. Yanashima, R., et al., *Cutting a drop of water pinned by wire loops using a superhydrophobic surface and knife*. *PLoS One*, 2012. **7**(9): p. e45893.
65. Cao, C. and J. Cheng, *Fabrication of robust surfaces with special wettability on porous copper substrates for various oil/water separations*. *Chemical Engineering Journal*, 2018. **347**: p. 585-594.
66. Zhang, P., et al., *Enhanced Coalescence-Induced Droplet-Jumping on Nanostructured Superhydrophobic Surfaces in the Absence of Microstructures*. *ACS Appl Mater Interfaces*, 2017. **9**(40): p. 35391-35403.

67. M. Mosonviski, *Multiscale Dissipative Mechanisms and Hierarch*. 2007, New York: Springer
68. Koch, K., *Diversity of structure, morphology and wetting of plant surfaces*. Royal Society of Chemistry 2008. **2008**: p. 1943-1963.
69. Schlesinger, M. and M. Paunovic, *Modern electroplating*. Vol. 55. 2011: John Wiley & Sons.
70. Wolf, M.J., et al., *Flip chip bumping technology—Status and update*. Nuclear Instruments and Methods in Physics Research Section A: Accelerators, Spectrometers, Detectors and Associated Equipment, 2006. **565**(1): p. 290-295.
71. Kanani, N., *Electroplating: basic principles, processes and practice*. 2004: Elsevier.
72. Sosa, G.L., A. Zalts, and S.A. Ramírez, *Complexing capacity of electroplating rinsing baths—a twist to the resolution of two ligand families of similar strength*. Journal of Analytical Science and Technology, 2016. **7**(1): p. 7.
73. Bockris, J.O.M., A.K. Reddy, and M. Gamboa-Aldeco, *Modern Electrochemistry: Fundamentals of Electrodeposition*. V. 2a. 1998: Plenum Press.
74. Alkire, R.C., et al., *Advances in electrochemical science and engineering*. 2002: Wiley Online Library.
75. Eroglu, D., et al., *Use of dispersants to enhance incorporation rate of nanoparticles into electrodeposited films*. Electrochimica Acta, 2013. **113**: p. 628-634.
76. Keller, R., S. Rolseth, and J. Thonstad, *Mass transport considerations for the development of oxygen-evolving anodes in aluminum electrolysis*. Electrochimica acta, 1997. **42**(12): p. 1809-1817.
77. Kuhn, H., *Powder metallurgy processing: the techniques and analyses*. 2012: Elsevier.
78. Jones, D.A., *Electrical engineering: the backbone of society*. IEE Proceedings A (Science, Measurement and Technology), 1991. **138**(1): p. 1-10.
79. Lufitha, M., *Effect of substrate temperature on coating adhesion*. 2001, National Library of Canada= Bibliothèque nationale du Canada.
80. Nikolić, N.D., et al., *Application of pulsating overpotential regime on the formation of copper deposits in the range of hydrogen co-deposition*. Journal of Solid State Electrochemistry, 2010. **14**(2): p. 331.
81. Bo, Z., et al., *Design of supercapacitor electrodes using molecular dynamics simulations*. Nano-micro letters, 2018. **10**(2): p. 33.
82. Welch, D.A., et al., *Using molecular dynamics to quantify the electrical double layer and examine the potential for its direct observation in the in-situ TEM*. Advanced Structural and Chemical Imaging, 2015. **1**(1): p. 1.
83. Davis, J.R., *Copper and copper alloys*. 2001: ASM international.
84. Nikolić, N., *Fundamental aspects of copper electrodeposition in the hydrogen co-deposition range*. Zaštita materijala, 2010. **51**(4): p. 197-203.
85. Nikolić, N.D. and K.I. Popov, *Hydrogen co-deposition effects on the structure of electrodeposited copper*, in *Electrodeposition*. 2010, Springer, New York, NY. p. 1-70.

86. Maharana, H. and A. Basu, *Evolution and structure-property correlation of CTAB assisted high hardness electrodeposited Cu-ZrO₂ nano-cone arrays*. Surface and Coatings Technology, 2017. **310**: p. 148-156.
87. Dini, J.W. and D.D. Snyder, *Electrodeposition of copper*. Modern electroplating, 2010: p. 33-78.
88. Asnavandi, M. and C. Zhao, *Hydrogen bubble-assisted electrodeposition of metal nanoparticles from protic ionic liquids for electrocatalysis*. ACS Sustainable Chemistry & Engineering, 2016. **5**(1): p. 85-89.
89. Li, Y., et al., *Superhydrophobicity of 3D porous copper films prepared using the hydrogen bubble dynamic template*. Chemistry of Materials, 2007. **19**(23): p. 5758-5764.
90. Najdovski, I., *The electrochemical fabrication of porous bimetallic structures and their applications in catalysis and sensing*. 2013.
91. Plowman, B.J., L.A. Jones, and S.K. Bhargava, *Building with bubbles: the formation of high surface area honeycomb-like films via hydrogen bubble templated electrodeposition*. Chemical Communications, 2015. **51**(21): p. 4331-4346.
92. Kristof, P. and M. Pritzker, *Effect of electrolyte composition on the dynamics of hydrogen gas bubble evolution at copper microelectrodes*. Journal of applied electrochemistry, 1997. **27**(3): p. 255-265.
93. Kim, J.-H., R.-H. Kim, and H.-S. Kwon, *Preparation of copper foam with 3-dimensionally interconnected spherical pore network by electrodeposition*. Electrochemistry Communications, 2008. **10**(8): p. 1148-1151.
94. Shin, H.-C. and M. Liu, *Copper foam structures with highly porous nanostructured walls*. Chemistry of materials, 2004. **16**(25): p. 5460-5464.
95. Luo, B., et al., *3D Porous Copper Films with Large Specific Surface Prepared by Hydrogen Bubble Template*. Asian Journal of Chemistry, 2013. **25**(17).
96. Yuan, Z., et al., *Fabrication of superhydrophobic surface with hierarchical multi-scale structure on copper foil*. Surface and Coatings Technology, 2014. **254**: p. 151-156.
97. Qiu, W., et al., *Fabrication of superhydrophobic surfaces by smoke deposition and application in oil-water separation*. RSC advances, 2015. **5**(87): p. 71329-71335.
98. Wang, H., et al., *A facile two-step approach to prepare superhydrophobic surfaces on copper substrates*. Journal of Materials Chemistry A, 2014. **2**(14): p. 5010-5017.
99. Fan, Y., et al., *Preparation of superhydrophobic films on copper substrate for corrosion protection*. Surface and Coatings Technology, 2014. **244**: p. 1-8.
100. Zhijin, G., et al., *Fabrication of super hydrophobic surfaces on copper by solution-immersion*. Chinese Journal of Chemical Engineering, 2013. **21**(8): p. 920-926.
101. Li, J., et al., *One-step preparation of transparent superhydrophobic coatings using atmospheric arc discharge*. Applied Physics Letters, 2015. **107**(5): p. 051603.
102. Jo, S.B., et al., *Large-area graphene synthesis and its application to interface-engineered field effect transistors*. Solid state communications, 2012. **152**(15): p. 1350-1358.

103. Nair, R.R., et al., *Fine structure constant defines visual transparency of graphene*. Science, 2008. **320**(5881): p. 1308-1308.
104. Balaji, A. and J. Zhang, *Electrochemical and optical biosensors for early-stage cancer diagnosis by using graphene and graphene oxide*. Cancer nanotechnology, 2017. **8**(1): p. 10.
105. Kalisz, M., et al., *Comparison of mechanical and corrosion properties of graphene monolayer on Ti–Al–V and nanometric Nb₂O₅ layer on Ti–Al–V alloy for dental implants applications*. Thin Solid Films, 2015. **589**: p. 356-363.
106. Shareena, T.P.D., et al., *A review on graphene-based nanomaterials in biomedical applications and risks in environment and health*. Nano-micro letters, 2018. **10**(3): p. 53.
107. Soldano, C., A. Mahmood, and E. Dujardin, *Production, properties and potential of graphene*. Carbon, 2010. **48**(8): p. 2127-2150.
108. Pham, A.T., M. Barisik, and B. Kim, *Interfacial thermal resistance between the graphene-coated copper and liquid water*. International Journal of Heat and Mass Transfer, 2016. **97**: p. 422-431.
109. Zhang, H., et al., *Strength and fracture behavior of graphene grain boundaries: effects of temperature, inflection, and symmetry from molecular dynamics*. Physical Chemistry Chemical Physics, 2013. **15**(28): p. 11794-11799.
110. Zhao, Y., et al., *Strengthening mechanisms of graphene coated copper under nanoindentation*. Computational Materials Science, 2018. **144**: p. 42-49.
111. Zhang, T., X. Li, and H. Gao, *Fracture of graphene: a review*. International Journal of Fracture, 2015. **196**(1-2): p. 1-31.
112. Zhao, H. and N.R. Aluru, *Temperature and strain-rate dependent fracture strength of graphene*. Journal of Applied Physics, 2010. **108**(6): p. 064321.
113. Bo, Z., et al., *Plasma-enhanced chemical vapor deposition synthesis of vertically oriented graphene nanosheets*. Nanoscale, 2013. **5**(12): p. 5180-5204.
114. Illakkiya, J.T., P.U. Rajalakshmi, and R. Oommen, *Nebulized spray pyrolysis: a new method for synthesis of graphene film and their characteristics*. Surface and Coatings Technology, 2016. **307**: p. 65-72.
115. Gong, L., et al., *Reversible loss of bernal stacking during the deformation of few-layer graphene in nanocomposites*. Acs Nano, 2013. **7**(8): p. 7287-7294.
116. Tjong, S.C., *Recent progress in the development and properties of novel metal matrix nanocomposites reinforced with carbon nanotubes and graphene nanosheets*. Materials Science and Engineering: R: Reports, 2013. **74**(10): p. 281-350.
117. Brownson, D. and C. Banks, *The Handbook of Graphene Electrochemistry 2014*. Springer London, Limited.
118. Kidambi, P.R., et al., *In situ observations during chemical vapor deposition of hexagonal boron nitride on polycrystalline copper*. Chemistry of Materials, 2014. **26**(22): p. 6380-6392.
119. Lim, S., et al., *Plasma-assisted synthesis of carbon nanotubes*. Nanoscale research letters, 2010. **5**(9): p. 1377.

120. Pedersen, H., et al., *A novel high-power pulse PECVD method*. Surface and Coatings Technology, 2012. **206**(22): p. 4562-4566.
121. Boccaccini, A.R. and I. Zhitomirsky, *Application of electrophoretic and electrolytic deposition techniques in ceramics processing*. Current Opinion in Solid State and Materials Science, 2002. **6**(3): p. 251-260.
122. Dickerson, J.H. and A.R. Boccaccini, *Electrophoretic deposition of nanomaterials*. 2011: Springer.
123. Gonzalez, Z., et al., *Electrochemical performance of pseudo-capacitor electrodes fabricated by Electrophoretic Deposition inducing Ni (OH)₂ nanoplatelets agglomeration by Layer-by-Layer*. Electrochimica Acta, 2017. **247**: p. 333-343.
124. Sarkar, P. and P.S. Nicholson, *Electrophoretic deposition (EPD): mechanisms, kinetics, and application to ceramics*. Journal of the American Ceramic Society, 1996. **79**(8): p. 1987-2002.
125. Van der Biest, O.O. and L.J. Vandeperre, *Electrophoretic deposition of materials*. Annual Review of Materials Science, 1999. **29**(1): p. 327-352.
126. Ganesan, S., *Simulations of impinging droplets with surfactant-dependent dynamic contact angle*. Journal of Computational Physics, 2015. **301**: p. 178-200.
127. Seo, K., M. Kim, and D.H. Kim, *Re-derivation of Young's Equation, Wenzel Equation, and Cassie-Baxter Equation Based on Energy Minimization, in Surface Energy*. 2015.
128. Darhuber, A.A. and S.M. Troian, *Principles of microfluidic actuation by modulation of surface stresses*. Annu. Rev. Fluid Mech., 2005. **37**: p. 425-455.
129. Weng, Y.H., et al., *Water-repellent hydrophilic nanogrooves*. Phys Chem Chem Phys, 2017. **19**(20): p. 13022-13029.
130. Indekeu, J., G. Backx, and G. Langie, *Line tension near multicritical wetting transitions*. Physica A: Statistical Mechanics and its Applications, 1993. **196**(3): p. 335-348.
131. Meier, G.H., *Thermodynamics of surfaces and interfaces: concepts in inorganic materials*. 2014: Cambridge University Press.
132. Esmailzadeh, I., et al., *A feasibility study on semi industrial nozzleless electrospinning of cellulose nanofiber*. International Journal of Industrial Chemistry, 2015. **6**(3): p. 193-211.
133. Speight, J.G., *Environmental organic chemistry for engineers*. 2016: Butterworth-Heinemann.
134. Speight, J.G., *Natural gas: a basic handbook*. 2018: Gulf Professional Publishing.
135. Bush, J.W., *Mit lecture notes on surface tension, lecture 5*. PDF). Massachusetts Institute of Technology. Retrieved April, 2007. **1**.
136. Extrand, C.W., *Origins of wetting*. Langmuir, 2016. **32**(31): p. 7697-7706.
137. Skłodowska, A., M. Woźniak, and R. Matlakowska, *The method of contact angle measurements and estimation of work of adhesion in bioleaching of metals*. Biological procedures online, 1999. **1**(3): p. 114.
138. Shen, Y., et al., *Relationship between Wetting Hysteresis and Contact Time of a Bouncing Droplet on Hydrophobic Surfaces*. ACS Appl Mater Interfaces, 2015. **7**(37): p. 20972-8.

139. Rusanov, A., A. Shchekin, and D. Tatyanyenko, *The line tension and the generalized Young equation: the choice of dividing surface*. Colloids and Surfaces A: Physicochemical and Engineering Aspects, 2004. **250**(1-3): p. 263-268.
140. Hsieh, C.-T., et al., *Water and oil repellency of flexible silica-coated polymeric substrates*. Applied Surface Science, 2010. **256**(16): p. 4867-4872.
141. Hozumi, A. and T.J. McCarthy, *Ultralyophobic oxidized aluminum surfaces exhibiting negligible contact angle hysteresis*. Langmuir, 2009. **26**(4): p. 2567-2573.
142. Wier, K.A., L. Gao, and T.J. McCarthy, *Two-dimensional fluidics based on differential lyophobicity and gravity*. Langmuir, 2006. **22**(11): p. 4914-4916.
143. ElSherbini, A. and A. Jacobi, *Retention forces and contact angles for critical liquid drops on non-horizontal surfaces*. Journal of colloid and interface science, 2006. **299**(2): p. 841-849.
144. Li, H. and K. Zhang, *Dynamic behavior of water droplets impacting on the superhydrophobic surface: Both experimental study and molecular dynamics simulation study*. Applied Surface Science, 2019. **498**: p. 143793.
145. Jasper, W.J. and N. Anand, *A generalized variational approach for predicting contact angles of sessile nano-droplets on both flat and curved surfaces*. Journal of Molecular Liquids, 2019. **281**: p. 196-203.
146. Milchev, A.I. and A.A. Milchev, *Wetting behavior of nanodroplets: The limits of Young's rule validity*. EPL (Europhysics Letters), 2001. **56**(5): p. 695.
147. Milchev, A., A. Milchev, and K. Binder, *Nanodroplets on a solid plane: wetting and spreading in a Monte Carlo simulation*. Computer physics communications, 2002. **146**(1): p. 38-53.
148. Wang, K., *Diffusion anomaly and blind pore character in carbon molecular sieve membrane*. Chemical engineering science, 2007. **62**(14): p. 3654-3659.
149. Ajaxon, I., C. Öhman, and C. Persson, *Long-term in vitro degradation of a high-strength brushite cement in water, PBS, and serum solution*. BioMed research international, 2015. **2015**.
150. Liu, Y. and Y. Zhu, *Comparison of pore characteristics in the coal and shale reservoirs of Taiyuan Formation, Qinshui Basin, China*. International Journal of Coal Science & Technology, 2016. **3**(3): p. 330-338.
151. Haugaard, J. and H. Livbjerg, *Models of pore diffusion in porous catalysts*. Chemical engineering science, 1998. **53**(16): p. 2941-2948.
152. Yang, R., et al., *The effects of mineral composition, TOC content and pore structure on spontaneous imbibition in Lower Jurassic Dongyuemiao shale reservoirs*. Marine and Petroleum Geology, 2019.
153. Yang, R., et al., *Experimental investigations on the geometry and connectivity of pore space in organic-rich Wufeng and Longmaxi shales*. Marine and Petroleum Geology, 2017. **84**: p. 225-242.
154. Yassin, M.R., et al., *A theory for relative permeability of unconventional rocks with dual-wettability pore network*. SPE Journal, 2016. **21**(06): p. 1,970-1,980.
155. Shi, S., H. Belhaj, and A. Bera, *Capillary pressure and relative permeability correlations for transition zones of carbonate reservoirs*. Journal of Petroleum Exploration and Production Technology, 2018. **8**(3): p. 767-784.

156. Oyenehin, B., *Introduction to the Hydrocarbon Composite Production System*, in *Integrated Sand Management For Effective Hydrocarbon Flow Assurance*. 2015. p. 11-128.
157. Mane, S., *Effect of porogens (type and amount) on polymer porosity: a review*. Can. Chem. Trans, 2016. **4**(2): p. 210-225.
158. Masoodi, R. and K.M. Pillai, *Wicking in porous materials: traditional and modern modeling approaches*. 2012: CRC Press.
159. Rabbani, H.S., V. Joekar-Niasar, and N. Shokri, *Effects of intermediate wettability on entry capillary pressure in angular pores*. Journal of colloid and interface science, 2016. **473**: p. 34-43.
160. Yang, L., et al., *Effect of annealing temperature on wettability of TiO₂ nanotube array films*. Nanoscale research letters, 2014. **9**(1): p. 621.
161. Wenzel, R.N., *Resistance of Solid Surfaces to Wetting by Water*. Industrial & Engineering Chemistry, 1936. **28**(8): p. 988-994.
162. Yoon, Y., D. Kim, and J.-B. Lee, *Hierarchical micro/nano structures for super-hydrophobic surfaces and super-lyophobic surface against liquid metal*. Micro and Nano Systems Letters, 2014. **2**(1): p. 3.
163. Bahners, T., et al., *Super-wetting surfaces by plasma-and UV-based grafting of micro-rough acrylate coatings*. Progress in Organic Coatings, 2013. **76**(10): p. 1356-1362.
164. Rudawska, A., *Surface Treatment in Bonding Technology*. 2019: Academic Press.
165. Oliveira, S., A. Stojanovic, and S. Seeger, *Superhydrophilic and superamphiphilic coatings*. Functional Polymer Coatings: Principles, Methods, and Applications, 2015. **12**: p. 96.
166. Cassie, A. and S. Baxter, *Wettability of porous surfaces*. Transactions of the Faraday society, 1944. **40**: p. 546-551.
167. Huang, W., et al., *Effect of polyethylene glycol on hydrophilic TiO₂ films: Porosity-driven superhydrophilicity*. Surface and Coatings Technology, 2010. **204**(24): p. 3954-3961.
168. Sun, C., et al., *Control of water droplet motion by alteration of roughness gradient on silicon wafer by laser surface treatment*. Thin Solid Films, 2008. **516**(12): p. 4059-4063.
169. Xiao, K., et al., *Modeling the Effects of Nanopatterned Surfaces on Wetting States of Droplets*. Nanoscale research letters, 2017. **12**(1): p. 309.
170. Whitney, H.M., et al., *Determining the contribution of epidermal cell shape to petal wettability using isogenic Antirrhinum lines*. PLoS One, 2011. **6**(3): p. e17576.
171. Gao, L. and J. He, *Surface hydrophobic co-modification of hollow silica nanoparticles toward large-area transparent superhydrophobic coatings*. Journal of colloid and interface science, 2013. **396**: p. 152-159.
172. Stocco, A. and M. Nobili, *A comparison between liquid drops and solid particles in partial wetting*. Advances in colloid and interface science, 2017. **247**: p. 223-233.
173. Kim, T.J. and C. Hidrovo, *Pressure and partial wetting effects on superhydrophobic friction reduction in microchannel flow*. Physics of Fluids, 2012. **24**(11): p. 112003.

174. Al-Sharafi, A., et al., *A water droplet pinning and heat transfer characteristics on an inclined hydrophobic surface*. Scientific reports, 2018. **8**(1): p. 3061.
175. Gao, N. and Y. Yan, *Modeling superhydrophobic contact angles and wetting transition*. Journal of Bionic Engineering, 2009. **6**(4): p. 335-340.
176. Schlangen, L.J., *Adsorption and wetting: experiments, thermodynamics and molecular aspects*. 1995: Schlangen.
177. Lv, Y., et al., *Interfacial effect on the electrochemical properties of the layered graphene/metal sulfide composites as anode materials for Li-ion batteries*. Surface Science, 2016. **651**: p. 10-15.
178. Bai, S., et al., *Enhancement of mechanical and electrical properties of graphene/cement composite due to improved dispersion of graphene by addition of silica fume*. Construction and Building Materials, 2018. **164**: p. 433-441.
179. Raza, M.A., et al., *Electrochemical behavior of graphene coatings deposited on copper metal by electrophoretic deposition and chemical vapor deposition*. Surface and Coatings Technology, 2017. **332**: p. 112-119.
180. Yang, C., et al., *Shell-isolated graphene@ Cu nanoparticles on graphene@ Cu substrates for the application in SERS*. Carbon, 2016. **98**: p. 526-533.
181. Liu, X., et al., *Shear modulus of monolayer graphene prepared by chemical vapor deposition*. Nano letters, 2012. **12**(2): p. 1013-1017.
182. Xu, Z. and M.J. Buehler, *Interface structure and mechanics between graphene and metal substrates: a first-principles study*. Journal of Physics: Condensed Matter, 2010. **22**(48): p. 485301.
183. Chen, X.-D., et al., *High-quality and efficient transfer of large-area graphene films onto different substrates*. Carbon, 2013. **56**: p. 271-278.
184. Kalita, D., *Graphene produced by Chemical Vapor Deposition: From control and understanding of atomic scale defects to production of macroscale functional devices*. 2015, Université Grenoble Alpes.
185. Boukhvalov, D., et al., *Atomic and electronic structure of a copper/graphene interface as prepared and 1.5 years after*. Applied Surface Science, 2017. **426**: p. 1167-1172.
186. Choi, B.K., et al., *Tunable wetting property in growth mode-controlled WS₂ thin films*. Nanoscale research letters, 2017. **12**(1): p. 262.
187. Yavari, F., et al., *Tunable bandgap in graphene by the controlled adsorption of water molecules*. small, 2010. **6**(22): p. 2535-2538.
188. Shih, C.-J., et al., *Breakdown in the wetting transparency of graphene*. Physical review letters, 2012. **109**(17): p. 176101.
189. Taherian, F., et al., *What is the contact angle of water on graphene?* Langmuir, 2013. **29**(5): p. 1457-1465.
190. Leenaerts, O., B. Partoens, and F. Peeters, *Water on graphene: Hydrophobicity and dipole moment using density functional theory*. Physical Review B, 2009. **79**(23): p. 235440.
191. Solanky, P., et al., *The inherent behavior of graphene flakes in water: A molecular dynamics study*. Computational Materials Science, 2019. **162**: p. 140-147.
192. Rafiee, J., et al., *Superhydrophobic to superhydrophilic wetting control in graphene films*. Advanced Materials, 2010. **22**(19): p. 2151-2154.

193. Xu, K., et al., *Wetting properties of defective graphene oxide: A molecular simulation study*. *Molecules*, 2018. **23**(6): p. 1439.
194. Wang, S., et al., *Wettability and surface free energy of graphene films*. *Langmuir*, 2009. **25**(18): p. 11078-11081.
195. Surwade, S.P., et al., *Water desalination using nanoporous single-layer graphene*. *Nature nanotechnology*, 2015. **10**(5): p. 459-464.
196. Dey, A., et al., *Plasma engineering of graphene*. *Applied Physics Reviews*, 2016. **3**(2): p. 021301.
197. Safarpour, M., A. Khataee, and V. Vatanpour, *Thin film nanocomposite reverse osmosis membrane modified by reduced graphene oxide/TiO₂ with improved desalination performance*. *Journal of Membrane Science*, 2015. **489**: p. 43-54.
198. Ma, J., et al., *Robust stable MoS₂/GO filtration membrane for effective removal of dyes and salts from water with enhanced permeability*. *Desalination*, 2020. **480**: p. 114328.
199. Zhu, J., et al., *Mussel-inspired architecture of high-flux loose nanofiltration membrane functionalized with antibacterial reduced graphene oxide-copper nanocomposites*. *ACS applied materials & interfaces*, 2017. **9**(34): p. 28990-29001.
200. Wong, S.-C. and Y.-C. Lin, *Effect of copper surface wettability on the evaporation performance: Tests in a flat-plate heat pipe with visualization*. *International journal of heat and mass transfer*, 2011. **54**(17-18): p. 3921-3926.
201. Shirazy, M.R., S. Blais, and L.G. Fréchette, *Mechanism of wettability transition in copper metal foams: From superhydrophilic to hydrophobic*. *Applied Surface Science*, 2012. **258**(17): p. 6416-6424.
202. Whyman, G. and E. Bormashenko, *Wetting transitions on rough substrates: General considerations*. *Journal of adhesion science and technology*, 2012. **26**(1-3): p. 207-220.
203. Kung, C.H., et al., *Assessment and interpretation of surface wettability based on sessile droplet contact angle measurement: challenges and opportunities*. *Adv. Mater. Interfaces*, 2019. **6**(18): p. 1900839.
204. Nam, Y. and Y.S. Ju, *Comparative Study of Copper Oxidation Schemes and Their Effects on Surface Wettability*, in *Proceedings of the ASME 2008 International Mechanical Engineering Congress and Exposition*. 2008: Boston, MA. p. 1833–1838.
205. Millet, D.B., et al., *Atmospheric volatile organic compound measurements during the Pittsburgh air quality study: results, interpretation, and quantification of primary and secondary contributions*. *J. Geophys. Res. Atmos.*, 2005. **110**(D7).
206. Hurst, J.M., L. Li, and H. Liu, *Adventitious hydrocarbons and the graphite-water interface*. *Carbon*, 2018. **134**: p. 464–469.
207. Mitchell, D.R., *Contamination mitigation strategies for scanning transmission electron microscopy*. *Micron*, 2015. **73**: p. 36-46.
208. Zisman, W.A., *Influence of constitution on adhesion*. *Ind. Eng. Chem.*, 1963. **55**(10): p. 18–38.
209. Oliver, J.F., C. Huh, and S.G. Mason, *Resistance to spreading of liquids by sharp edges*. *J. Colloid Interface Sci.*, 1977. **59**(3): p. 568–581.

210. Candal, R.J., A.E. Regazzoni, and M.A. Blesa, *Precipitation of copper (II) hydrous oxides and copper (II) basic salts*. Journal Of Materials Chemistry, 1992. **2**(6): p. 657-661.
211. Hashemi, T. and C. Hogarth, *The mechanism of corrosion inhibition of copper in NaCl solution by benzotriazole studied by electron spectroscopy*. Electrochimica acta, 1988. **33**(8): p. 1123-1127.
212. El Warraky, A., H. El Shayeb, and E. Sherif, *Pitting corrosion of copper in chloride solutions*. Anti-Corrosion Methods and Materials, 2004.
213. Xia, X., et al., *Corrosion characteristics of copper microparticles and copper nanoparticles in distilled water*. Corrosion Science, 2006. **48**(12): p. 3924-3932.
214. Gorgolis, G. and C. Galiotis, *Graphene aerogels: a review*. 2D Materials, 2017. **4**(3): p. 032001.
215. Zegeye, E., A.K. Ghamsari, and E. Woldesenbet, *Mechanical properties of graphene platelets reinforced syntactic foams*. Composites Part B: Engineering, 2014. **60**: p. 268-273.
216. Le, H.D., et al., *Synthesis of multi-layer graphene films on copper tape by atmospheric pressure chemical vapor deposition method*. Advances in Natural Sciences: Nanoscience and Nanotechnology, 2013. **4**(3): p. 035012.
217. Teng, T.-P., et al., *High-yield production of graphene flakes using a novel electrochemical/mechanical hybrid exfoliation*. The International Journal of Advanced Manufacturing Technology, 2019. **104**(5): p. 2751-2760.
218. Ferrari, A.C., et al., *Raman spectrum of graphene and graphene layers*. Physical review letters, 2006. **97**(18): p. 187401.
219. Tang, B., H. Guoxin, and H. Gao, *Raman spectroscopic characterization of graphene*. Applied Spectroscopy Reviews, 2010. **45**(5): p. 369-407.
220. Silva, D.L., et al., *Raman spectroscopy analysis of number of layers in mass-produced graphene flakes*. Carbon, 2020. **161**: p. 181-189.
221. Tynan, M.K., et al., *Formation of 3D graphene foams on soft templated metal monoliths*. Nanoscale, 2016. **8**(27): p. 13303-13310.
222. Kim, K.S., et al., *Large-scale pattern growth of graphene films for stretchable transparent electrodes*. nature, 2009. **457**(7230): p. 706-710.
223. Rho, H., et al., *Three-dimensional porous copper-graphene heterostructures with durability and high heat dissipation performance*. Scientific Reports, 2015. **5**(1): p. 1-7.
224. Zhang, J., et al., *Clean transfer of large graphene single crystals for high-intactness suspended membranes and liquid cells*. Advanced Materials, 2017. **29**(26): p. 1700639.
225. Pu, N.-W., et al., *Dispersion of graphene in aqueous solutions with different types of surfactants and the production of graphene films by spray or drop coating*. Journal of the Taiwan Institute of Chemical Engineers, 2012. **43**(1): p. 140-146.
226. Hadi, A., et al., *Graphene nanosheets preparation using magnetic nanoparticle assisted liquid phase exfoliation of graphite: the coupled effect of ultrasound and wedging nanoparticles*. Ultrasonics sonochemistry, 2018. **44**: p. 204-214.

227. Huang, C., F. Xu, and Y. Sun, *Effects of morphology, tension and vibration on wettability of graphene: a molecular dynamics study*. Computational Materials Science, 2017. **139**: p. 216-224.
228. Wang, N., et al., *Role of surfactants in construction of porous copper film by electrodeposition approach*. Transactions of the IMF, 2011. **89**(5): p. 261-267.
229. Jaschke, M., et al., *Surfactant aggregates at a metal surface*. Langmuir, 1997. **13**(6): p. 1381-1384.
230. Fenske, M., et al., *Raman spectra of hydrocarbons*. Analytical Chemistry, 1947. **19**(10): p. 700-765.
231. Sterin, K.E., V. Aleksanyan, and G.N. Zhizhin, *Raman spectra of hydrocarbons*. 2013: Elsevier.
232. Zhang, N., et al., *Raman characteristics of hydrocarbon and hydrocarbon inclusions*. Science in China Series D: Earth Sciences, 2007. **50**(8): p. 1171-1178.



VITA

NAME Husam Eltigani

DATE OF BIRTH 19 September 1974

PLACE OF BIRTH Barber/ Sudan

INSTITUTIONS ATTENDED Khartoum University
King Mongkut's University of Technology North Bangkok
Chulalongkorn University

HOME ADDRESS 154, Sukumvit Road, Wattana, Klongtoi, 10110, Bangkok, Thailand

PUBLICATION Paper 1 Husam Eltigani, Yuttanant Boonyongmaneerat
Modifications of the wetting characteristics of electrodeposited porous copper by controlling the plating parameters and storage conditions. Micron Journal Volume 150. 2021.

Paper 2 submitted to Journal of Metals, Materials and Minerals (JMMM) with the title of Progress of Water Desalination Application Based on Wettability and Surface Characteristic of Graphene and Graphene Oxide: Review, Husam Eltigani, Yuttanant Boonyongmaneerat, July, 2022.

AWARD RECEIVED The 100th Anniversary Chulalongkorn University Scholarship